Modelling of the galactic chemical evolution of r-process elements

Inauguraldissertation

zur

Erlangung der Würde eines Doktors der Philosophie

vorgelegt der

Philosophisch-Naturwissenschaftlichen Fakultät

der Universität Basel

von

Benjamin Wehmeyer
aus Westerland/Sylt, Deutschland

Basel, 2018

Genehmigt von der Philosophisch-Naturwissenschaftlichen Fakultät
auf Antrag von
Prof. Dr. Friedrich-Karl Thielemann & Prof. Dr. Francesca Matteucci

Basel, den 15.11.2016
(Datum der Genehmigung durch die Fakultät)

Prof. Dr. Jörg Schibler,
Dekan

Acknowledgement

This work would not have been possible without the contributions and help of many people.

First of all, I would like to thank my family for constantly supporting me. They provided me with the required energy to complete this work.

Greatest gratitude is awarded to Friedel Thielemann for giving me the chance to do a PhD in his group; Also for introducing me to the exciting life of an astrophysicist. Thank you for many great discussions, travel opportunities, and constantly great support, in all areas of the scientific life. (Although he always insists that he is a bad supervisor, he is actually a very good one!)

Thomas Rauscher for insisting me to hear his astrophysics lecture which showed me the beauty of the field and paved the path to this PhD.

Marco Pignatari for support, numerous discussions, help with coding, writing parts and constantly correcting parts of my publications.

Francesca Matteucci for providing her book (giving me large insights in the field of galactic chemical evolution), constant support and agreeing to act as co-examinator for this thesis.

Brad Gibson and his galaxy dynamics team at the University of Hull (namely Chris Jordan, C. Gareth Few) for letting me visit them, and for nice discussions and having great times. The third chapter of this thesis can be seen as the

(scientific) outcome of this nice exchange, which I enjoyed a lot, and hope it will be ongoing in the future.

Thanks to my office mates for spending the last (nearly) three years with me, for scientific and private exchange, providing drawings and figures, or helping me with simplest calculations (for the teaching) and concepts. This acknowledgement includes the entire nuclear astrophysics group. It has been a pleasure for me to work with you.

Dominik Argast for providing his GCE code "ICE" for our investigations.

Further acknowledgmements go to Almudena Arcones, John Cowan, Gabriel Martínez-Pinedo, Lyudmila Mashonkina, Francesca Matteucci, Tamara Mishenina, Nobuya Nishimura, Igor Panov, Albino Perego, Tsvi Piran, Nikos Prantzos, Stephan Rosswog, and Tomoya Takiwaki for helpful discussions during the Basel Brainstorming workshop and several other meetings; Camilla J. Hansen, Oleg Korobkin, Yuhri Ishimaru, and Shinya Wanajo for discussions at ECT* in Trento, and Freeke van de Voort for providing details about their modelling.

Takuji Tsujimoto and Nobuya Nishimura for providing the observational data for chapter three.

I greatly acknowledge financial support by the European Research Council (FP7) under ERC Advanced Grant Agreement No. 321263 - FISH, and the Swiss National Science Foundation (SNF), the Utrecht Network and the CCCS of the University of Basel. The Basel group is a member in the COST Action New Compstar.

Contents

1 Introduction

1.1 Motivation

Are we made of star dust? This question which already guided me during my master studies could be a good motivation to justify the efforts taken in this work.

The Big Bang made space itself and time itself. Also, a lot of energy was put in the newly formed space. At that time, space was only filled with high energetic photons, so there was only "light". After the inflation phase, parts of the light transformed to quarks and gluons which formed a plasma. After 10^{-6} seconds, baryons could form from the quarks and gluons. However, from that point of time until 10^{-4} seconds, only matter and anti-matter pairs formed, which annihilated shortly after their formation. A very tiny imbalance, an excess of only one matter constituent per 10 billion matter-anti matter pairs permitted that, after 10^{-4} seconds, matter could become the dominant species. Since the temperature dropped, the large hadrons decayed and formed a soup of protons and neutrons. They were evenly abundant and due to the high temperature, could still transition from one to the other. In these processes also neutrinos were formed and absorbed. After one second, neutrons could not transform to protons any more and vice versa. The neutrinos decoupled and hence stopped interacting with matter. At that time, the ratio between protons and neutrons was 6:1. Deuterons (^2H) could form, but were almost immediately disintegrated due to high energetic photons. When a minute had passed, the temperature had become so low, that not too much of these high energetic photons were around any more. So, deuterons could not form effectively during that time. Since (free) neutrons decay very fast, the proton to neutron ratio decreased further to 7:1. From here, most of the neutrons became bound in a ^4He nucleus. Since there is

no stable nucleus with mass number 5 or 8, only traces of ^7Li and ^3He could be formed. After five minutes, the density in the Universe had dropped so far that further nuclear reactions were not possible at that time. From here on, the primordial nucleosynthesis had come to an end, resulting in a mass ratio of $\approx 75\%$ ^1H, and $\approx 25\%$ ^4He, and traces of ^3He and ^7Li. Those neutrons unable to find a reaction partner decayed spontaneously after a couple of minutes.

Since only ^1H, ^4He, and traces of ^3He and ^7Li were formed, but we *observe* and actually *consist* of heavier elements as carbon and oxygen, and some heavy elements, we might ask the question:

So, if they were not formed in the beginning, where were they actually formed?

The answer to that is not too easy and still debated. While the situation of the formation of elements more massive than helium up to iron is *relatively* well-known, the situation beyond iron is still under investigation. This thesis tries to contribute a tiny piece to the big puzzle of solving the riddle where the *heaviest* elements were actually formed.

Considering the path from the Big Bang nucleosynthesis up to iron, *stars* are the key ingredient. Stars can be seen as giant *"pressure cookers"*: They are formed from clouds of interstellar matter which contracted gravitationally to form gas balls. Under certain conditions, the inward pull of the self-gravitating gas is high enough to trigger nuclear fusion reactions in the core of the gas ball. When this gas ball has started its reaction(s), we call this ball a "star". The mass of a newly born star will (among others) determine the way how it will burn and ultimately determine its faith. The lowest end of the mass spectrum of stars (low mass stars, LMS) starts with ≈ 0.07 Solar masses (or the equivalent of ≈ 75 Jupiter masses), since at this point, the requirements to trigger the hydrogen fusion in the core are met. Stars of this mass only process hydrogen to helium and are unable to perform further processing, extinguish their nuclear burning and just cool off. In the range ≈ 0.8 Solar masses and ≈ 8 Solar masses (intermediate mass stars, IMS, including our Sun) are also able to burn the produced helium to carbon and

oxygen. After the hydrostatic hydrogen burning (the stage which our Sun is actually in), these stars start to ”pulsate”, or ignite ”flashes”, and loose their outer envelopes via stellar winds, forming the beautiful objects called ”planetary nebulae”. When the nuclear ”fuel” is consumed or densities are not sufficient any more, these stars ultimately end as ”white dwarfs”, being very hot in the beginning, but radiating their heat away and slowly cool off until they reach their surroundings temperature. Stars more massive than ≈ 8 Solar masses (high mass / massive stars, HMS) go through all stellar burning stages including hydrogen-, helium-, carbon-, neon-, oxygen-, and silicon burning, then collapse under their own weight and die in giant explosions which are commonly referred to as ”supernovae”. Supernovae might also be triggered by binary systems of intermediate mass stars when the conditions are met. However, this mechanism is completely different than the mechanism of the central collapse of massive stars. What both ”types” of these supernovae have in common is that the progenitor star gets disrupted (partially leaving a neutron star or black hole behind) and blast processed elements into the interstellar medium. Stars more massive than 300 Solar masses (the actual limit is depending on many parameters and also strongly debated) collapse directly to a black hole. Neutron stars (the name is actually misleading since they are neither purely consisting of neutrons nor are they ”stars” in the sense that they ”shine” due to nuclear processes) are very dense and interesting objects which are produced during core collapse supernovae, and if they are born in a double star system, there is a possibility that they merge with their companion. These neutron star merger events are extremely violent processes where the conditions are met for the onset of mechanisms that are able to synthesize nuclei more massive than iron. However, since they require two evolved stars being gone through all their stellar burning stages and having gone supernova, there is one striking open question about the *actual* contribution of these systems to the nucleosynthesis of heavy elements remaining: Since we already observe stars being born at an early stage of our Galaxy’s history, but neutron star mergers require

all prerequisites to be met, which takes lots of time, is the contribution of neutron star mergers possibly to late? This thesis intends to address a portion of this open question of the nucleosynthesis of the heaviest elements. In the following, the (relative or exclusive) nucleosynthesis contribution of neutron star mergers is tested as well as alternative sites for the formation of the heaviest elements, with a chemical evolution model of our Galaxy.

This thesis is organized as follows.

- In chapter one, a general introduction and the relevant nuclear/hydro physics, structure and observational properties of stars and the interstellar medium is presented. This chapter is loosely oriented on D. Arnett, "Supernovae and Nucleosynthesis" (1996), T. Padmanabhan, "Theoretical Astrophysics, Volume I: Astrophysical Processes" (2000), T. Padmanabhan, "Theoretical Astrophysics, Volume II: Stars and Stellar Systems" (2001), F. Matteucci, "The chemical evolution of the Galaxy" (2001), A. Weigert, H. J. Wendker, L. Wisotzki, "Astronomie und Astrophysik" (2006), Cowan, Thielemann & Truran, "The Nuclear Evolution of the Universe" (in prep.), and the lecture notes of nuclear astrophysics held by Thomas Rauscher (fall semester 2011 and spring semester 2012).

- Chapter two consists of a detailed explanation of our chemical evolution model and an application to the formation scenario of the heaviest elements. This chapter has been previously published in *Monthly Notices of the Royal Astronomical Society, Volume 452, 1970 ff.*, with Marco Pignatari and Friedrich-Karl Thielemann as co-authors.

- Chapter three describes the application of our model to the Draco dwarf galaxies which orbits the Milky Way.

1.2 Relevant nuclear physics

1.2.1 Basic nuclear properties

Atomic nuclei consist of protons (p) and neutrons (n). These have only slightly different masses ($m_p c^2 = 938.3$ MeV and $m_p c^2 = 939.6$ MeV). They are both spin half fermions. One of the main differences considered here is that protons are positively charged while neutrons are neutral. Usually, a nucleus containing more than one proton should be unstable due to the repelling coulomb forces of two positive charges. However, the very short range nuclear force(s) keep them together. The nuclear force(s) result in a binding energy, which has to be invested if one is willing to remove one of the nucleons from a nucleus. This binding energy $B(Z,N)$ (with Z the charge number and N the number of nucleons) is different for every nucleus and can be calculated using the difference in nuclear masses $M(Z,N)$ which can be estimated via e.g., the Bethe-Weizsäcker mass formula (cf. von Weizsäcker 1935):

$$\begin{aligned} M(Z,A) = m_u c^2 [a_v * A - a_s * A^{\frac{2}{3}} - a_c * Z(Z-1) * A^{-\frac{1}{3}} - \\ - a_{Symm} * \frac{(N-Z)^2}{4A} + \begin{cases} +a_P * A^{-\frac{1}{2}} & \text{ee-nuclei} \\ 0 & \text{ue-nuclei} \\ -a_P * A^{-\frac{1}{2}} & \text{uu-nuclei} \end{cases}] \end{aligned} \tag{1.1}$$

The coefficients discussed in detail:

- Volume term

$$a_v * A \quad \textit{with} \quad a_v \approx 15.67\ \textit{MeV} \tag{1.2}$$

  Since the Bethe-Weizsäcker formula assumes constant density in the nucleus, the volume of the nucleus is proportional to the the mass number.

- Surface term

$$-a_s * A^{\frac{2}{3}} \quad \textit{with} \quad a_s \approx 17.23\,\textit{MeV} \tag{1.3}$$

  Nucleons at the surface of the nucleus are bound less strong than those in not being at the the surface. These less bound nuclei reduce the binding energy.

- Coulomb term

$$-a_c * Z * (Z-1) * A^{-\frac{1}{3}} \quad \textit{with} \quad a_v \approx 0.714\,\textit{MeV} \tag{1.4}$$

  The repelling force of the protons decreases the binding energy.

- Symmetry term

$$-a_{\textit{Symm}} * \frac{(N-Z)^2}{4A} \quad \textit{with} \quad a_{\textit{Symm}} \approx 93.15\,\textit{MeV} \tag{1.5}$$

  This term is implied by the quantum mechanical symmetry implications. It is zero for an equal number of protons and neutrons. However, with increasingly different number of protons and neutrons, the binding energy decreases due to asymmetry.

- Pairing term

$$\begin{cases} +a_P * A^{-\frac{1}{2}} & \text{even-even-nuclei} \\ 0 & \text{uneven-even-nuclei} \\ -a_P * A^{-\frac{1}{2}} & \text{uneven-uneven-nuclei} \end{cases} \quad \textit{with} \quad a_P \approx 11.2\,\textit{MeV} \tag{1.6}$$

  This term comes from the observation that nuclei with even proton and neutron numbers are tighter bound than nuclei with uneven proton and neutron numbers.

When considering the energies and the potential of a nucleus, the shell model is very useful. In this model, it is assumed that the interaction of any nucleon

with the rest of the nucleus can be described by a spherical potential $V(r)$. This potential is represented by a well with depth W and radius R (with $R = r_0 A^{1/2}$ and $r_0 \approx 10^{-13}$ cm). The energy levels inside the potential can then be approximated by:

$$E(n,l) \approx -W + \frac{\hbar^2}{2mR^2}\left[\pi^2\left(n+\frac{l}{2}\right)^2 - l\,(l+1)\right] \tag{1.7}$$

with n and l being the quantum wave numbers of the respective state.

1.2.2 The nuclear chart and the valley of stability

A good portion of people are familiar with the periodic table of elements. This table is able to provide average mass and charge of the represented elements. However, in nuclear physics, also the information about every elements' isotopes are relevant. Therefore, nuclear physicists use the "nuclear chart". The chart's concept is very simple. It is a $2D$ array with the neutron number N on the x-axis and the charge (or proton) number on the y-axis. Every element of the chart represents one isotope. Every line represents a different element, and every column a different isotope of the respective line's element. As an example of a detail of a nuclear chart, see figure 1.1. One of the advantages of using a nuclear chart is that nuclear decays and captures can be easily illustrated. When considering a "mother nucleus" with (Z, N), all different decays and captures move the nucleus in the following directions of the nuclear chart:

- Neutron captures lead to $(Z, N+1)$ and therefore move the nucleus to the right.

- Inverse neutron captures (photodisintegration with respect to neutrons) lead to $(Z, N-1)$ and therefore move the nucleus to the left.

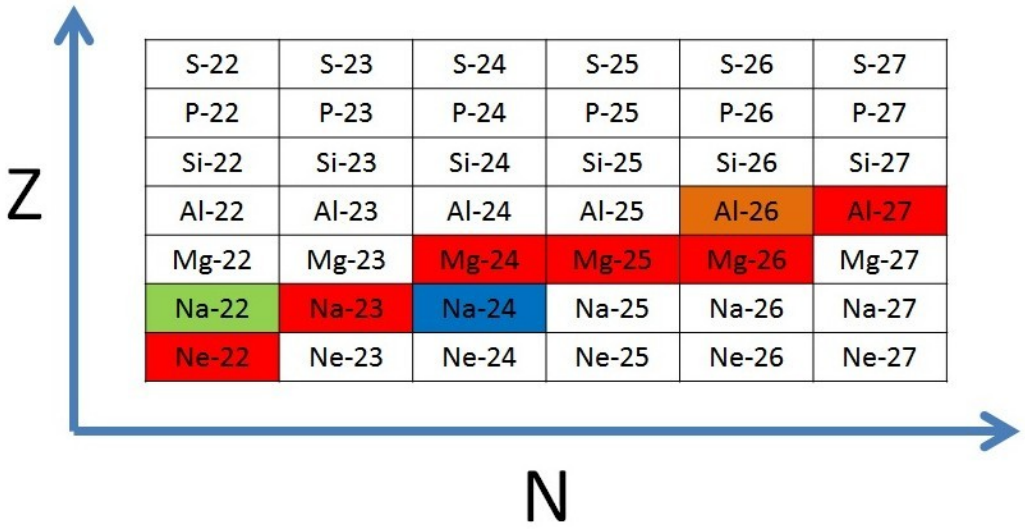

Fig. 1.1: Detail of a nuclear chart. Every element of this grid represents one isotope. On the x-axis are the neutron number and on the y-axis the proton (charge) number of the respective isotope. This snapshot represents the region of $22 \leq N \leq 27$ and $10 \leq Z \leq 16$. The red isotopes are stable, green isotopes have life times of 60 days to ten years, blue isotopes have life times between one hour and one day, brown isotopes have life times $100.000yrs \leq \tau \leq 10.000.000yrs$, while white isotopes have life times below one hour. Note the notation X-yy $\equiv {}^{yy}$X.

- Proton captures lead to $(Z+1, N)$ and therefore move the nucleus one line higher.

- Inverse proton captures (photodisintegration with respect to protons) lead to $(Z-1, N)$ and therefore move the nucleus one line below.

- α-decay is the ejection of a 2 neutron and 2 proton particle from the nucleus and therefore reduces the nucleus to $(Z-2, N-2)$, so moves it two lines down and two columns to the left.

- β^+-decay converts a proton to a neutron (under the emission of a positron and a neutrino) leading to $(Z-1, N+1)$ and therefore moves the nucleus diagonally to the lower right. The same is true for an electron capture.

- β^--decay converts a neutron to a proton (under the emission of an electron and an anti-neutrino) leading to $(Z+1, N-1)$ and therefore moves the nucleus diagonally to the upper left.

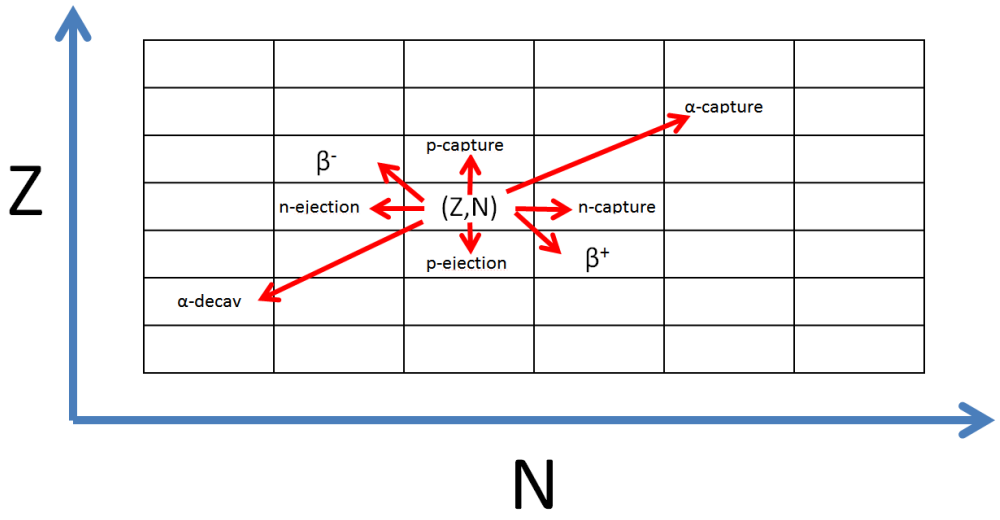

Fig. 1.2: Illustration of the the movement on the nuclear chart which a mother nucleus (Z,N) experiences under the specific decays/captures: up on proton capture, down on proton ejection, right on neutron capture, left on neutron ejection, diagonally to the upper left on β^--decay, diagonally to lower right on β^+-decay (equivalently to electron capture), diagonally to the upper right upon alpha capture, diagonally to the lower left on alpha decay.

From the discussion of the binding energy per nucleon in section 1.2.1, one can identify the isotopes with the highest binding energy among their respective element. A nuclear chart displaying actually measured binding energies can be found in figure 1.3. In a nuclear chart, one can also find the elements which are most stable against decays. These elements are situated in a specific pattern, which is referred to as ”the valley of stability”. Under standard conditions, any isotope not being on the valley of stability will decay (with the respective rate) in the direction of the valley, until it has become a stable isotope. See figure 1.3 for illustration.

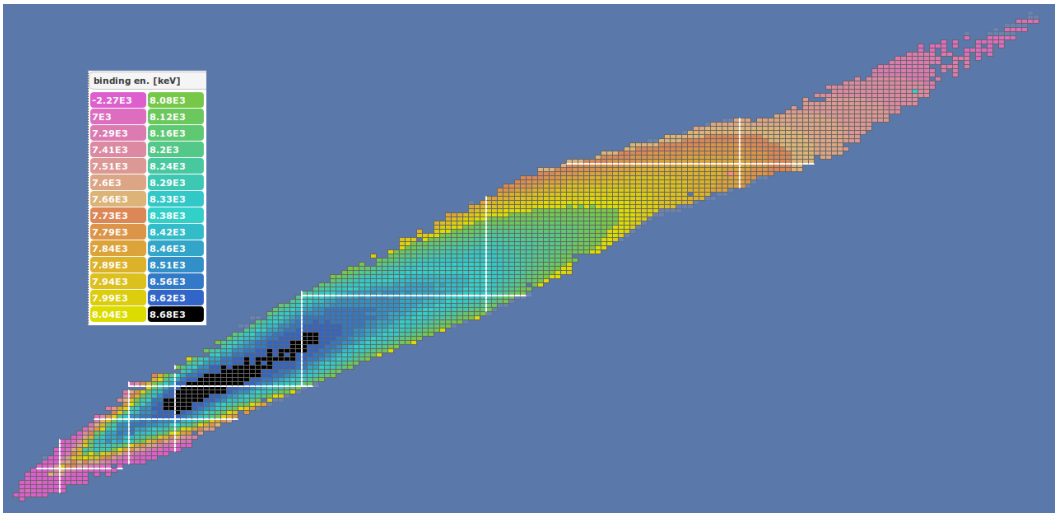

Fig. 1.3: Nuclear chart showing the binding energy of the isotopes. See legend for colour coding. Figure ©2009-2016 IAEA Nuclear Data Section.

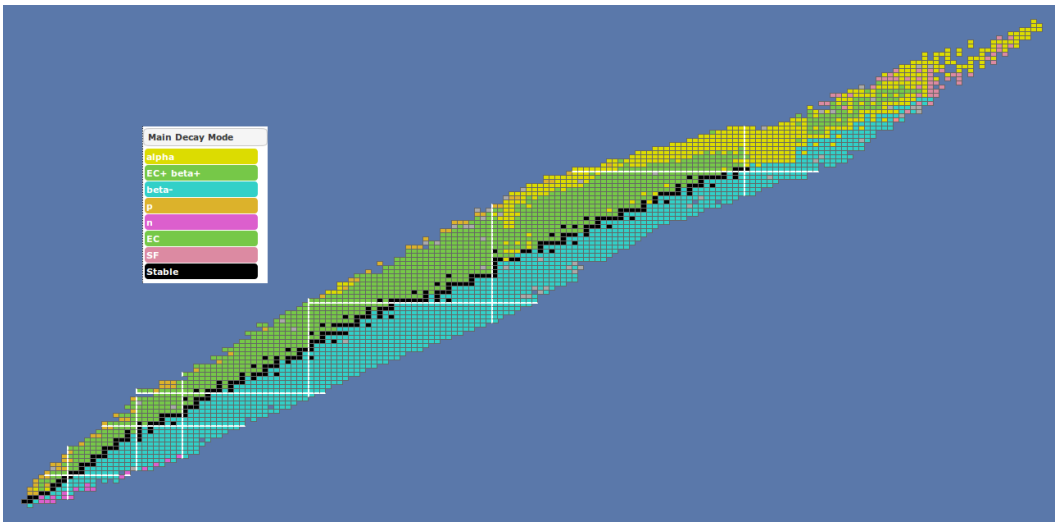

Fig. 1.4: Nuclear chart showing the valley of stability (black), and the decay modes of the nuclei. See legend for colour coding. Figure ©2009-2016 IAEA Nuclear Data Section.

1.2.3 Binding energy per nucleon and net energy release

Another implication of the considerations made in section 1.2.1 can be found when plotting the binding energy per nucleon versus the atomic mass. We can see that the binding energy per nucleon increases in a zig-zag pattern until it peaks at $A \approx 56$. When omitting the zig-zag pattern at lower mass numbers, we can make the general remark that adding a nucleon to a nucleus releases energy until the nucleus has reached $A \approx 56$, whereas it consumes energy when the nucleus is more massive than $A \approx 56$. On the other hand, if the nucleus is more massive than $A \approx 56$, the removal of a nucleon releases energy, whereas it consumes energy when the nucleus is less massive than $A \approx 56$. Accordingly, nuclear fusion might free energy until $A \approx 56$, but will consume energy beyond $A \approx 56$. On the other hand, fission (as in nuclear power plants) frees energy of heavy nuclei down to $A \approx 56$, but to further fission the nuclei beyond $A \approx 56$, the process will consume energy.

1.2.4 Nuclear-particle interactions

While having in mind the discussion of basic nuclear properties from section 1.2.1, we can think of what happens when nuclei interact with each other (or with charged particles). Since the nuclear force(s) have only very short range, the coulomb force is of more importance for the interaction of nuclei. If now a nucleus (or a charged particle in general, let us call this "a") with charge Z_2 approaches another nucleus (let us call this one "X") with Z_1, it will feel the coulomb repulsive force of $F = Z_1 Z_2 e^2/r^2$ until it comes in the range of the nuclear forces which will counteract the coulomb forces and try to keep it inside the potential well. An illustration of this can be found in figure 1.5. If the incoming nucleus a has an energy that exceeds the maximum coulomb energy, it can pass the coulomb barrier very easily, and the

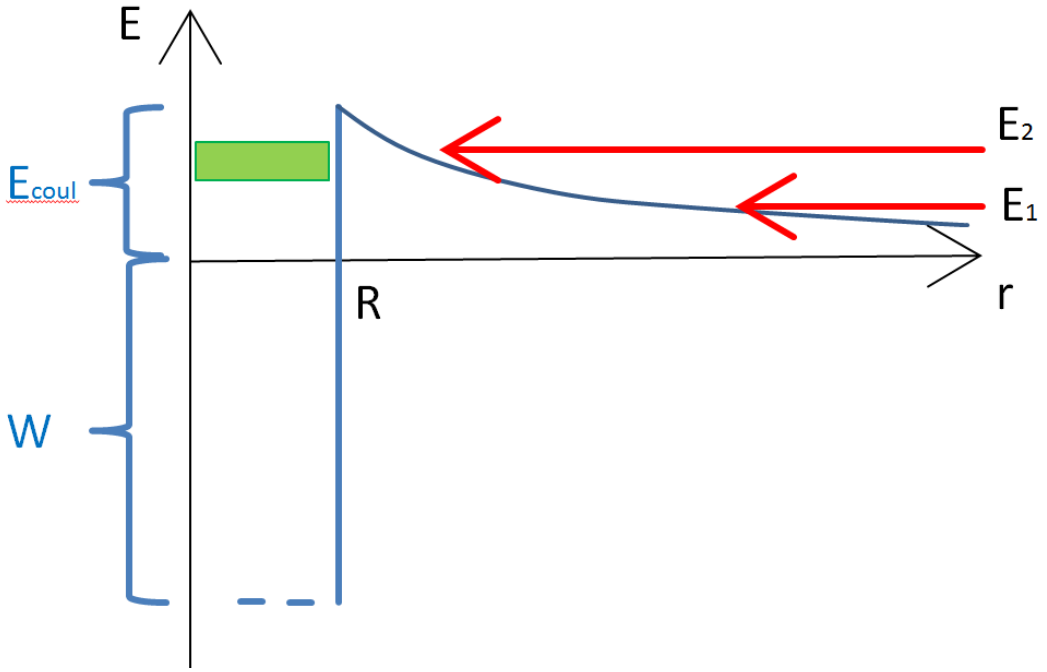

Fig. 1.5: Schematic of a simple nuclear potential well of depth W and radius R. Incoming (charged) particles (red arrows) can classically not overcome the repulsive coulomb force provided by the resident protons until they have higher energies than the barrier.

nuclear reaction is then governed by the nuclear forces. (However, this is a very rare case, since the temperature necessary to generate such high kinetic energies is of the order of 10^{10} K). Usually, when considering temperatures in stars, these are far below 10^{10}K and hence the incoming particle's kinetic energy is below the repulsive coulomb energy, so the incoming particle a will classically have no chance to come in range of the nuclear forces of the other nucleus X. However, when considering quantum mechanics, there is a small possibility to "tunnel" through the coulomb barrier and thus reach the potential well of nucleus X. When the incoming particle x has finally reached the potential well of X, the nuclear forces start to act on the a. In most cases, the nuclear forces will then trigger a reaction,

$$a + X \rightarrow Y + b \tag{1.8}$$

with Y the nucleus after the reaction and b a reaction product particle which is re-ejected from nucleus Y after the reaction. This kind of reaction is usually abbreviated as

$$X(a,b)Y \tag{1.9}$$

in nuclear physics. Often, this reaction is happening via a "compound nucleus", Z^* so that nucleus X and particle a from compound nucleus Z^* being in an excited state and then decaying to the products Y and b:

$$a + X \rightarrow Z^* \rightarrow Y + b \tag{1.10}$$

However, the compound nucleus Z^* might also decay in a different way, e.g., to (X,a), (Y,b), (G,g), (F,F), and so forth (with (X,a) being the elastic scattering of X and a); Each decay *mode* should be considered and its rate Γ_i is an individual property of the specific reaction. In either case, Z^* will be in an excited state. If an incoming particle's energy is close or at an excited state of a compound nucleus (for an illustration see green area in the well and incoming particle with energy E_2 in figure 1.5), the reaction rate will be significantly enhanced.

Cross sections of reactions are usually expressed in terms of

$$\sigma = \frac{\textit{number of reactions} * \textit{target}^{-1} * \textit{sec}^{-1}}{\textit{flux of incoming particles}} = \frac{r/n_X}{n_a v}, \tag{1.11}$$

with number densities n_X and n_a, the relative velocity v and the reaction rate (the number of reactions per cubic centimeter and second) r. If we assume (what is certainly true in a star) a velocity distribution of incoming and target particles, the rate will then be determined by the integral over the velocities multiplied by the cross section:

$$r_{X;a} = \int \sigma |\vec{v_X} - \vec{v_a}| \, dn_X \, dn_a. \tag{1.12}$$

When applying a Maxwell-Boltzmann distribution, we will obtain the following:

$$r_{X;a} = n_X n_a \int \sigma(|\vec{v_X} - \vec{v_a}|)|\vec{v_X} - \vec{v_a}|\Phi(\vec{v_X})\Phi(\vec{v_a})\, d^3v_X\, d^3v_a, \tag{1.13}$$

with

$$\Phi(\vec{v_x})\, d^3v_x = \left(\frac{m_x}{2\pi kT}\right)^{3/2} \exp\left(\frac{m_x v_x^2}{2kT}\right)\, d^3v_x. \tag{1.14}$$

Equation 1.13 can then be re-written as

$$r_{X;a} = n_X n_a \left\langle \sigma v \right\rangle_{X;a}. \tag{1.15}$$

When changing the integration constants and applying the reduced mass $\mu = m_i m_j/(m_i + m_j)$. we will obtain

$$\left\langle \sigma v \right\rangle_{X;a} = \int \sigma(v) v \left(\frac{\mu}{2\pi kT}\right)^{3/2} \exp\left(\frac{\mu v^2}{2kT}\right)\, d^3v. \tag{1.16}$$

When we now substitute $d^3v = 4\pi v^2\, dv$ and $E = 0.5\mu c^2$ in eq. 1.16, we will obtain

$$\left\langle \sigma v \right\rangle_{X;a}(T) = \left(\frac{8}{\mu\pi}\right)^{1/2} \frac{1}{(kT)^{3/2}} \int_0^\infty E\sigma(E) \exp(-E/kT)\, dE, \tag{1.17}$$

and together with eq. 1.15,

$$r_{X;a}(T) = n_X n_a \left(\frac{8}{\mu\pi}\right)^{1/2} \frac{1}{(kT)^{3/2}} \int_0^\infty E\sigma(E) \exp(-E/kT)\, dE, \tag{1.18}$$

which suits our requirements to have a reaction rate formula which is dependent on the temperature and densities of the reaction site, and the (experimentally determined) cross-sections $\sigma(E)$.

1.2.5 Nuclear statistical equilibrium

When the temperature yield kinetic particle energies which are beyond the target nucleus' repelling coulomb energy, the abundance (and reactions and their rates) equilibrate, resulting in a "nuclear statistical equilibrium" (NSE). This NSE is governed by

$$\dot{Y} = 0. \tag{1.19}$$

Since the net flow is zero, all nuclear reactions equilibrate:

$$\textit{Nucleus1}(\textit{Particle1}, \textit{Particle2})\textit{Nucleus2}, \tag{1.20}$$

and their chemical potential equals (with $\mu'_x = \mu_x + m_x c^s$),

$$N_1\mu'_1 + N_2\mu'_2 = N_3\mu'_3 + N_4\mu'_4 \tag{1.21}$$

Let us now consider the "easiest" reactions to move the nucleus in the nuclear charts, proton and neutron captures (and their respective inverse) to be in an equilibrium, this yields

$$\begin{aligned} &\mu'(Z,N) + \mu'_n = \mu'(Z,N+1) \quad \textit{for neutron capture, and} \\ &\mu'(Z,N) + \mu'_p = \mu'(Z+1,N) \quad \textit{for proton capture, with} \\ &N\mu'_n + Z\mu'_p = \mu'(Z,N). \end{aligned} \tag{1.22}$$

Given a Maxwell-Boltzmann distribution of particles, this yields

$$\begin{aligned} & kT * \ln\left[\frac{\rho N_A Y_{(Z,N)}}{G_{(Z,N)}}\left(\frac{2\pi\hbar^2}{m_{(Z,N)}}\right)\right]^{\frac{3}{2}} + m_{(Z,N)}c^2 = \\ = \;& N\left[kT * \ln\left[\frac{\rho N_A Y_n}{G_n}\left(\frac{2\pi\hbar^2}{m_n}\right)\right]^{\frac{3}{2}} + m_n c^2\right] + Z\left[kT * \ln\left[\frac{\rho N_A Y_p}{G_p}\left(\frac{2\pi\hbar^2}{m_p}\right)\right]^{\frac{3}{2}} + m_p c^2\right] \\ \Leftrightarrow \;& \ln\left[\frac{\rho N_A Y_{(Z,N)}}{G_{(Z,N)}}\left(\frac{2\pi\hbar^2}{m_{(Z,N)}}\right)\right]^{\frac{3}{2}} - N\ln\left[\frac{\rho N_A Y_n}{G_n}\left(\frac{2\pi\hbar^2}{m_n}\right)\right]^{\frac{3}{2}} + Z\ln\left[\frac{\rho N_A Y_p}{G_p}\left(\frac{2\pi\hbar^2}{m_p}\right)\right]^{\frac{3}{2}} = \\ = \;& \frac{1}{kT}\underbrace{\left(Nm_n c^2 + Zm_p c^2 - m_{(Z,N)}c^2\right)}_{\textit{Binding energy} =: B}. \end{aligned} \tag{1.23}$$

Recalling

$$A = N + Z, \tag{1.24}$$

and considering

$$m_n \approx m_m, \tag{1.25}$$

yields

$$m_{(Z,N)} = A * m_n. \tag{1.26}$$

Let us solve equation 1.23 for $Y_{(Z,N)}$:

$$Y_{(Z,N)} = G_{(Z,N)} \left(\rho N_A\right)^{A-1} \frac{A^{3/2}}{2^A} \left(\frac{2\pi\hbar^2}{Z^A}\right)^{\frac{3}{2}(A-1)} e^{\frac{B_{(Z,N)}}{kT}} * Y_n^N Y_p^Z. \tag{1.27}$$

This equation is the so-called **first NSE equation**. Mass conservation considerations yield the **second NSE equation**:

$$\sum_i X_i = 1 \Leftrightarrow \sum_i A_i Y_i = 1, \tag{1.28}$$

and charge conservations yields the **third NSE equation**:

$$\sum_i Z_i Y_i = Y_e. \tag{1.29}$$

Let us now derive some of the most important outcomes regarding the abundances of nuclei in a statistical equilibrium:

$$Y_{(Z,N)} = \ldots \left(\rho N_A\right)^{A-1} \ldots, \tag{1.30}$$

resulting in, high density yields heavy nuclei;

$$Y_{(Z,N)} = \ldots \left(\frac{2\pi\hbar^2}{Z^A}\right)^{\frac{3}{2}(A-1)} \ldots, \tag{1.31}$$

consequently, high temperature yields light nuclei;

$$Y_{(Z,N)} = \ldots e^{\frac{B_{(Z,N)}}{kT}} \ldots, \tag{1.32}$$

with neither temperature nor densities being high, nuclei with high binding energy are favoured.

1.2.6 The r-process

In some astrophysical sites, temperatures and neutron densities are high enough to set on the rapid neutron capture process (r-process). In this process, nuclei (Z, N) quickly capture neutrons via a (n, γ) reaction, hence increase their N and move to the right on the nuclear chart. This process is in equilibrium with the (γ, n) photodisintegration process, which removes neutrons from the nucleus, say, decreasing its N and thus moving it to the left on the nuclear chart. The isotope with the highest abundance in this equilibrium will then be the isotope with the lowest cross sections for the aforementioned reactions.

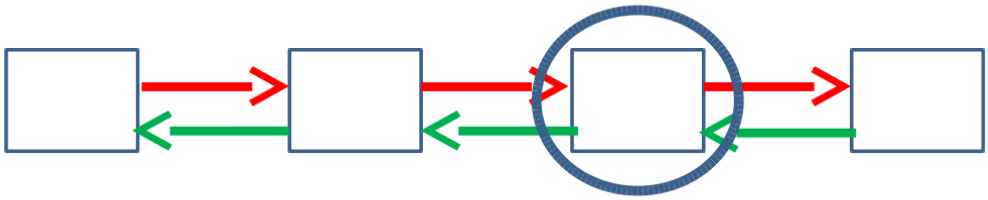

Fig. 1.6: Illustration of the (n, γ), (γ, n) equilibrium on a nuclear chart. The blue boxes represent different isotopes on an r-process path on a nuclear chart. Red arrows represent the effect of the (n, γ) neutron capture process on the nucleus, whereas green arrows represent the effect of the (γ, n) photodisintegration. The isotope which is marked with a blue circle is the "waiting point", with the highest abundance of nuclei in this line of the r-process path.

From this most abundant isotope, the nucleus might perform a β^--decay, shifting the nucleus towards the upper left in the nuclear chart. From here on, the nucleus gets again into the equilibrium of neutron capture and (γ, n) photodisintegration.

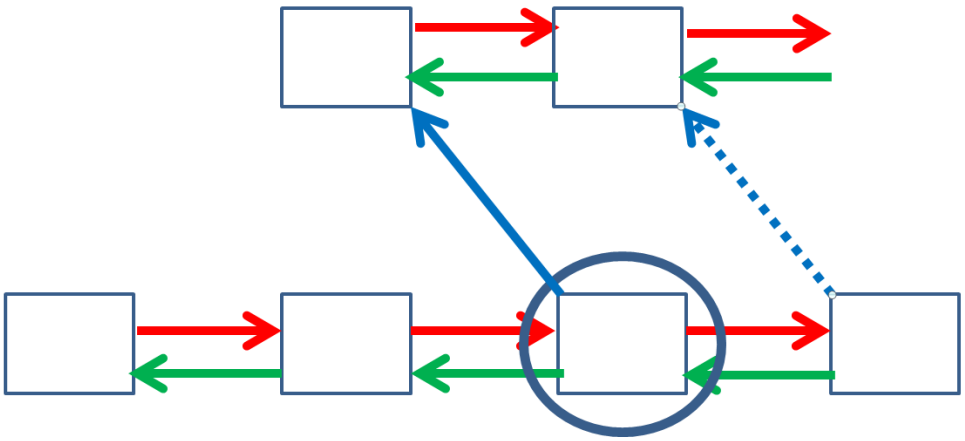

Fig. 1.7: Illustration of a short portion of an r-process path on a nuclear chart. The blue boxes represent different isotopes on an r-process path on a nuclear chart. Red arrows represent the effect of the (n, γ) neutron capture process on the nucleus, whereas green arrows represent the effect of the (γ, n) photodisintegration. The isotope which is marked with a blue circle is the "waiting point", with the highest abundance of nuclei in this line of the r-process path. From here on, nuclei perform a β^--decay (blue arrow; with probably some paths of minor relevance originating from neighbouring nuclei, dashed blue arrow line), increasing the nucleus' Z but decreasing its N (through the conversion of a neutron to a proton), shifting it to the upper left. From here on, it comes into the (n, γ), (γ, n) equilibrium in the next line of the nuclear chart.

This process happens over and over again, and the result is a zig-zag-like path far on the neutron-rich side of the nuclear chart. Once the conditions of the r-process (excess neutron abundance / temperature) are waived, the nuclei on the path do not follow it any more. Instead they perform multiple β^--decays until they reach the valley of stability. The elements produced in this manner are usually referred to as r-process elements.

1.3 Basic stellar hydrostatics

1.3.1 Lagrange coordinates

When considering the radius of a star, the use of "Lagrange coordinates" is more practical than using standard Cartesian coordinates. These coordinates are defined by the enclosed mass of the star, with the following transformations:

$$\frac{\partial}{\partial r} = \frac{\partial}{\partial m}\frac{\partial m}{\partial r}. \tag{1.33}$$

Considering a gas sphere with

$$m(r) = \frac{4}{3}r^3\pi\rho, \tag{1.34}$$

we can find

$$\frac{\partial m}{\partial r} = 4\pi\rho r^2, \tag{1.35}$$

and

$$\frac{\partial r}{\partial m} = \frac{1}{4\pi\rho r^2}. \tag{1.36}$$

1.3.2 Basic equations of stellar hydrostatics

Stellar hydrostatics (in 1D) are in general governed by three main equations.

1. Since a star can be considered as a spherically symmetric gas ball, the relation between enclosed mass and density yields:

$$dm(r) = \rho\, dV = \rho(r) * 4\pi\rho r^2\, dr \Leftrightarrow \frac{dm(r)}{dr} = 4\pi\rho r^2\rho(r). \tag{1.37}$$

2. Considering gravitation and pressure acting on an enclosed shell inside a star,

$$dF_{grav} = \frac{-Gm(r)\,dm}{r^2} \tag{1.38}$$

$$dF_{press} = \underbrace{[P(r) - P(r+\,dr)]}_{-\,dP=:\textit{pressure gradient}} * dA, \tag{1.39}$$

together with Newton's second law of motion,

$$F = m * a = m * \ddot{x}, \tag{1.40}$$

we can find the acceleration acting on a mass element of the shell:

$$dF_{tot} = \, dF_{grav} + \, dF_{press} = \, dm * \ddot{r} = \frac{dm * \, d^2r}{dt^2}. \tag{1.41}$$

This leads to

$$\begin{aligned} &\frac{dP(r)}{dr} = -\frac{\rho G m(r)}{r^2} - \rho\frac{d^2r}{dt^2} \quad \textit{for Euler coordinates, and} \\ \Leftrightarrow &\frac{dP}{dm} = -\frac{Gm}{4\pi r^4} \quad \textit{for Lagrange coordinates, respectively.} \end{aligned} \tag{1.42}$$

3. Equation of state (EOS): Considering the star behaves according to a barotropic EOS, $P = P(\rho)$, often it follows a polytropic EOS,

$$P = \kappa\rho^{\theta} = \kappa\rho^{1+\frac{1}{n}}, \tag{1.43}$$

with κ being the polytropic constant, θ the polytropic exponent and n the polytropic index (with $x\epsilon\mathbb{R}$).

1.3.3 Lane-Emden equation

Plugging the poisson equation in a polytropic ESO yields

$$\begin{aligned}\Delta P(r) &= \frac{1}{r^2}\frac{d}{dr}\left(\frac{r^2}{\rho}\frac{dP}{dr}\right) \overbrace{=}^{\text{eq. 1.42}} \frac{1}{r^2}\frac{d}{dr}\left(-Gm(r)\right) = \\ &= \frac{1}{r}\left(-Gm\frac{dm}{dr}\right) \overbrace{=}^{\text{eq. 1.37}} -\frac{1}{r^2}G4\pi r^2\rho = -4\pi\rho G.\end{aligned} \tag{1.44}$$

The following *Ansatz* will help us to solve this differential equation:

$$\rho(r) = \rho_c\Phi^n(\chi), \tag{1.45}$$

with χ being

$$\chi = \frac{r}{a_n}, \textit{ with} \quad a_n = \left[\frac{(n+1)K\rho_c^{\frac{1-n}{n}}}{4\pi G}\right]^{\frac{1}{2}}. \tag{1.46}$$

The resulting equation is the Lane-Emden equation:

$$\frac{1}{\chi^2}\frac{d}{d\chi}\left(\chi^2\frac{d\Phi}{d\chi}\right) = \Phi^n(\chi), \tag{1.47}$$

with $\Phi^n(\chi)$ being the structural function, ρ_c the central density, and the boundary conditions

$$\Phi(0) = 1, \quad \Phi\left(\frac{R}{a}\right) = 0, \quad \left[\frac{d\Phi}{d\chi}\right]_{\chi=0} = 0. \tag{1.48}$$

1.3.4 Chandrasekhar limit

Starting from the Lane-Emden equation (eq. 1.47), we calculate the radius R of a star,

$$R = a_n\rho_c^{1-\frac{n}{2n}}\chi_n, \tag{1.49}$$

with n being the number of the analytic solution of the Lane-Emden equation. The total stellar mass yields

$$M = \int_0^R 4\pi r^2 \rho \, dr. \tag{1.50}$$

Now express ρ in terms of Φ,

$$M = -4\pi \left(\frac{(n+1)K}{4\pi G} \right)^{\frac{3}{2}} * \rho_c^{3-\frac{n}{2n}} * \left(\chi^2 \frac{d\Phi}{d\chi} \right). \tag{1.51}$$

NB. If we choose a polytropic EOS with $n = 3$, ρ_c vanishes from the above equation. Together with , this leads to an undefined radius for the star. The physical consequence is that the radius of a star in this condition is vulnerable to even smallest perturbations.

An application of this can obtained considering the radius of a white dwarf (cf. section 1.7), when combining the equations for mass and radius (eqs. 1.51 & 1.49),

$$M = 0.7011 \left(\frac{R}{10^4 km} \right)^{-3} (2Y_e)^5 \, M_\odot; \tag{1.52}$$

When we now plug in a polytropic EOS with index $n = 3/2$, we get

$$M_3 = -2.01824 * 4\pi * \left(\frac{K}{\pi G} \right)^{\frac{3}{2}} \overbrace{=}^{\textit{Fermi gas}} 3.062 \left(\frac{\hbar c}{G} \right)^{\frac{3}{2}} (2Y_e)^2 \, M_\odot. \tag{1.53}$$

This mass is called "Chandrasekhar mass". Once a massive star's iron core reaches this mass, it will not be able to withstand its own weight anymore and contracts. This case will be discussed in section 1.5.

1.4 Stellar burning stages

The (hydrostatical) stellar burning consists of multiple stages: hydrogen-, helium-, carbon-, neon-, oxygen-, and silicon burning. The end point of the (hydrostatical) stellar burning is when iron is produced, since it has the highest binding energy per nucleon. Hence, beyond iron, energy cannot be released via fusion reactions. In the following, we will discuss the (hydrostatical) stellar burning in detail.

1.4.1 Hydrogen burning

At the beginning of the main sequence burning stage, stars mainly burn hydrogen to helium. In total, four hydrogen nuclei are consumed and one Helium nucleus is produced. This reaction consists of two major paths: PP-chains which are direct fusion reactions, or CNO-cycles which are ”catalytic” reactions which become more important as the temperature of the star and the abundance of the catalytic nuclei grows. Under solar conditions, PP-chains dominate the reaction flow by a factor of ≈ 10. The main reactions of the PP-cycles are in principle:

cycle	reaction	$\tau(years)$	$Q(MeV)$
PPI	${}^1H(p, e^+\nu)^2H$	$7.9 * 10^9$	0.420
	${}^1H(pe^-, \nu)^2H$	$1.9 * 10^{12}$	1.442
	${}^2H(p, \gamma)^3He$	$4.4 * 10^{-8}$	5.493
	${}^3He({}^3He, 2p)^4He$	$2.4 * 10^5$	12.859
PPII	${}^3He(\alpha, \gamma)^7Be$	$9.7 * 10^5$	1.586
	${}^7Be(e^-, \nu)^7Li$	$3.9 * 10^{-1}$	0.861
	${}^7Li(p, \alpha)^4He$	$1.8 * 10^{-5}$	17.347
PPIII	${}^7Li(p, \gamma)^8B$	$6.6 * 10^1$	0.135
	${}^8B(e^+\nu)^8Be^*(\alpha)^4He$	$3 * 10^{-8}$	18.078

Tab. 1.1: PP cycles in the hydrostatic hydrogen burning. The PPI-reaction is the most common one. The PPII-reaction branches from the PPI-reaction at ^{3}He. The PPIII reaction branches from the PPII-reaction at ^{7}Li.

Where the reaction ${}^1H(pe^-, \nu)^2H$ (pep-reaction) is by far the slowest. The main problem is that the probability of having three particles $(2 * p + e^-)$ at the same place in the same moment is very low, so that during the time that the first two educts are in the same spot, also the third one has to join after a very short time. Since densities are not too high in the hydrogen burning, it is very difficult to find three different particles in the very same spot. Thus, the possibility of a reaction of these three educts simultanously is very rare. Since this reaction is the limiting factor for the total reaction path, and all reactions follow immediately (compared to the time scale of the pep-reaction), this situation is called a steady flow equilibrium. If we

consider only the one reaction as the limiting factor, we can find the reaction flow for the respective branches:

$$\begin{aligned} C_I &= \frac{1}{2}\rho N_A \langle 3,3\rangle Y_3^3 \\ C_{II} &= -\rho N_A \langle 3,4\rangle Y_3 Y_4 + 2\rho N_A \langle 1,7^*\rangle Y_1 Y_7 * \\ C_{III} &= 2\lambda_8 Y 8 \\ C &= C_I + C_{II} + C_{III} \end{aligned} \tag{1.54}$$

If one assumes $\dot{Y} = 0$ for all intermediate nuclei, one can calculate the energy generation:

$$\dot{\epsilon} = -N_A \sum_i \dot{Y}_i m_i c^2 = N_A C * (4m_p - m_\alpha)c^2 = N_A C Q_{\text{H-burning}}. \tag{1.55}$$

For the CNO-cycles, the reaction paths are as follows.

cycle	reactions
CNOI	$^{12}C(p,\gamma)^{13}N(e^+\nu)^{13}C(p,\gamma)^{14}N(p,\gamma)^{15}O(e^+,\nu)^{15}N(p,\alpha)^{12}C$
CNOII	$^{15}N(p,\gamma)^{16}O(p,\gamma)^{17}F(e^+,\nu)^{17}O(p,\alpha)^{14}N$
CNOIII	$^{17}O(p,\gamma)^{18}F(e^+,\nu)^{18}O(p,\alpha)^{15}N$
CNOIV	$^{18}O(p,\gamma)^{19}F(p,\alpha)^{16}O$

Tab. 1.2: Main reactions of the CNO-cycle. The CNOI-cycle is the most common one. The CNOII-cycle branches from the CNOI-cycle at ^{15}N. The CNOIII-cycle branches from the CNOII-cycle at ^{17}O, the CNOIV-cycle branches from the CNOIII-cycle at ^{18}O.

In the CNO-cycle the reaction $^{14}N(p,\gamma)^{15}O$ has the smallest reaction rate which leads to the fact that the most abundant nucleus in the reaction chain is ^{14}N, with $Y_{14}^{\odot} = \frac{1.4*10^{-2}}{14}$ and the abundances of all other nuclei remain negligible. (This is often referred to as "bottleneck reaction, since at

this reaction, most nuclei "wait" until they react further, and therefore the abundance in the nucleus "before" the reaction is higher.) Hence,

$$C_{CNO} = \rho N_A \langle 14,1 \rangle Y_{14} Y_1 \tag{1.56}$$

and

$$\begin{aligned}
\dot{Y}_1 &= \rho N_A \langle 12,1 \rangle Y_{12} Y_1 - \rho N_A \langle 13,1 \rangle Y_{13} Y_1 - \rho N_A \langle 14,1 \rangle Y_{14} Y_1 - \rho N_A \langle 15,1 \rangle Y_{15} Y_1 \\
&= -4 C_{CNO} = -4 \rho N_A \langle 14,1 \rangle Y_{14} Y_1 = -\frac{1}{\tau_{1,14}} Y_1 \\
\dot{Y}_4 &= \rho N_A \langle 15,1 \rangle Y_{15} Y_1 = C_{CNO}
\end{aligned} \tag{1.57}$$

For the energy generation:

$$\dot{\epsilon} = N_A C_{CNO} Q_{H\text{-}burning} \tag{1.58}$$

Since densities in the hydrostatic burning stages are low enough to let neutrinos escape freely, they will carry away energy whenever they are produced in a reaction. This leads to a total neutrino loss of $\approx 6.3\%$ during the hydrogen burning. Typical values of the hydrogen burning in a $25 M_\odot$ star are temperatures of the order of $T_9 = 0.06$, densities of $\rho \approx 5$ g cm^{-3}, and a time scale of $\tau \approx 7 * 10^6$ years.

1.4.2 Helium burning

Since there is no stable $A = 5$ nucleus, stellar burning cannot continue the hydrogen burning, e.g., adding a hydrogen nucleus / proton to a helium nucleus. Also reactions with the ashes are quite complicated, e.g., for the case $^3He(^4He, \gamma)^7Be$, the newly produced ^7Be nucleus will decay to ^7Li, which will then be destroyed via a sub-reaction of the PPII hydrogen burning reaction,

$^7Li(p,\alpha)^4He$ (see table 1.1). The only possibility is the fusion of two ^3He, creating an equilibrium with the unstable ^8Be nucleus:

$$^4He + {}^4He \rightleftarrows {}^8Be \tag{1.59}$$

Since the reaction is in an equilibrium, it does not change its abundance (whereas the life time is determined by the width of the ground state via the Heisenberg uncertainty principle):

$$\begin{aligned} \dot{Y}_8 &= \rho N_A \langle 4,4\rangle Y_4^2 - \lambda_8 Y_8 = 0 \\ \lambda_8 &= \frac{1}{\tau_8} \quad \Gamma_8 \tau_8 = \hbar \quad \lambda_8 = \frac{\tau_8}{\hbar}. \end{aligned} \tag{1.60}$$

Thus,

$$Y_8 = \frac{\hbar}{2\Gamma_8} \rho N_A \langle 4,4\rangle Y_4^2 \tag{1.61}$$

In the rare case where a third ^4He joins the ^8Be during its short life time, the reaction $^8Be(\alpha,\gamma)^12C$ can occur. Hence, the total reaction yields:

$$3 * {}^4He \rightarrow {}^{12}C \quad Q = 6.445\ MeV, \tag{1.62}$$

which is commonly referred to as "triple-alpha" reaction due to the three α ($= {}^4He$) particles involved. The abundance change in ^{12}C can then be written as

$$\begin{aligned} \dot{Y}_{12} &= \rho N_A \langle 4,8\rangle Y_4 Y_8 \\ &= \frac{\hbar}{2\Gamma_8} \rho^2 N_A^2 \langle 4,4\rangle \langle 4,8\rangle Y_4^3 \\ &= \frac{1}{3!} \rho^2 N_A^2 \langle 4,4,4\rangle Y_4^3 \end{aligned} \tag{1.63}$$

From the product ^{12}C on, an additional alpha capture can occur,

$$^{12}C(\alpha,\gamma)^{16}O \quad Q = 7.161\ MeV; \tag{1.64}$$

From here on, the cross-sections for alpha captures on ^{16}O are too low, so the ashes of the helium burning are ^{12}C and ^{16}O. Unfortunately the cross section of the $^{12}C(\alpha,\gamma)^{16}O$ reactions are not well determined experimentally (due to

the overlap of resonances), so this rate and hence the ratio of $Y_{^{12}C}/Y_{^{16}O}$ at the end of the helium burning remains one of the largest issues in nuclear astrophysics. Typical values of the helium burning in a $25M_{\odot}$ star are temperatures of the order of $T_9 = 0.23$, densities of $\rho \approx 7 * 10^2$ g cm^{-3}, and a time scale of $\tau \approx 5 * 10^5$ years.

1.4.3 Carbon burning

When a star is massive enough (usually $> 8M_{\odot}$ are assumed) to further increase the temperature by contraction at the end of the helium burning, the carbon burning can be ignited. The two main reactions are:

$$\begin{aligned} &^{12}C(^{12}C,\alpha)^{20}Ne \quad Q = 4.62\ MeV \\ &^{12}C(^{12}C,p)^{23}Na \quad Q = 2.24\ MeV. \end{aligned} \tag{1.65}$$

The products might then react further via

$$\begin{aligned} &^{23}Na(p,\alpha)^{20}Ne \\ &^{23}Na(p,\gamma)^{24}Mg \\ &^{12}C(\alpha,\gamma)^{16}O. \end{aligned} \tag{1.66}$$

Typical values of the carbon burning in a $25M_{\odot}$ star are temperatures of the order of $T_9 = 0.93$, densities of $\rho \approx 2 * 10^5$ g cm^{-3}, and a time scale of $\tau \approx 600$ years.

1.4.4 Neon burning

Since the star further contracts, raises the temperature and density, at this burning stage the photodisintegration of ^{20}Ne will occur under the releas of

an alpha particle which will then be recycled to further fusion another ^{20}Ne nucleus and its product:

$$\begin{aligned} &^{20}Ne(\gamma,\alpha)^{16}O \\ &^{20}Ne(\alpha,\gamma)^{24}Mg(\alpha,\gamma)^{28}Si. \end{aligned} \tag{1.67}$$

Typical values of the neon burning in a $25M_{\odot}$ star are temperatures of the order of $T_9 = 1.7$, densities of $\rho \approx 4 * 10^6$ g cm^{-3}, and a time scale of $\tau \approx\approx 1$ year.

1.4.5 Oxygen burning

In this burning stage, the oxygen which was produced in the preceeding burning stages will now serve as an educt for further fusion. The main reactions are as follows:

$$\begin{aligned} &^{16}O(^{16}O,p)^{31}P && Q = 7.676\ MeV \\ &^{16}O(^{16}O,\alpha)^{28}Si && Q = 9.593\ MeV \\ &^{16}O(^{16}O,n)^{31}S(\beta^+)^{31}P && Q = 1.459\ MeV, \end{aligned} \tag{1.68}$$

and the ^{31}P will then perform a (p,α) reaction and thus yield $^{31}P(p,\alpha)^{28}Si$. Typical values of the oxygen burning in a $25M_{\odot}$ star are temperatures of the order of $T_9 = 2.3$, densities of $\rho \approx 1 * 10^7$ g cm^{-3}, and a time scale of around six months.

1.4.6 Silicon burning

The silicon burning starts with the photodisintegration of silicon nuclei to obtain free alpha particles, neutrons and protons. Then, the abundance of nuclei will transform in two major quasi-statistical equilibria around silicon and iron, and transform into an NSE at later stages of the silicon burning. Its main product is ^{56}Ni which decays to ^{56}Fe on short time scales and marks the

end of the evolution of a massive star. Typical values of the silicon burning in a $25M_{\odot}$ star are temperatures of the order of $T_9 = 4.1$, densities of $3 * 10^7$ g cm^{-3}, and a time scale of one day.

1.5 Core-collapse supernovae

1.5.1 Collapse phase

At the end of the silicon burning, the massive star has reached a central density of $4 * 10^{10} < \rho_C < 10^{11} gcm^{-3}$, a core temperature of $(8 - 10) * 10^{10}$ K, which corresponds to an electron Fermi energy of $E_F^{e^-} = 6$ MeV. When enough iron is produced to let the iron core exceed the "Chandrasekhar mass" (cf. section 1.3.4),

$$M_{Ch}(Y_e, S_e) = 1.44(2Y_e)^2 \left[1 + \left(\frac{S_e}{\pi Y_e}\right)^2\right] M_\odot \tag{1.69}$$

the radius of the core is not well defined any more and therefore vulnerable to any perturbation. Since the Fermi energy of the electrons further increases, electron captures are caused:

$$p(e^-, \nu_e)n, \quad \textit{thus} \quad (Z, A)(e^-, \nu_e)(Z - 1, A), \tag{1.70}$$

hence the electron pressure decreases which leads to a contraction of the core. Additionally, an energy loss due to the freely escaping neutrinos affects the core. Due to high temperatures in this stage of the evolution of the massive star, photons with sufficiently high energies are available to photodisintegrate parts of the iron core:

$$Fe + \gamma \rightarrow 13\alpha + 4n \quad Q = -124.4\, MeV \tag{1.71}$$

This process absorbs the high energetic γ and therefore further decreases the radiation pressure. This accelerates the collapse of the core (see left panel of figure 1.8). Hence, the density in the core is increased. When a density of $\rho_0/20$ ($\rho_0 = 2.7 * 10^{14} g\ cm^{-3}$) is reached, nucleons only exist in a "soup of particles". Beyond ρ_0, nuclei get completely disrupt and split into their constituents. At this point, also a phase transition from a Maxwell-Boltzmann

gas to a nonrelativistic, degenerate Fermi gas occurs. Since the high energetic photons who prevented the star from collapsing are absorbed, all stellar matter is falling inwards (see right panel of figure 1.8). As the inner shells travel with a velocity proportional to r, the inner shells' velocity overcomes the local speed of sound. Since the "information" about the contraction is only able to travel through the matter with the speed of sound, there is no more interaction between the shells possible. This leads to a "decoupling" of the shells, where one shell has no pressure information of another shell, hence their collapse and inward fall happen completely independent. This leads to a density rush in the core. When a density of ρ_t is reached, the neutrinos are suddenly trapped inside the core due to elastic scattering

$$\nu + e^- \rightleftarrows \nu + e^-, \tag{1.72}$$

and cannot escape freely any more. This suddenly establishes a neutrino pressure, and the electron and neutrino captures come to an equilibrium:

$$e^- + p \rightleftarrows n + \nu_e. \tag{1.73}$$

The lepton fraction will remain constant (with typical values in the range of of $0.36 < Y_L < 0.38$). This leads to a constant electron abundance, which automatically leads to a constant Chandrasekhar mass via equation 1.69, with a typical mass of $M_{Ch} = 0.8 M_\odot$. At this stage, the innermost core exceeds the nuclear density $\rho_0 (= 2 * 10^{14} g cm^{-3})$. When such densities are reached, particles are close enough to be in the range of each others repelling (strong) nuclear force. The result is a sudden stiffening of the compressibility of the innermost portion of the core, decelerating the collapse, triggering a reversely oriented "core-bounce" .

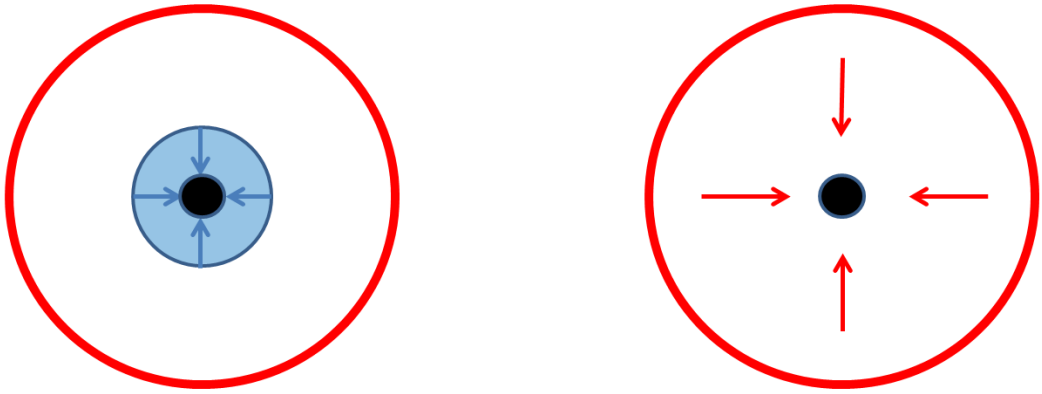

Fig. 1.8: Schematic of the collapse phase of a massive star. Left panel: The iron core (light blue) collapses to a proto-neutron star (black). Right panel: The outer layers of the star fall towards the inner layers.

1.5.2 Prompt-stalled-revived shock and neutrino burst

Since the core promptly increases its pressure due to (strong) nuclear forces after the nuclear density is reached, a shock wave towards the outer layers will be launched. The shock wave travels in the direction of the outer layer of the star, until the neutrino sphere is reached (this is the point where the density of matter is lower than the neutrino trapping density). From here, neutrinos can escape freely, generating a sudden burst in the neutrino flux. Since the neutrinos can travel with very low cross sections through the outer layers of the star, this neutrino burst is much earlier visible to the far away observer than the actual (optical) blast. Hence, this neutrino burst - when observed by a neutrino telescope - is a good messenger of an upcoming supernova. The (matter) shock looses energy on its way towards the outer layers. This is due to (elastic) scattering with the (still) in-flowing material from the outer layers, as well as the huge entropy differences in the shock front, and the loss of energy due to the freely escaping neutrinos (beyond the neutrino sphere). The shock front travels through $\approx 1.1 M_{\odot}$ of stellar matter in $30 - 110$ milliseconds, until its kinetic energy is exhausted and it stalls (e.g., Burrows et al. 1995). From this point on, "cooling neutrinos" can escape the core and decrease its temperature. These neutrinos will then

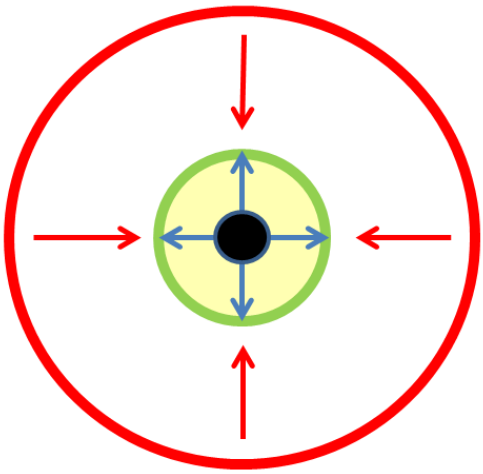

Fig. 1.9: Schematic of the stalled shock during a supernova. The shock front (green) travels outwards but is stalled due to the still infalling matter from outer layers of the star (red arrows).

scatter at the stalled shock front on their way towards the outer layers of the star, causing an increase in energy in the shock front and thus revive it. When the shock front reaches the outer layers of the star, one can finally observe the disruption of the outer layers, leaving behind the naked core, the newly born proto-neutron star (e.g., Janka & Müller 1996).

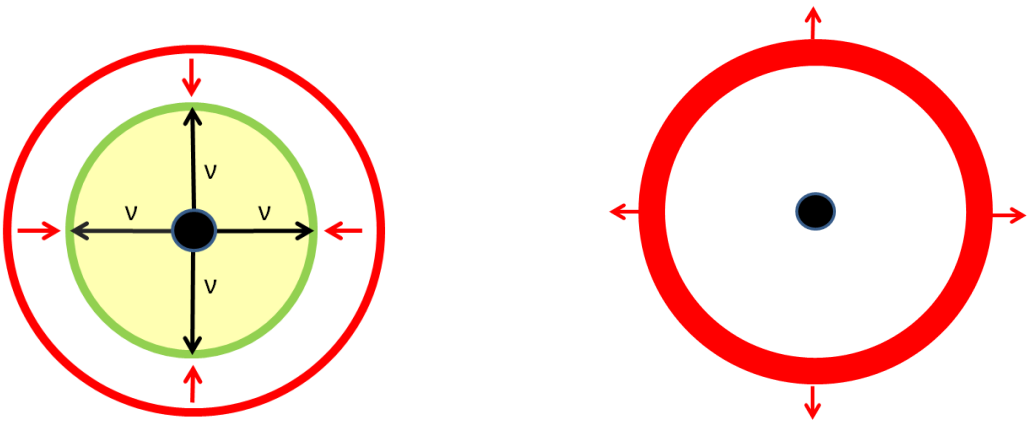

Fig. 1.10: Left panel: Schematic of the neutrino heating effect. Neutrinos (ν, black arrows) are cooling the core, travel outwards and interact with the stalled shock front (green). The deposited energy revives the shock which then overcomes the counterflow of inwards falling outer star layers (red arrows). Right panel: Once the shock front has reached the stellar surface, the star is blown apart. The proto-neutron star (black) remains.

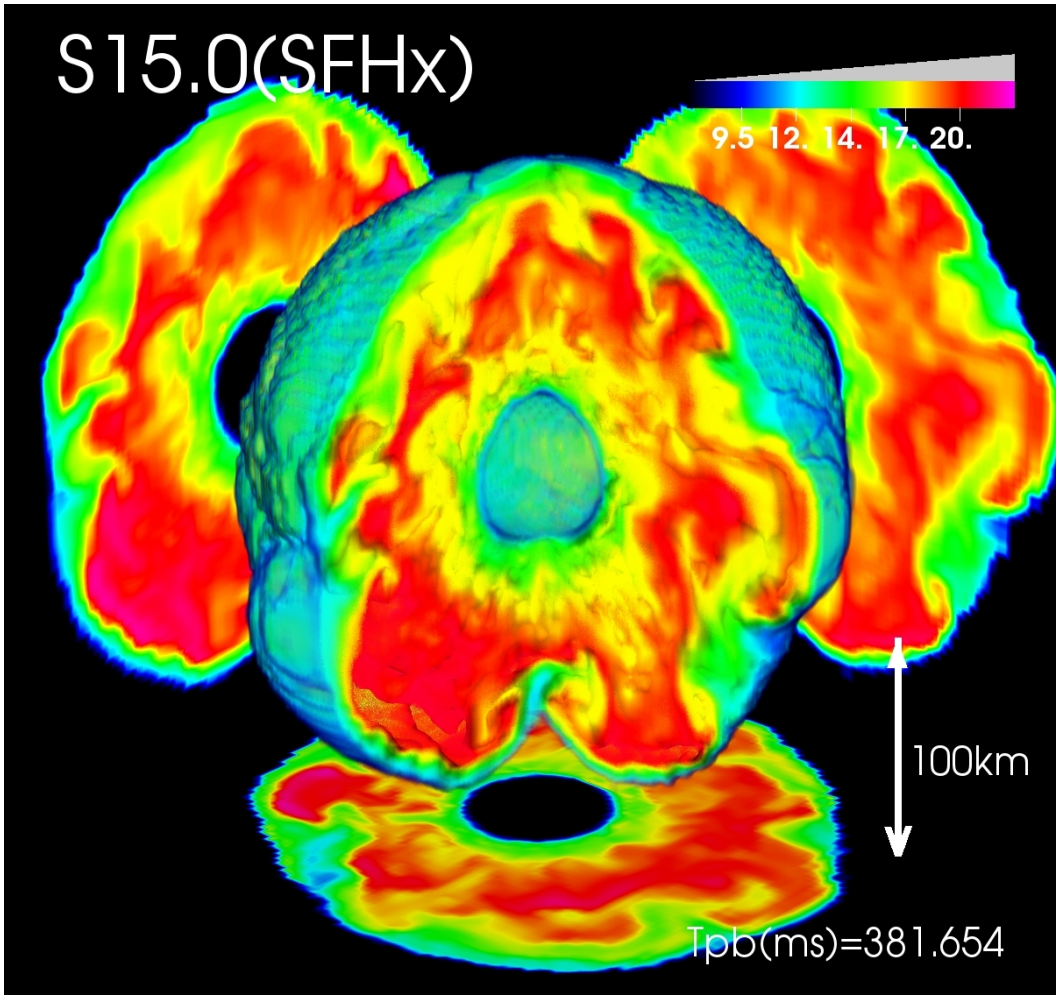

Fig. 1.11: Entropy 381.654 ms post bounce (tbp) in the centre of a simulated core collapse supernova of a $15 M_{\odot}$ star with full hydro and general relativity treatment. Colour represents entropy per baryon; right of, left of, and under the core cross sections through the respective plane are provided. In the very center of the exploding core the proto-neutron star is visible. Figure courtesy of Takami Kuroda, see Kuroda et al. (2012).

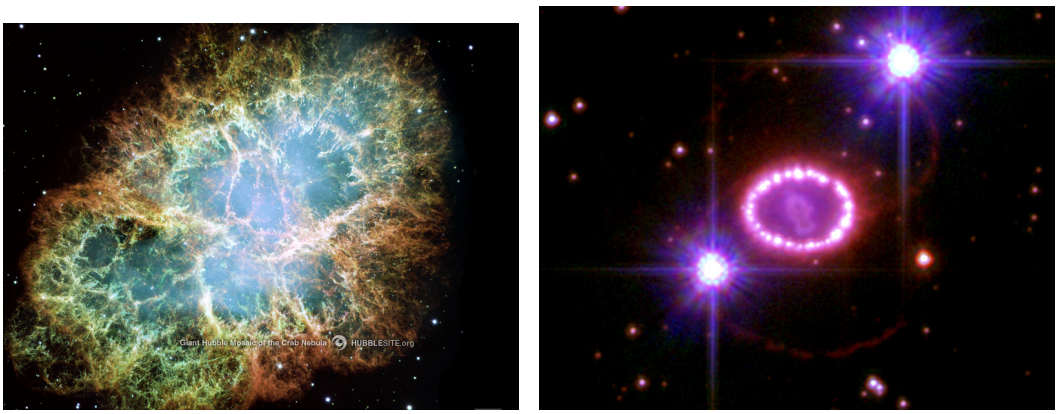

Fig. 1.12: Two examples of observed core collapse supernova remnants: Left panel: The Crab nebula. In the middle of this nebula, a pulsar (rotating neutron star) is detected. First reports on the explosion of the supernova date back to AD 1054 Image credits: NASA, ESA, J. Hester and A. Loll (Arizona State University). Right panel: Core collapse supernova SN1987A in the Large Magellanic Cloud. Image credits: NASA, ESA, P. Challis and R. Kirshner (Harvard-Smithsonian Center for Astrophysics)

1.6 Neutron star mergers

When a massive star is born in a double star system, both stars might undergo hydrostatic burning and core collapse supernovae individually. In a rare case, the two remaining neutron stars still orbit each other. Due to the emission of gravitational waves their orbit's radius decreases. When the two neutron stars come close enough they merge to form a larger neutron star or a black hole. This event is called a neutron star merger. Here, the prerequisites (neutron abundance, density and temperature) are reached to initiate the r-process (see section 1.2.6). A fraction of this (processed) matter is ejected into the interstellar medium, enriching it in r-process elements (cf. Freiburghaus et al. 1999, Panov et al. 2008, Korobkin et al. 2012, Bauswein et al. 2013, Rosswog 2013, Rosswog et al. 2014, Wanajo et al. 2014, Eichler et al. 2015).

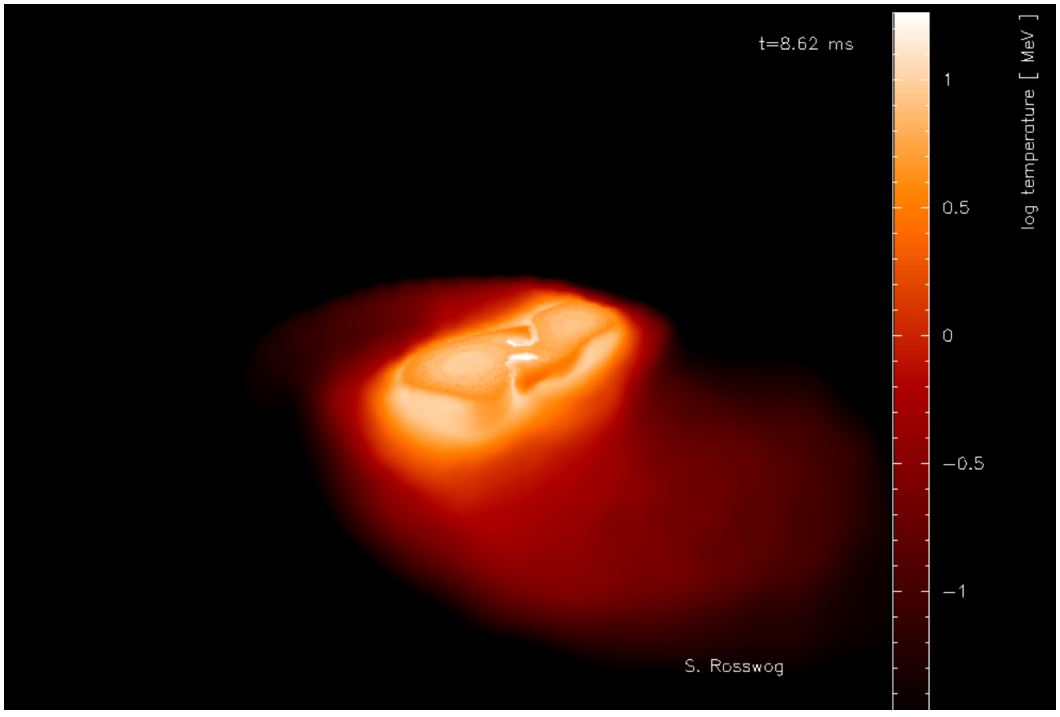

Fig. 1.13: Simulation of a dynamic neutron star collision with ejection of matter. Parameters are $m_1 = 1.3M_\odot$, $m_2 = 1.4M_\odot$, $(r_1 + r_2)/r_{peri} \equiv \beta = 1$. Illustration courtesy of Stephan Rosswog.

1.7 Low/intermediate mass stars and planetary nebulae

Despite the considerations made in section 1.4, low- ($0.08m_\odot \lessapprox m \lessapprox 0.8m_\odot$) and intermediate mass ($0.8m_\odot \lessapprox m \lessapprox 8m_\odot$) stars evolve different than massive ones. If a gas ball does not reach $m = 0.08$, it is unable to reach sufficient densities to ignite the hydrogen burning. Since it does not emit visible photons, it does not "shine", it is considered a "brown dwarf". Low mass stars ($0.08m_\odot \lessapprox m \lessapprox 0.8m_\odot$) are massive enough to (upon contraction) reach densities large enough to ignite the hydrogen burning. However, the mass is not sufficient to also ignite helium burning when the hydrogen fuel is exhausted. This type of star will just burn a large amount of hydrogen, until burning front has reached regimes where the densities are not sufficient for hydrogen burning anymore. The result is a remnant which consist only of hydrogen and helium and is called a "helium white dwarf". For intermediate mass stars ($0.8m_\odot \lessapprox m \lessapprox 8m_\odot$), the evolution is slightly different, since after the hydrogen burning phase, they are able to reach densities and temperatures triggering the helium burning. As a function of mass, the onset and evolution of the helium burning in these stars evolves slightly different:

- Stars in the mass range $0.8m_\odot \lessapprox m \lessapprox 2.3m_\odot$ will generate a degenerate helium core from the ashes of their hydrogen burning and thus experience a central helium flash instead of hydrostatic helium burning. Due to the degeneracy, it is not possible for this kind of star to regulate the helium burning hydrostatically.

- Stars in the mass range $2.3m_\odot \lessapprox m \lessapprox 8m_\odot$ ignite their helium burning in shells instead of in the core. Since the helium shells are thin and the triple alpha reaction is extremely sensitive to density (cf. eqs. 1.62 & 1.63), the (gravitationally) compressed shells violently produce helium shell flashes which move the outer layers of the star

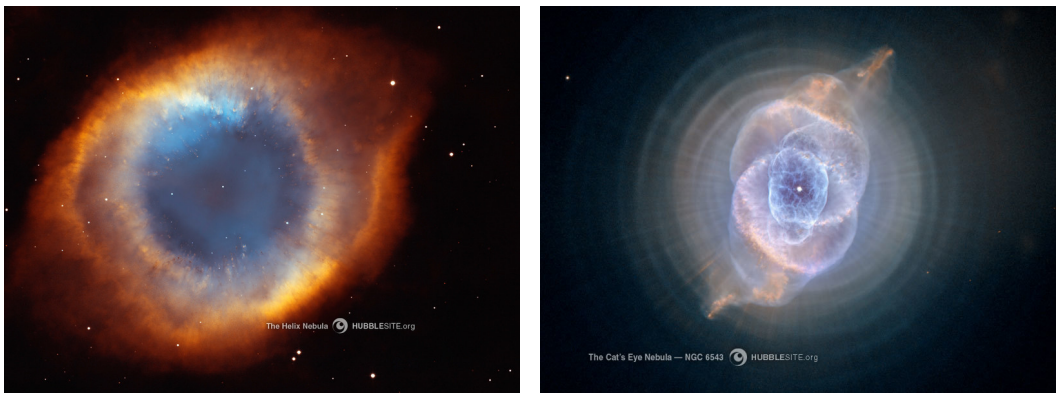

Fig. 1.14: Two examples of observed planetary nebulae: Left panel: The helix nebula. Image credits: NASA, NOAO, ESA, the Hubble Helix Nebula Team, M. Meixner (STScI), and T.A. Rector (NRAO). Right panel: The cat's eye nebula. Image credits: NASA, ESA, HEIC, and The Hubble Heritage Team (STScI/AURA)

further out, and then, due to the lower density, reduce the reaction rate dramatically until the outer layers move in again via gravitational attraction and thus quench the helium layer again. These repeated helium shell flashes with a shift of the outer star layers result in a stellar pulsation which leads to the onset of a strong stellar wind which blows the outer layers of the star apart. These outer layers form a ”planetary nebula” (two observed planetary nebulae can be found in figure 1.14), a giant gas cloud surrounding the stellar core which then has not enough mass and density to ignite further burning stages and thus extinguishes its nuclear burning. The resulting core is considered a ”white dwarf” which is still hot from the previous nuclear burning, but slowly cools down as it radiates its heat away.

1.8 Supernovae type Ia

Supernovae of type Ia are different from core collapse supernovae. Ia's originate in double star systems which consist of two intermediate mass stars. It has multiple channels:

- In the *single degenerate scenario (SD)* one of both stars evolves faster than the other and already evolved to a white dwarf. When they are so close that the slower evolving star crosses its Roche lobe[1], it will lose hydrogen gas from its outer layers which is then accreted around the white dwarf what might trigger hydrogen burning close to the dwarf. When a certain mass (near the Chandrasekhar mass) in the white dwarf is exceeded, the white dwarf will ignite explosive carbon burning and will be disrupted.

- In the *double degenerate scenario (DD)* both stars have undergone their respective burning stages and become white dwarfs. Similar to the SD scenario, one of these two stars might lose matter, here helium. Once the helium density on the surface of the other dwarf is sufficient to ignite helium burning of the accreted material, a shock front travels into the interior of the dwarf and triggers explosive carbon burning which disrupts the star.

- In the *core degenerate scenario* one of both stars evolves faster than the other and already evolved to a white dwarf. It dives into the companion red giant star's envelope and gets slowed down due to friction with gas. This deceleration further decreases the orbit and the white dwarf merges with the companion's core to form a fast rotating dwarf near the Chandrasekhar mass with a red giant envelope. When the rotation velocitiy of the dwarf decreases due to magnetic

[1]The Roche lobe is the area where the gravitational pull of one body is equal to the companion's attracting pull.

field effects, the centrifugal force which stabilizes the construct also decreases and cannot withstand a gravitational collapse anymore. Once the dwarf in the center reached the Chandrasekhar mass, it will be disrupted.

- In the *violent merger scenario*, two white dwarfs perform a heads-on collision. This event is rare and considered to happen in dense globular clusters.

The similarities between *regular* core collapse supernovae and supernovae of type Ia are a similar visible light curve, and a similar order of magnitude of the explosion's kinetic energy. The main difference is that the spectrum shows no silicon lines (nor hydrogen lines, but this is also true for some sub classes of core collapse supernovae). Also, it ejects large amounts of iron into the interstellar matter. Since all supernovae of type Ia require white dwarfs (which are produced from slowly burning intermediate mass stars, see section 1.7), core collapse supernovae occur much earlier (at lower metallicities) in the Galactic history. (For reference, on the Ia process and nucleosynthesis, see Iwamoto et al. 1999, Timmes et al. 2003, Thielemann et al. 2004, Travaglio et al. 2005, Bravo et al. 2010, Seitenzahl et al. 2013.)

Fig. 1.15: Picture of the observed type Ia supernova SN1994d in the NGC 4526 galaxy (bright spot in the lower left). Image credits:NASA, ESA, The Hubble Key Project Team, and The High-Z Supernova Search Team.

1.9 Supernova classification

Astronomers usually classify supernovae different than astrophysicists. This has historic reasons: Astronomers observed supernovae far earlier than astrophysicists could explain the different astrophysical scenarios responsible for them. This leads to different classifications. In astronomy, the following classifications are used:

- Supernovae type I: Early spectrum contains no hydrogen lines
  - Subclass Ia: spectrum contains silicon lines
  - Subclass Ib: spectrum contains no silicon lines but many helium lines
  - Subclass Ic: spectrum contains no silicon lines but few helium lines
- Supernovae type II: Early spectrum contains hydrogen lines
  - Subclass IIb: the helium line is dominant
  - Subclass IIL: the hydrogen lines are dominant and the lightcurve decreases linearly after the maximum
  - Subclass IIP: the hydrogen lines are dominant and the lightcurve remains on a high level for an extended amount of time

In astrophysics, the classification generally only consists of two types: thermonuclear supernovae of type Ia (identical with the astronomical class Ia; see section 1.8) on the one hand, and core collapse supernovae (containing the astronomical types Ib, Ic, IIb, IIL, and IIP; see section 1.5) on the other hand. For an illustration of the different classification schemes see table 1.3.

Astronomical classification					
SN I			SN II		
SN Ia	SN Ib	SN Ic	SN IIb	SN IIL	SN IIP
Thermonuclear SN	Core collapse SN				
Astrophysical classification					

Tab. 1.3: Illustration of the differences in astronomical and astrophysical supernova classifications.

1.10 The local interstellar medium

Beyond our Solar system's radiation bow shock begins the Local Fluff. It has a diameter of approximately 30 Ly, a average density of $0.26\ atoms * cm^{-3}$ and an average temperature of ≈ 6000 K. Among others, it contains the stellar systems α-Centauri, Formalhaut, Arktur, Altair, and Wega. The Local Fluff is a density anomaly in the Local Bubble, a (in the galactic plane nearly) spherical low density region. It consists (apart from the anomalies) of a hot and thin plasma with an average density of the order of $10^{-3}\ atoms * cm^{-3}$ and a temperature of the order of a million K and hydrogen gas with a density of $0.26\ atoms * cm^{-3}$. It is surrounded by a dense hydrogen gas shell. An illustration of this neighbourhood can be found in fig. 1.16. Once we go farther out, we find the Local Bubble surrounded by the Loop I, Loop II, and Loop III bubbles. We find the "bubble-like" structures over and over in our neighbourhood. These structures were created by central supernova explosions, blowing cavities into the interstellar medium and leave behind a "bubble" consisting of highly ionized, thin gas in the interior and a denser gas (with respect to the Galactic average) in the shell. In the case of the Local Bubble, it is thought that the supernova which blew the interstellar matter apart was a star which we know today as Geminga (pulsar). During its supernova explosion approximately one million years ago, it received a kick in the direction of the Gemini constellation so that today we do not find it on a central position anymore, but rather in the outer third of the Local Bubble. An alternative scenario of formation is the occurence of supernovae from the Pleiades (cf. Maíz-Apellániz 2001; Berghöfer & Breitschwerdt 2002). The bubble-style pattern observed in our neighbourhood can also be seen in our $3D$ chemical evolution simulations.

Fig. 1.16: Illustration of the Local Bubble. ”Lokale Flocke” translates to Local Fluff. ”Sonne” corresponds to Sun, and ”Lokale Blase” to Local Bubble. Image adopted from Henbest & Couper (1996). ©Cambridge University Press & Springer

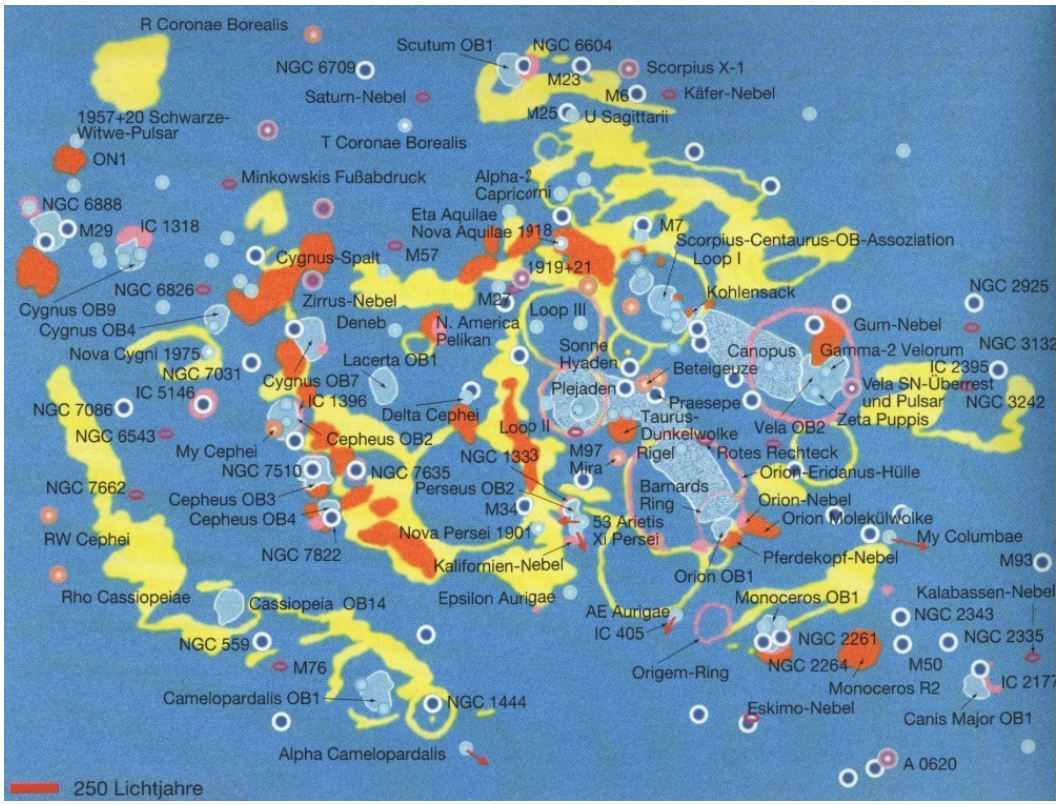

Fig. 1.17: Illustration of the surroundings of the Local Bubble. Image adopted from Henbest & Couper (1996). ©Cambridge University Press & Springer

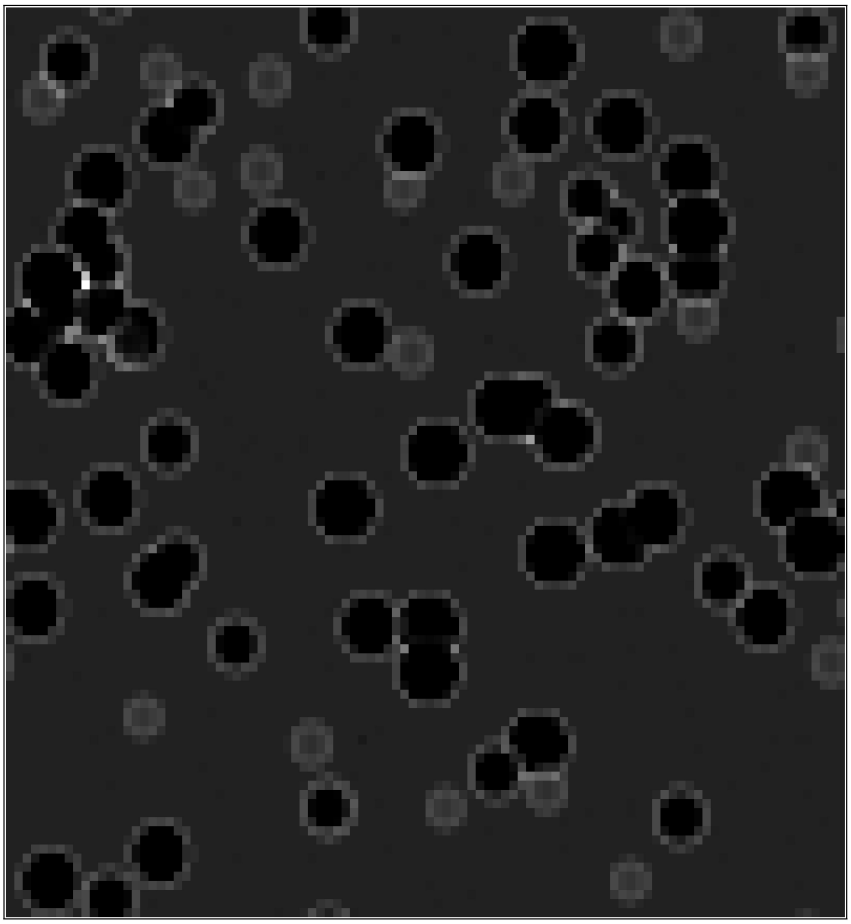

Fig. 1.18: Cut through the yz-plane of our simulation of the Galactic halo (for a description of our simulation see sections 1.13 and 2.3). The ”bubble-like” patterns are supernova remnants which resemble the bubble style patterns in our actual neighbourhood as in figs. 1.16 & 1.17.

1.11 The cosmic life cycle

Since most elements were not produced in the Big Bang or shortly later, they must have been produced somewhere else. The ”cosmic life cycle” explains how these elements have formed: The interstellar medium consists of gas. Under certain conditions, gas clouds collapse to stars which start hydrostatic burning. If the star is a low or intermediate mass star, it will not significantly produce elements, but lock up the matter out of which it was formed, and will re-eject it to the interstellar medium at the end of its life time (see also section 1.7). In the case that the low or intermediate mass star has a companion, under certain conditions this double star system might perform a supernova of type Ia (see section 1.8). If the star is massive enough, it might go through all burning stages (see section 1.4), and finally end up in a core collapse supernova (see section 1.5), re-ejecting processed matter into the interstellar medium. This might leave behind a neutron star. If this neutron star is born in a double neutron star system, there is a low probability that the two neutron stars might merge, re-ejecting processed matter into the interstellar medium (see section 1.6). These processes happen over and over again, until today’s composition is reached. So, except from hydrogen and helium, nearly every atom has been produced in a star or a process of the cosmic life cycle. An illustration of the cycle can be found in figure 1.19.

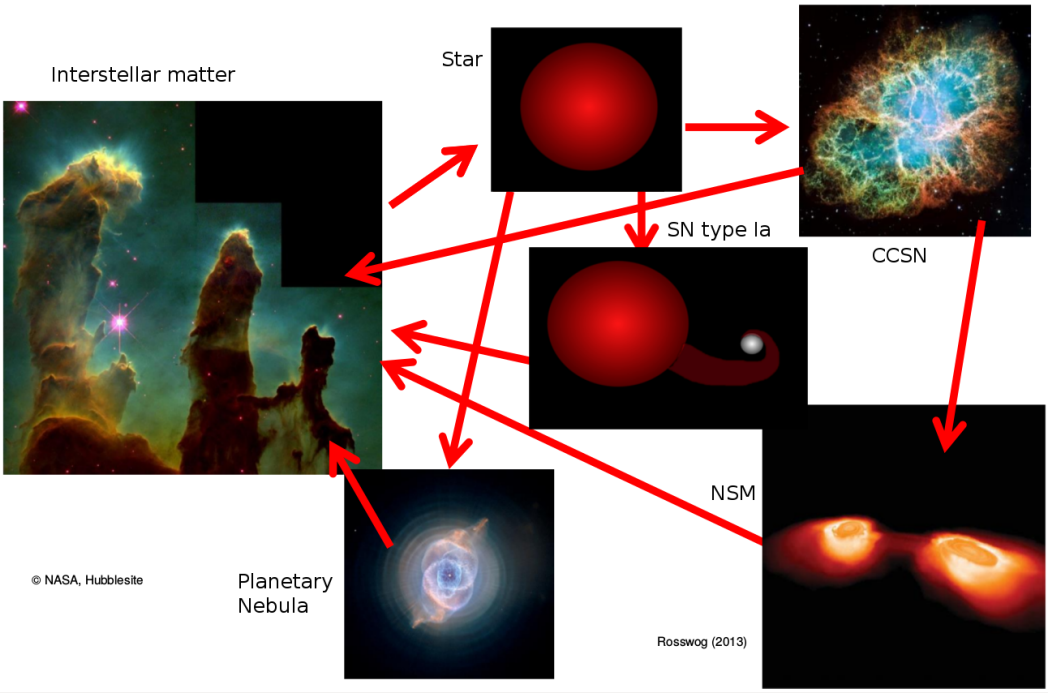

Fig. 1.19: Illustration of the cosmic life cycle. Dense regions of interstellar matter (ISM, left panel) form stars, which start hydrostatic burning (top center panel). Low mass stars (less than approximately eight solar masses) end their life in planetary nebulae (bottom left panel), re-ejecting their locked up material back into the ISM. If the low mass star has a companion star, it might perform a supernova of type Ia (center panel), re-ejecting iron-enriched matter back into the ISM. If a star is massive (more massive than ≈ 8 solar masses), it usually undergoes a core collapse supernova, also re-ejecting matter into the ISM. Usually, the remnant of such an explosion is a neutron star (or a black hole; this case is discussed later). If the neutron star has a neutron star companion, they might be gravitationally bound and (under the emission of gravitational waves) later perform a neutron star merger event, enriching the ISM with r-process elements. Image credits: NASA, ESA, HEIC, The Hubble Heritage Team (STScI/AURA), J. Hester, P. Scowen, and A. Loll (ArizonaState University), and Stephan Rosswog (Rosswog (2013))

1.12 Galactic abundances of alpha and r-process elements

In the context of galactic chemical evolution (GCE), abundances are usually measured in units of [X/Y] $= \log(N_X/N_Y) - \log(N_X/N_Y)_\odot$; Metallicity is usually written in terms of [Fe/H]. (In this notation, the sun has an abundance of $\log(N_X/N_Y) = \log(N_X/N_Y)_\odot$, hence [X/Y]$_\odot$=0=[Fe/H]$_\odot$ for the sun.)

1.12.1 alpha elements

Considering the GCE of α-elements[2], these elements are produced during the hydrostatic burning phase of massive stars (cf. section 1.4), and core collapse supernovae (cf. section 1.5). Their (astronomically) observed Galactic elemental abundances (see figure 1.20) can be explained in the following (simplistic) way (we take magnesium as example since some other α-elements show additional effects which go beyond the scope of this simplistic explanation). In supernovae, the α-elements are ejected together with iron. So, they are abundant from very low metallicities on. Supernovae of type Ia eject huge amounts of Fe (in relation to other α elements). However, they require two intermediate mass stars to evolve individually which takes longer than the evolution of massive stars. So, supernovae of type Ia only contribute later (at higher metallicities) to the chemical evolution of elements. They usually start to contribute at [Fe/H]$\gtrapprox -1.0$. Since they eject huge amounts of iron, the abundance curve for some elements increases when going from solar metallicities to [Fe/H]≈ -1.0. From here on, the abundance curve stays roughly constant, since the (α) elements are ejected together with iron under a constant ratio in average, e.g., [Mg/Fe]≈ 0.4 for magnesium. This ratio also sets the height of the (averaged) constant abundance curve

[2]Among the stable alpha elements are carbon, oxygen, neon, magnesium, silicon, sulfur, argon, and calcium.

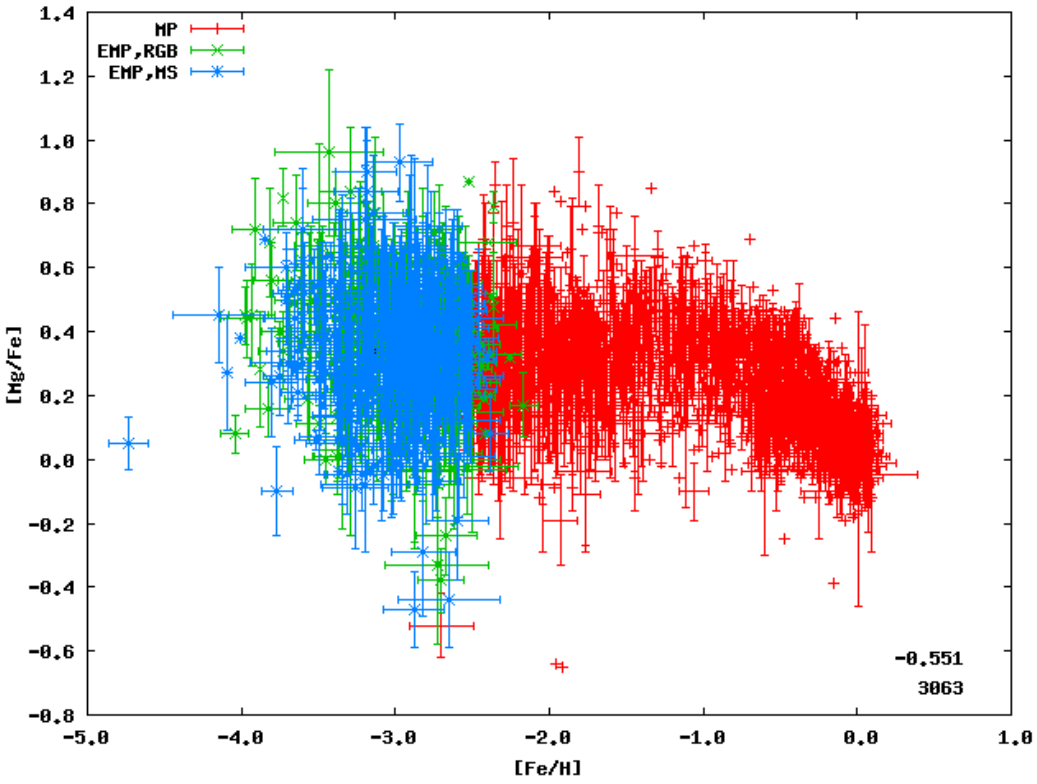

Fig. 1.20: Galactic abundances of magnesium vs. metallicity. Figure extracted from the SAGA (Stellar Abundances for Galactic Archaeology) database (e.g., Suda et al. 2008, Suda et al. 2011, Yamada et al. 2013), excluding CEMP and self enriched stars, and stars of binary nature.

for the metallicities [Fe/H]$\lessapprox -1.0$. However, different supernova progenitors (with different masses) eject different amounts of iron. This leads to a (small) scatter of α elements in [Fe/H]$\lessapprox -1.0$. For a simplistic illustration of the abundance curve for the magnesium example see figure 1.21.

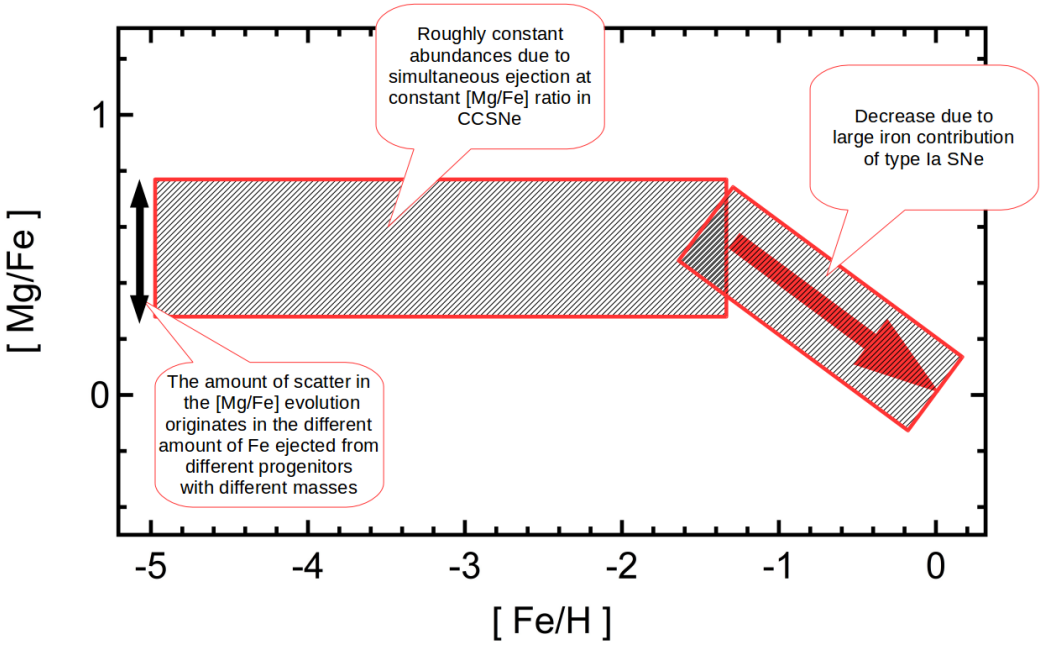

Fig. 1.21: Simplistic schematic of the evolution of the abundance curve of magnesium. At metallicities [Fe/H]$\lessapprox -1.0$, the (averaged) abundance are constant, with a scatter originating in different iron ejecta from different CCSN progenitor masses. At metallicities [Fe/H]$\gtrapprox -1.0$, SN Ia start to contribute and eject huge amounts of iron in respect to magnesium. This decreases the abundance curve in the range [Fe/H]$\gtrapprox -1.0$, until solar metallicites are reached.

1.12.2 r-process elements

Elements produced by the r-process (cf. section 1.2.6) show a large scatter, especially at low(est) metallicities. Together with unsuccessful r-process calculations in CCSNE, this excludes that r-process elements can be formed in standard supernovae (at least over the whole progenitor mass range). If r-process elements were formed in regular supernovae (over the whole progenitor mass range), they should show a similar abundance pattern as most of the other alpha elements (e.g., magnesium), i.e., no large scatter,

also at low metallicities. The large scatter shows that the r-process elements must have formed in a site which is rare compared to the standard supernova rate. (For illustration of the r-process elemental abundances see figure 1.22, for a comparison of magnesium and r-process abundances see figure 1.23)

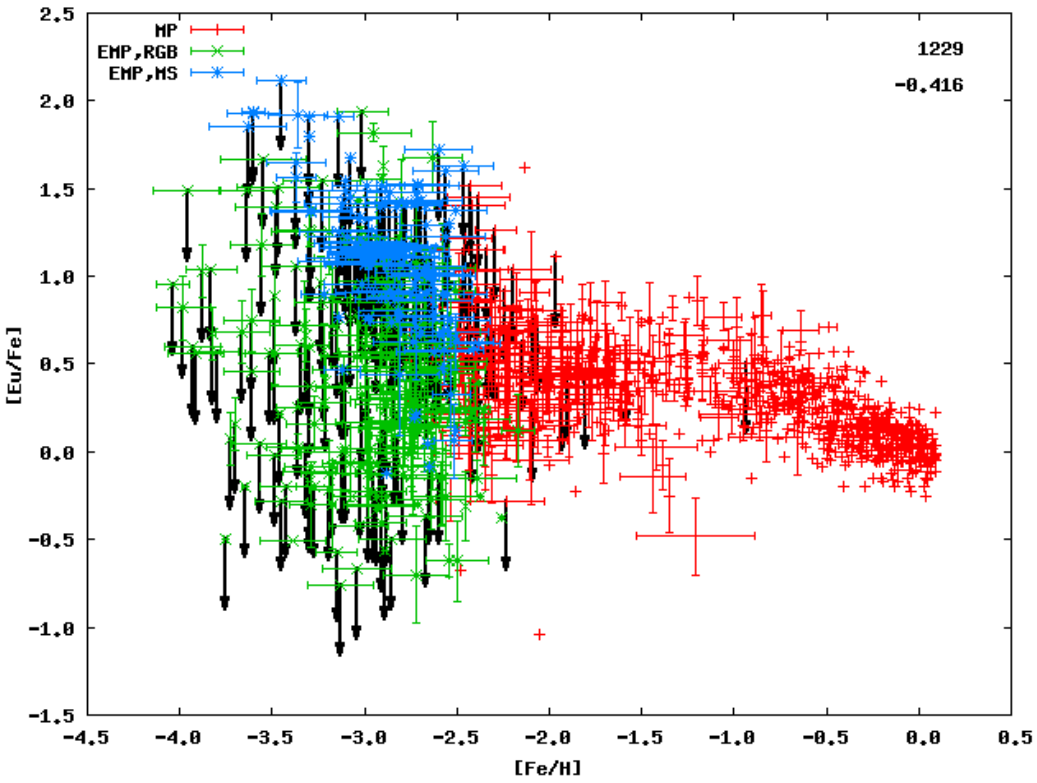

Fig. 1.22: Galactic abundances of europium vs. metallicity. Figure extracted from the SAGA (Stellar Abundances for Galactic Archaeology) database (e.g., Suda et al. 2008, Suda et al. 2011, Yamada et al. 2013; in particular mainly from Francois et al. 2007, Simmerer et al. 2004, Barklem et al. 2005, Ren et al. 2012, Roederer et al. 2010, Roederer et al. 2014a, Roederer et al. 2014b, Roederer et al. 2014c, Shetrone, Côté, Stetson 2001, Shetrone et al. 2003, Geisler et al. 2005, Cohen & Huang 2009, Letarte et al. 2010, Starkenburg et al. 2013, McWilliam et al. 2003), excluding CEMP and self enriched stars, and stars of binary nature.

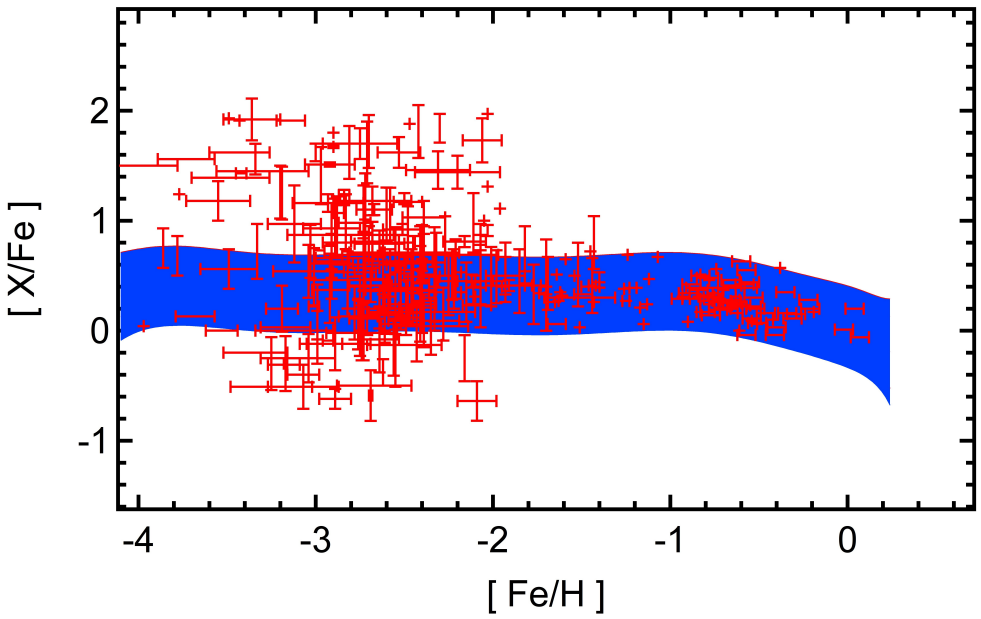

Fig. 1.23: Illustration of the different abundance scatter of magnesium and europium. The blue area marks the 95% statistics of magnesium observations, whereas red error bars show europium abundances. Figure adopted from Thielemann et al. (2016).

1.13 Our chemical evolution model

Our model is based on the model of Argast et al. (2004), but with a few modifications and improvements. The modelling details can be found in section 2.3, but the main properties and additional implications are summarized here. We set up a cube of (2 kpc)^3, representing a part of the Galaxy, and cut it into sub-cubes of (50pc)^3 each. In every time step of 1 My, the following happens:

- (Primordial) gas falls into the volume obeying the form $\dot{M}(t) = a \cdot t^b \cdot e^{-t/\tau}$.

- The total gas mass is calculated and the star formation rate is calculated using a Schmidt law with a power of $\alpha = 1.5$ (see Schmidt 1959, Kennicutt 1998, Larson 1991). The stars are then distributed into the cells (the amount of stars in the respective cells is scaled to the

respective cells density; The cell's minimum mass must exceed $50M_{\odot}$ to prevent biasing the initial mass function). The newly born stars' masses in the range $0.1M_{\odot} < m < 50M_{\odot}$ are randomly selected with a statistic weigh provided by a Salpeter initial mass function with a power of -2.35; Their life time expectation is then estimated using the Geneva stellar evolution and nucleosynthesis expectation routine, The star inherits the elemental abundances of the interstellar medium out of which it is formed.

- The overall star list is scanned to find stars which end their life in the present time step. If the star is a LMS/IMS, it returns the matter and composition out of which it is formed to the ISM via a planetary nebula. If the star is a HMS, the respective core collapse supernova yields of Thielemann et al. (1996) or Nomoto et al. (1997) are added to its elemental composition and then ejected polluting an amount of neighbouring cells which is determined under the assumption that the star explodes in a Sedov-Taylor blast wave with 10^{51} erg polluting an amount of $5 * 10^{4} M_{\odot}$ of ISM. In stars in the affected cells then inherit the ejected elements.

- One exception to the last procedure is the possibility for a HMS to explode in the sub-class of "magnetorotationally driven SN". However, this sub-channel is not relevant for this chapter and its nucleosynthesis and their implications will be discussed in chapters 2 & 3.

- There is a probability P_{NSM} that a newly born HMS is in a double star system which fulfils the requirements to later (after both HMS have undergone their respective evolution, went supernova individually, and performed an inspiral procedure for the duration of the coalescence time scale t_{coal}) undergo a NSM. One the NSM event is triggered, the surrounding ISM is polluted by r-process elements.

- Similar to the NSM procedure, there is a probability P_{Ia} that a newly born IMS is in a binary system fulfilling the requirements to undergo (after the respective stellar evolution of both stars) a supernova of type Ia. In this event, the site's respective yields (from Iwamoto et al. 1999, model CDD2) are added to the stars' initial composition and then ejected in a blast wave using the same procedure (but different nucleosynthesis yields) as for CCSNe.

A few implications and properties are discussed in the following sub-sections while the main implications can be found in the following chapters.

1.13.1 Gas fractions

The gas fraction describes which fraction of the mass in the volume is in the form of free gas, how much in fall into the volume happens per time step, how much interstellar medium is converted into stellar matter and how many solar masses of stellar matter are returned to the interstellar medium per time step in our simulations, see figure 1.24. In fall is modelled following the formula provided in the previous paragraph. It increases the total mass in the simulated volume. The gas mass is shaped by a dynamical process: Since star formation is coupled to the gas mass, it shows a monotonously increasing behaviour up to a simulation time of $\lessapprox 3.8$ Gy. After being formed, stars live for their specific life time (dependent mainly on mass and metallicity of the ISM out of which they were formed), and then re-eject (in some cases processed) matter into the ISM, thus re-increasing the gas mass. Since the life time of stars act as a "delay" between mass use and mass return, the mass return curve follows the mass use curve on average, but its shape is modulated due to the sampling of the life times over the specific stellar masses (hence the IMF). Since the infall decreases after a simulation time greater than $\gtrapprox 2.5$ Gy, and additionally long living low- and intermediate mass stars are formed, the gas mass decreases (after some delay of the order

of ≈ 0.5 Gy) after the decrease of the infall. This decrease also results in a decrease of the mass use, which leads to a decrease in the mass return and so forth. An illustration of the respective infall, gas mass, mass use and mass return amounts can be found in figure 1.24.

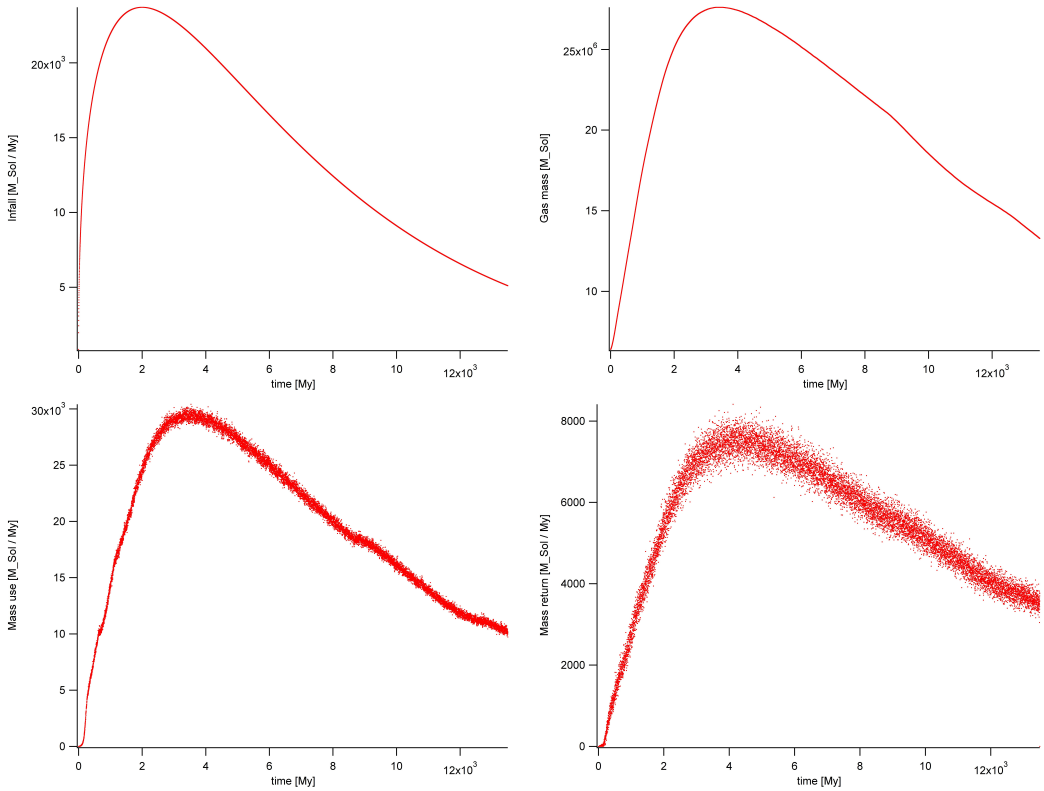

Fig. 1.24: Illustration of the gas masses in the simulation volume. Top left panel: in fall into the simulation volume. Top right panel: gas mass the volume. Bottom left panel: mass use in the volume, i.e., how much gas is converted to stars. Bottom right panel: mass return in the volume, i.e., how much stellar mass is returned to the insterstellar medium.

1.13.2 Age - metallicity relation

The age metallicity relation explains the connection between the Galactic age and the metallicity of the stars present. In the early Galactic stage, only few metals were present, hence the metallicity was low. Then stars enriched the interstellar medium with metals, thus increasing the interstellar mediums metallicity. The next generation of stars was already born in a metal enriched environment, so their metallicity was already increased. This process

repeats further and further, until the first SN Ia start to contribute at later Galactic development stages and significantly start to contribute iron, thus accelerating the process. Due to the logarithmic notation of the metallicity, the age-metallicity curve behaves approximatively in a logarithmic manner. An age-metallicity graph of our simulations can be found in figure 1.25.

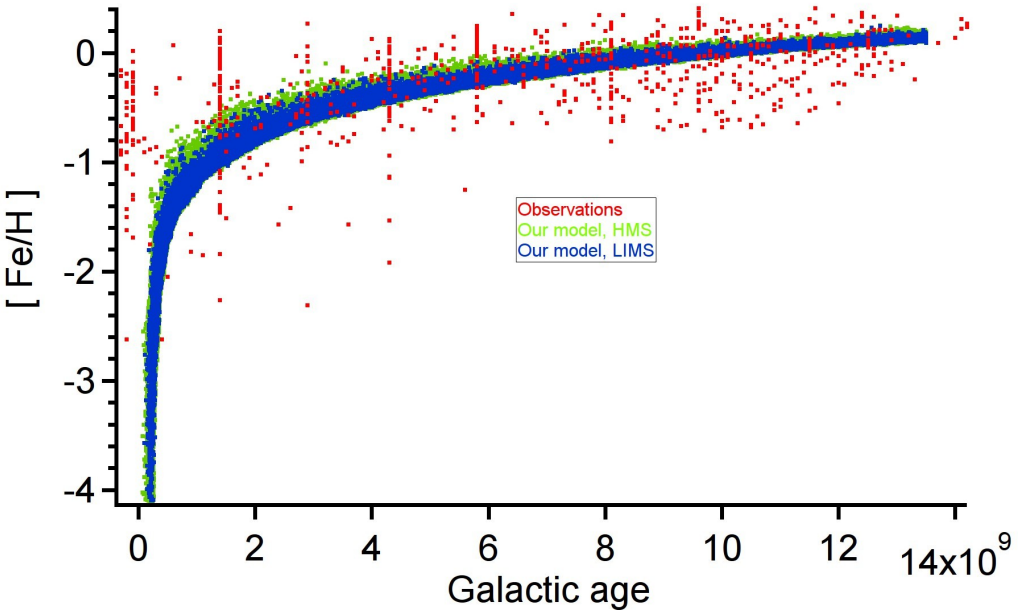

Fig. 1.25: Illustration of the age metallicity relation of our Galaxy. Red dots show observations as per Bensby et al. (2014); Green and blue dots shows the age metallicity relation of high mass stars, and low/intermediate mass stars as extracted from our chemical evolution model.

1.13.3 Supernova rates

The supernova rates are divided in two sub classes (see also the differences explained in section 1.9): core collapse supernovae and supernovae of type Ia. Since CCSNe are the end point of the evolution of a massive star, they are directly correlated to the occurrence of massive stars. The occurrence of CCSNe follows the mass use curve on average, with a delay which is due to the life time of the respective massive stars (which itself is modulated via the IMF). The same argumentation can be used to explain the occurrence of SNIa, however it has to be mentioned that only a small fraction of intermediate

mass stars will later undergo a SNIa event. Hence, the SNIa occurrence curve also follows the mass use curve on average with a longer delay than for the CCSNe curve due to the (slower burning and thus) longer life times of intermediate mass stars (sampled over the IMF of IMS), but the absolute value is reduced by the factor which determines the fraction of IMS actually undergoing this supernova channel. An illustration of the occurrence rates of the respective supernova channels can be found in figure 1.26.

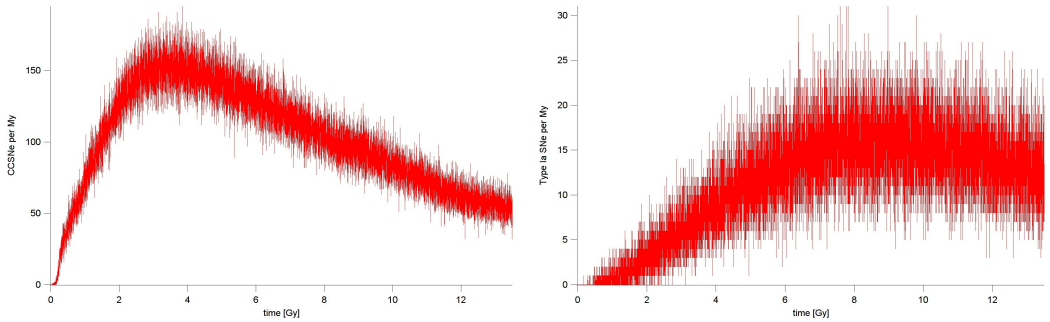

Fig. 1.26: Illustration of the SN rates in our simulation volume.

1.13.4 Neutron star merger rate

For the neutron star merger rate, a similar argumentation as in the previous section 1.13.3 can be used. Since NSM originate from massive stars, the NSM occurrence curve generally follows the CCSN curve. Due to the coalescence time scale, it is shifted towards higher simulation times. However, due to the low probability of the fulfilment of the prerequisites to actually perform a NSM event, and due to the *double* delay due to the life times of a massive star *and* the coalescence time scale, NSM events originating from different stellar generations overlap. In consequence, the NSM occurrence curve is strongly ”smeared out” in comparison to the mass use curve. Also, since NSMs are a very rare event, usually not more than one to two events happen per mega year so it is very difficult to find a pattern when considering the NSM occurrence curve. An illustration of the occurrence rates of neutron star mergers vs. Galactic life time can be found in figure 1.27

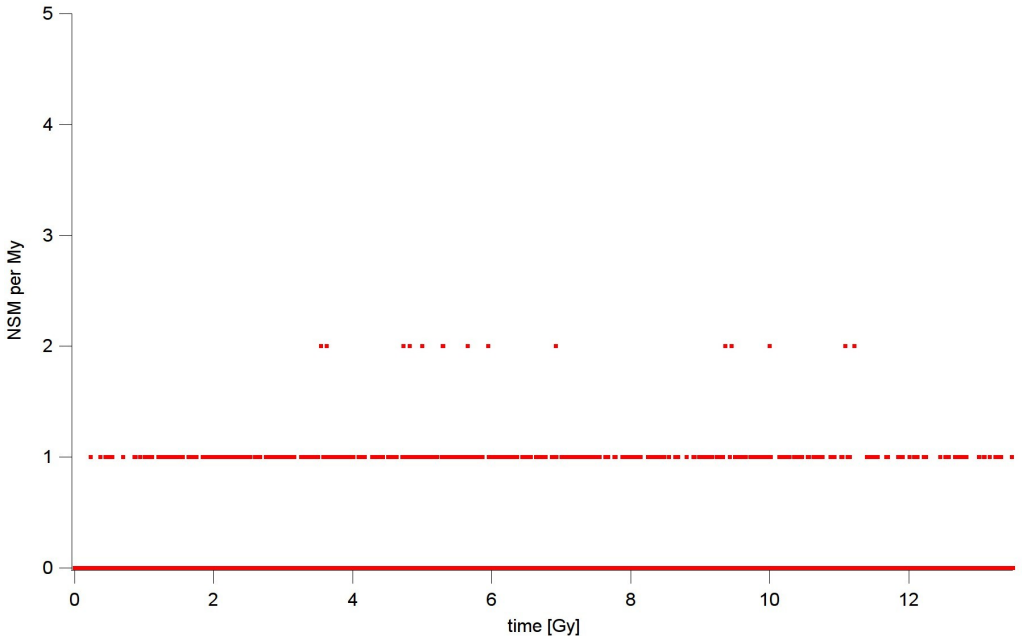

Fig. 1.27: Illustration of the NSM rate in our simulation volume.

1.13.5 Metallicity dispersion

The metallicity dispersion illustrates the metallicity of stars still alive at the end of the simulation. Due to the continuous metal production of (massive) stars, inhomogenieties in the interstellar medium and the presence of old (intermediate) mass stars, the (observed) curve resembles a Gaussian function with a strong arm towards lower metallicities, centered around Solar metallicity. An comparison between the observed and our modelled metallicity dispersion can be found in figure 1.28.

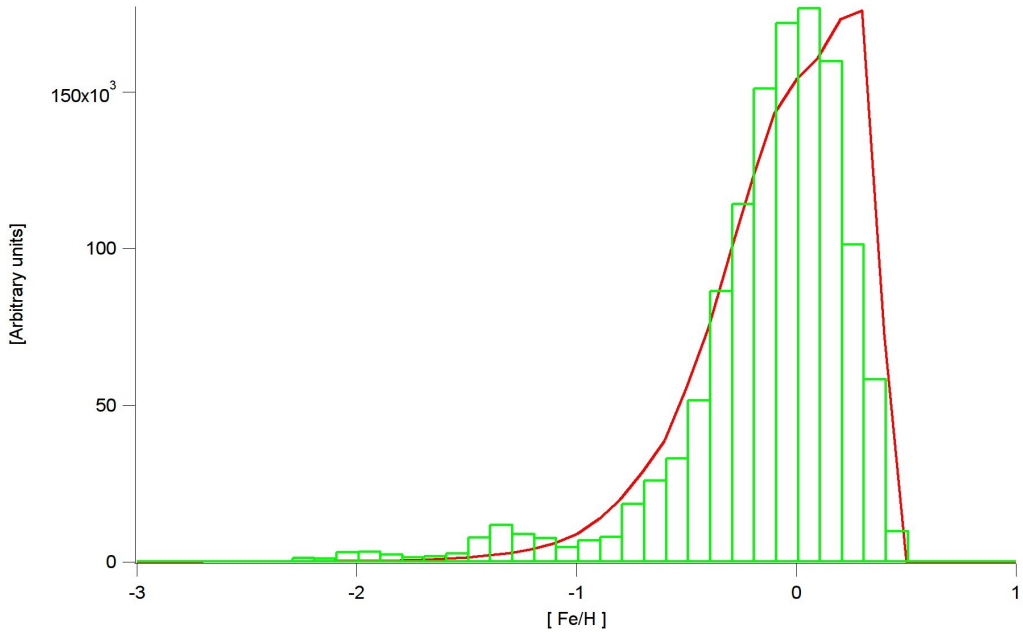

Fig. 1.28: Illustration of metallicity dispersion. The green histograms shows the dispersion observed stars in the Galaxy using the APOGEE R12 data, post-processed via the ASPCAP pipeline (Gárcia-Pérez et al. 2016); The red line shows the dispersion extracted from our chemical evolution model.

2 Galactic evolution of rapid neutron capture process abundances: the inhomogeneous approach

2.1 abstract

For the origin of heavy r-process elements, different sources have been proposed, e.g., core-collapse supernovae or neutron star mergers. Old metal-poor stars carry the signature of the astrophysical source(s). Among the elements dominantly made by the r-process, europium (Eu) is relatively easy to observe. In this work we simulate the evolution of europium in our galaxy with the inhomogeneous chemical evolution model 'ICE', and compare our results with spectroscopic observations. We test the most important parameters affecting the chemical evolution of Eu: (a) for neutron star mergers the coalescence time scale of the merger ($t_{\rm coal}$) and the probability to experience a neutron star merger event after two supernova explosions occurred and formed a double neutron star system ($P_{\rm NSM}$) and (b) for the sub-class of magneto-rotationally driven supernovae ("Jet-SNe"), their occurrence rate compared to standard supernovae ($P_{\rm Jet-SN}$). We find that the observed [Eu/Fe] pattern in the galaxy can be reproduced by a combination of neutron star mergers and magneto-rotationally driven supernovae as r-process sources. While neutron star mergers alone seem to set in at too high metallicities, Jet-SNe provide a cure for this deficiency at low metallicities. Furthermore, we confirm that local inhomogeneities can explain the observed large spread in the europium abundances at low metallicities. We also predict the evolution

of [O/Fe] to test whether the spread in α-elements for inhomogeneous models agrees with observations and whether this provides constraints on supernova explosion models and their nucleosynthesis.

2.2 Introduction

The rapid neutron capture process (r-process, e.g., Thielemann et al. 2011, and references therein) is responsible for the production of about half of the heavy element abundances beyond Fe in the solar system, and of the heaviest elements like Th and U. The remaining heavy element abundances are mostly made by the slow neutron capture process (s-process, e.g., Käppeler et al. 2011). Despite its relevance, the true astrophysical origin of the r-process is still under debate. Because of the larger uncertainties affecting the r-process nucleosynthesis predictions compared to the s-process in stars, the r-process isotopic contribution in the solar system has been originally identified by using the residual method, i.e., by subtracting the s-process component from the solar isotopic distribution (e.g., Arlandini et al. 1999, Bisterzo et al. 2014). The r-process residual abundances have been shown to be consistent in first approximation with the abundance signatures in old r-process rich metal-poor stars (at least for elements heavier than Ba, see Travaglio et al. 2004 for details), carrying the signature of the r-process nucleosynthesis in the early galaxy (e.g., Sneden, Cowan & Gallino 2008). For instance, Eu receives only a marginal contribution from the s-process (the s-process explains only 6 per cent of the solar Eu, while the remaining amount has an r-process origin, Bisterzo et al. 2014), and therefore it is often used as a tracer of the r-process nucleosynthesis in stellar spectroscopic observations. One possibility to test predictions from r-process nucleosynthesis is to include the r-process stellar yields in galactic chemical evolution (GCE) simulations, and to compare the theoretical results with spectroscopic observations at different metallicities. Eu is an ideal diagnostic for these studies. The purpose of this work is to illustrate the europium evolution throughout the evolu-

tion of our galaxy. We consider here the contribution from two sites (and their frequency) to the production of heavy r-process elements: Neutron Star Merger (NSM) and ”magneto-rotationally driven supernovae” (hereafter referred to as ”Jet-SNe”). We will show that the combination of both sites is able to reproduce the observed europium abundance distribution of the stars of our galaxy. Neutron star - black hole (NS-BH) mergers might have a non-negligible contribution to the r-process inventory in the galaxy. However, their relevance as astrophysical source for the r-process is controversial, since this event has not yet been observed (e.g., Bauswein et al. 2014). These difficulties also result in an extreme divergence of the predicted galactic rate of such an event (e.g., Postnov & Yungelson 2014). However, it should be noticed that a contribution from NS-BH mergers has been predicted as well (e.g., Korobkin et al. 2012, Mennekens & Vanbeveren 2014). We give an estimate of the possible effects caused by these events in Section 2.6. Chemical evolution of galaxies has made strong advances since its early days. Initially all approaches made use of the instantaneous recycling approximation in the sense, that the ejecta of stellar end stages were immediately utilized without delay after the initial star formation, assuming that the stellar evolution time scale is short in comparison to galactic evolution. If, in addition, the instantaneous mixing approximation was applied, i.e., assuming that the ejecta were instantaneously mixed throughout the galaxy, the whole galaxy acts as a homogeneous box. Neglecting this can explain radial gradients. Further developments included infall of primordial matter into and outflow of enriched material out of the galaxy (for a review of these early investigations see e.g., Audouze & Tinsley 1976). When relaxing the instantaneous recycling approximation, i.e., taking into account that (explosive) stellar ejecta enter the interstellar Medium (ISM) delayed with respect to the birth of a star by the duration of its stellar evolution, detailed predictions for the evolution of element abundances can be made. Based on nucleosynthesis predictions for stellar deaths, a number of detailed analyses have been performed, from light elements up to the Fe-group (e.g., Timmes et al. 1995, Goswami & Prantzos

2000, F. Matteucci, "The chemical evolution of the Galaxy" 2001, Gibson et al. 2003, Kobayashi et al. 2006, Pagel 2009, Kobayashi 2012, Matteucci 2012). Such approaches have recently also been applied to understand the enrichment of heavy elements in the galaxy (including r-process contributions) as a function of time or metallicity [Fe/H] (see e.g., Ishimaru & Wanajo 1999, Travaglio et al. 1999, De Donder & Vanbeveren 2003, Matteucci 2012, Vangioni et al. 2015). However, if still the instantaneous mixing approximation is applied, i.e., such ejecta are instantaneously mixed with the global ISM, no local inhomogeneities can be produced. The latter would relate to the fact that only limited amounts of the ISM are polluted by / mixed with the ejecta of each event. This effect is of essential importance, especially at low metallicities, where portions of the ISM are already polluted by stellar winds and supernovae, and others are not. In addition, different portions of the ISM are polluted by different types of events, leading to a scatter at the same metallicity, which can in fact be utilized as a constraint for these different stellar ejecta. When, however, utilizing the instantaneous mixing approximation, this leads to a unique relation between galactic evolution time and metallicity [Fe/H], i.e., any [Fe/H] can be related to a specific time in the evolution of a galaxy (while inhomogeneous mixing could experience similar [Fe/H] values in different locations of the galaxy at different times). This is especially the case in the very early galactic evolution ([Fe/H]< -2.5), when locally only a few stars (out of a whole initial mass function IMF) might have exploded and imprinted their stellar neighbourhood with their ejecta. Thus, the application of chemical evolution models which utilize the instantaneous mixing approximation is questionable for the early evolution of galaxies. In addition, for each [Fe/H], due to the instantaneous mixing, only a mean value of [X/Fe] (X being the element of interest to follow in chemical evolution) is obtained. Inhomogeneous mixing, however, could produce larger ratios in strongly polluted areas and smaller values in still less polluted ones. This means that the scatter in [X/Fe] at low metallicities, which might also be a helpful asset in pointing to the origin of element X,

cannot be reproduced or utilized with an homogeneous treatment. In case of rare events, which – on the other hand – produce large amounts of element X in each event, this would produce a large scatter, and – if observed – could be used as a very helpful constraint to identify the production site. For these reasons, specially for the origin of r-process elements like Eu, we think that only inhomogeneous chemical evolution models should be utilized at low metallicities. The two type of rare events (i) Jet-SNe (maybe up to 1% of all core collapse supernovae (CCSNe)) and (ii) neutron star mergers, with a similar occurrence frequency of about 1% of all CCSNe are considered here, while regular and more frequent core collapse supernovae might at most contribute to the lighter r-process elements. The binary merger rates are estimated by van den Heuvel & Lorimer (1996) as well as Kalogera et al. (2004). The rate of Jet-SNe is related to the fact that about 1% of neutron stars are found with magnetic fields of the order 10^{15} Gauss (magnetars, see, e.g., Kouveliotou et al. 1998, Kramer et al. 2009). Earlier inhomogeneous chem(odynam)ical evolution models for r-process elements like Eu have been provided by Travaglio et al. (2001, where the r-process yields were assumed to come from CCSN), Argast et al. (2004) and Matteucci et al. (2014) comparing neutron star mergers and core collapse supernovae, Cescutti & Chiappini (2014, comparing NSM and Jet-SNe) Mennekens & Vanbeveren (with NSM and NS-BH mergers), and Shen et al. and van de Voort et al. (2015, only utilizing neutron star mergers). One of the main questions here is related to the problem of reproducing [Eu/Fe] at low(est) metallicities. Cescutti & Chiappini (2014) have shown that this is possible with Jet-SNe. Argast et al. (2004) concluded that neutron star mergers cannot reproduce observations at [Fe/H]< -2.5, while van de Voort et al. (2015) and Shen et al. 2015 came to the opposite conclusion. The main difference between Jet-SNe and neutron star mergers is that in one case the immediate progenitors are massive stars and the first occurrence in chemical evolution is due to the death of massive stars. In the other case the progenitors are also massive stars, leading to two supernova explosions in a binary system, which – if not disrupted – causes

a binary neutron star system and a merger with a given delay time due to gravitational radiation losses. Thus, one needs to consider two aspects: (i) the two supernova explosions and the pollution of the ISM with their ejecta (for the case of NS-BH mergers see the discussion in section 2.6), and (ii) the delay time of the merger event after the formation of the binary neutron star system. Especially aspect (i) can only be treated adequately with inhomogeneous evolution models, and there an additional factor is of major importance: with how much matter the supernova ejecta mix before the neutron star mergers eject their products into the same environment. This paper is organized as follows. In section 2.3, we introduce the model used to compute the evolution of abundances. In section 2.4, we present the influence of the different r- and non-r-process sites on the evolution. Additionally, we provide an overview why an inhomogeneous treatment of the evolution is important. In section 2.5 we discuss the impact of inhomogeneities, causing and permitting a scatter of [X/Fe] ratios at low metallicities. As a further test of the model, we discuss the fact why the large scatter of [r/Fe] observed at low metallicities is strongly reduced for α-elements, and show how this constraints core collapse supernovae nucleosynthesis predictions, which are still not available in a self-consistent way. In section 2.6, our results are summarized and discussed.

2.3 The model

Recent chemodynamical galactic evolution models, like e.g., Minchev et al. (2014), van de Voort et al. (2015), and Shen et al. (2015), can model in a self-consistent way massive mergers of galactic subsystems (causing effects like infall in simpler models), energy feedback from stellar explosions (causing effects like outflows), radial migrations in disk galaxies, mixing and diffusion of matter/ISM, and the initiation of star formation dependent on local conditions, resulting from the effects discussed above. In our present investigation we still utilize a more classical approach with a parametrized infall of primordial matter, and a Schmidt law (Schmidt 1959) for star formation. Therefore, we neglect large scale mixing effects, while we include the feedback from stellar explosions and the resulting mixing with the surrounding ISM, according to a Sedov-Taylor blast wave. In this way, the model permits to keep track of the local inhomogeneities due to different CCSN ejecta. This approach allows to grasp the main features of the impact of the first stars / stellar deaths on the evolution of the heavy element enrichment. This approximation omits other mixing effects, e.g., spiral arm mixing (on time scales of the order of $2 \cdot 10^8$ years). The main focus of this work is the investigation of the chemical evolution behaviour at low metallicities, where these effects should not have occured, yet, and are therefore left out in this first order approximation. We treat the galactic chemical evolution of europium (Eu), iron (Fe) and α-elements (e.g., oxygen O), utilizing the established GCE code "Inhomogeneous Chemical Evolution" (ICE), created by Argast et al. (2004). A detailed description of the model can be found therein. For the simulation, we set up a cube of $(2kpc)^3$ within the galaxy which is cut in 40^3 smaller cubes representing a $(50pc)^3$ sub cube each. The evolution is followed with time-steps of 1My. Primordial matter is assumed to fall into the simulation volume, obeying the form

$$\dot{M}(t) = a \cdot t^b \cdot e^{-t/\tau}, \tag{2.1}$$

M_{tot}	Total infall mass	$10^8 M_\odot$
τ	time scale of infall decline	$5 \cdot 10^9$yrs
t_{max}	time of the highest infall rate	$2 \cdot 10^9$yrs
t_{final}	duration of the simulation	$13.6 \cdot 10^9$yrs

Tab. 2.1: Main infall parameters. See Argast et al. (2004) for details on the parameters.

which permits an initially rising and eventually exponentially declining infall rate. While τ and the total galaxy evolution time t_{final} are fixed initially, the parameters a and b can be determined alternatively from M_{tot} (the total infall mass integrated over time), defined by

$$M_{tot} := \int_0^{t_{final}} a \cdot t^b \cdot e^{-t/\tau}, \tag{2.2}$$

and the time of maximal infall t_{max}, given by

$$t_{max} := b \cdot \tau. \tag{2.3}$$

See Argast et al. (2004) for an extended discussion of the infall model and table 2.1 for the applied parameters.

2.3.1 Treating stellar births and deaths

The main calculation loop at each time step (1My) can be described in the following way.

1. We scan all mass cells of the total volume and calculate the star formation rate per volume and time step (10^6 yrs) according to a Schmidt law with a density power $\alpha = 1.5$ (see Schmidt 1959, Kennicutt 1998, Larson 1991). Dividing by the average stellar mass of a Salpeter IMF (power -2.35) provides the total number of stars per time step $n(t)$ created in the overall volume of our simulation.

2. Individual cells in which stars are formed are selected randomly until $n(t)$ is attained, but the probability is scaled with the density, which leads to the fact that patches of higher density, predominantly close to supernova remnants, are chosen.

3. The mass of a newly created star is chosen randomly in the range 0.1 to $50M_{\odot}$, subject to the condition that the mass distribution of all stars follows a Salpeter IMF. Consequently only cells which contain more than $50M_{\odot}$ are selected in order to prevent a bias.

4. The newly born star inherits the composition of the ISM out of which it is formed.

5. The age of each star is monitored, in order to determine the end of its lifetime, either to form a white dwarf or experience a supernova explosion (see 2.3.2 and 2.3.2). A fraction of all high mass stars ($M > 8M_{\odot}$), according to the probability (P_{Jet-SN}), is chosen to undergo a magneto-rotationally driven supernova event (see section 2.4.2). Type Ia supernova events are chosen from white dwarfs according to the discussion in 2.3.2. The treatment of neutron star mergers follows the description in 2.3.2.

6. The composition for the ejecta of all these events is chosen according to the discussion in 2.3.2. They will pollute the neighbouring ISM with their nucleosynthesis products and sweep up the material in a chemically well mixed shell. We assume that an event pollutes typically $5 \cdot 10^4 \mathrm{M}_{\odot}$ of surrounding ISM due to a Sedov-Taylor blast-wave of 10^{51}erg (Ryan, Norris & Beers 1996, Shigeyama & Tsujimoto 1998). This implies that the radius of a remnant depends strongly on the local density and the density of the surrounding cells.

7. In the affected surrounding cells, stars are polluted by the matter of the previously exploded star and the event specific element yields.

The details on the above procedure will be explained in the following.

2.3.2 Nucleosynthesis sites

Low (LMS) and intermediate mass stars (IMS)

Low and intermediate mass stars provide a fundamental contribution to the GCE of e.g., He, C, N, F, Na and heavy s-process elements during the asymptotic giant branch (AGB) phase. For instance, most of the C and N in the solar system were made by AGB stars (e.g., Kobayashi 2012). In their hydrostatic burning phase, these stars lock-up a part of the overall mass and return most of it to the ISM in their AGB phase by stellar winds. Since the maximum radius of these winds is orders of magnitude smaller than the output range of supernova events (e.g., radius of Crab remnant: 5.5 Ly (Hester 2008), while the diameter of the Cat's Eye Nebula is only 0.2 Ly (Reed et al. 1999)), our simulation assumes that stellar winds influence the ISM only in the local calculation cell. AGB stars provide only a marginal s-process contribution to typical r-process elements like Eu (e.g., Travaglio et al. 1999). In particular, for this work the s-process contribution to Eu plays a negligible role and we are not considering it here.

High mass stars (HMS)

Massive stars which exceed $8\mathrm{M}_{\odot}$ are considered to end their life in a core-collapse supernova (CCSN, e.g., Thielemann et al. 1996, Nomoto et al. 1997, Woosley et al. 2002, Nomoto et al. 2013, Jones et al. 2013). CCSNe produce most of the O and Mg in the chemical inventory of the galaxy. They provide an important contribution to other α-elements (S, Ca, Ti), to all intermediate-mass elements, the iron-group elements and to the s-process species up to the Sr neutron-magic peak (e.g., Rauscher et al. 2002). Associated to CCSNe, different neutrino-driven nucleosynthesis components

might be ejected and contribute to the GCE (e.g., Arcones & Thielemann 2013, and references therein), possibly including the r-process. We did not include regular CCSNe as a major source of heavy r-process elements, as recent investigations indicate strongly that the early hopes for a high entropy neutrino wind with the right properties (Woosley et al. 1994, Takahashi et al. 1994) did not survive advanced core collapse simulations (e.g., Liebendörfer et al. 2003) which led to proton-rich environments in the innermost ejecta (see also Fischer et al. 2010, Hüdepohl et al. 2010), causing rather a so-called νp-process (Fröhlich et al. 2006a, Fröhlich et al. 2006b, Pruet et al. 2005, Pruet et al. 2006, Wanajo 2006). Further investigations seem to underline this conclusion (recently revisited by Wanajo 2013), although a more advanced – in medium – treatment of neutrons and protons in high density matter causes possible changes of the electron fraction (Y_e) of ejecta (Martinez-Pinedo et al. 2012; Roberts et al. 2012) and might permit a weak r-process, including small fractions of Eu. Similar effects might be possible via neutrino oscillations (Wu et al. 2014). For this reason we did not include regular CCSNe in our GCE simulations, although a weak r-process with small (Honda et al. 2006-like) Eu contributions could be responsible for a lower bound of [Eu/Fe] observations (see Fig. 2.5), explaining a non-detection of the lowest predicted [Eu/Fe] ratios. Nucleosynthesis yields for HMS are taken from Thielemann et al. (1996) or Nomoto et al. (1997). Assuming a typical explosion energy of 10^{51}erg, the ejecta are mixed with the surrounding interstellar medium via the expansion of a Sedov-Taylor blast wave, which stops at a radius which contains about $5 \cdot 10^4 \mathrm{M}_\odot$ (see section 2.3.1 for details on the iteration procedure).

Supernovae Type Ia (SNIa)

When an IMS is newly born in a binary system, there is a probability that it has a companion in the appropriate mass range leading finally to a SNIa, following a double- or single degenerate scenario. We follow the analytical

suggestion of Greggio (2005) and reduce the numerous degeneracy parameters to one probability ($P_{SNIa} = 9 \cdot 10^{-4}$) for a newly born IMS to actually be born in a system fulfilling the prerequisites for a SNIa. Once the star enters its red giant phase, we let the system perform a SNIa-type explosion and emit the event specific yields (cf. Iwamoto et al. 1999, model CDD2), which highly enriches the surrounding ISM with iron. For this work we use the same SNIa yields for each metallicity, consistently with the Argast et al. (2004) calculations. We are aware that this choice is not optimal, since several SNIa yields including e.g., Mn and Fe depend on the metallicity of the SNIa progenitor (e.g., Timmes et al. 2003, Thielemann et al. 2004, Travaglio et al. 2005, Bravo et al. 2010, Seitenzahl et al. 2013). On the other hand, this approximation does not have any impact on our analysis and our conclusions.

Neutron Star Merger (NSM)

If two newly born HMS were created in a binary system, they may both undergo a CCSN individually. This could leave two gravitationally bound Neutron Stars ("NS") behind. Such a system emits gravitational waves and the two NS spiral inwards towards their common center of mass with a coalescence time (t_{coal}) until they merge. The actual merging event is accompanied by an ejection of matter and (r-process) nucleosynthesis (Rosswog 2013, Freiburghaus et al. 1999, Panov et al. 2008, Korobkin et al. 2012, Bauswein et al. 2013, Rosswog 2013, Rosswog et al. 2014, Eichler et al. 2015, Wanajo et al. 2014). As all of these publications show the emergence of a strong r-process, in the mass region of Eu they suffer partially from nuclear uncertainties related to fission fragment distributions (see e.g., Eichler et al. 2015, Goriely et al. 2013). For our purposes we chose to utilize as total amount of r-process ejecta $1.28 \cdot 10^{-2}\mathrm{M}_{\odot}$ (consistent with the $1.4\mathrm{M}_{\odot} + 1.4\mathrm{M}_{\odot}$ NS collision in Korobkin et al. 2012 and Rosswog 2013), but distributed in solar r-process proportions, which leads for Eu to a total amount of $10^{-4}\mathrm{M}_{\odot}$

per merger. This value is relatively high in comparison to other investigations in the literature. Observational constraints for the probability of a newly born star to undergo this procedure (P_{NSM}) are provided by e.g., Kalogera et al. (2004) who have found a NSM rate of $R_{NSM} = 83.0^{+209.1}_{-66.1}\text{Myr}^{-1}$, which corresponds to a $P_{NSM} = 0.0180^{+0.0453}_{-0.0143}$. The coalescence time, P_{NSM} and the event specific yields are important parameters for GCE, and their influence on the GCE are subject of this paper. Concerning the coalescence time scale, it might be more realistic to use a distribution function (e.g., as in Ishimaru, Wanajo & Prantzos 2015) instead of a fixed value. We utilize this simplified procedure as a first order approach.

Magnetorotationally driven supernovae (Jet-SNe)

A fraction (P_{Jet-SN}) of high mass stars end their life as a "magneto-rotationally driven supernova" or magnetar, forming in the center a highly magnetized neutron star (with fields of the order 10^{15}Gauss) and ejecting r-process matter along the poles of the rotation axis (Fujimoto et al. 2006, Fujimoto et al. 2008; Winteler et al. 2012, Mösta et al. 2014). r-process simulations for such events were first undertaken in 3D by Winteler et al. (2012). For the purpose of this work, we randomly choose newly born high mass stars to later form a Jet-SN. At the end of their life time, they explode similar to a CCSN, however with different ejecta. Based on Winteler et al. (2012), we assume an amount of $14 \cdot 10^{-5}\text{M}_{\odot}$ of europium ejected to the ISM by such an event. In this work, we study the influence of P_{Jet-SN} and the specific Jet-SN yields on the GCE.

2.3.3 Observed stellar abundances

Data for the observed stars to compare our simulation results with are taken from the SAGA (Stellar Abundances for Galactic Archaeology) database (e.g., Suda et al. 2008, Suda et al. 2011, Yamada et al. 2013; in particular [Eu/Fe]

abundance observations are mainly from e.g., Francois et al. 2007, Simmerer et al. 2004, Barklem et al. 2005, Ren et al. 2012, Roederer et al. 2010, Roederer et al. 2014a, Roederer et al. 2014b, Roederer et al. 2014c, Shetrone, Côté, Stetson 2001, Shetrone et al. 2003, Geisler et al. 2005, Cohen & Huang 2009, Letarte et al. 2010, Starkenburg et al. 2013, McWilliam et al. 2003). From the raw data, we excluded carbon enriched metal poor stars ("CEMPs") and stars with binary nature, since the surface abundances of such objects are expected to be affected by internal pollution from deeper layers or pollution from the binary companion.

2.4 RESULTS

For a general understanding of the effects of Jet-SNe and NSM on GCE, namely the parameters P_{NSM}, t_{coal} and P_{Jet-SN}, we performed a number of simulations described in detail below.

2.4.1 Coalescence time scale and NSM probability

As a prerequisite, we studied the influence of both coalescence time and the probability of a binary system to become a NSM. In Figure 2.1, we present the evolution of [Eu/Fe] abundances when only NSM contribute to the enrichment. The results can be summarized as follows.

1. Smaller coalescence time scale leads to an enrichment of europium at lower metallicities. Larger coalescence time scale shifts this to higher metallicities.

2. A higher NSM probability shifts towards a quantitatively higher enrichment combined with an appearence at lower metallicities.

These effects can be explained in the following way.

1. When binary neutron star systems take longer to coalesce, the time between the CCSN of both stars and the NSM event is longer. The longer this delay time, also further nucleosynthesis events occur in the galaxy during this period, enriching the ISM with metals. Thus, when the NSM event finally takes place, surrounding stars have developed a higher [Fe/H] abundance, shifting the system towards higher [Fe/H] abundances, respectively. This implies an overall europium production shift towards higher metallicities.

2. With more binary systems becoming NSM, the produced europium amount per time step is larger, since every event produces the same amount of r-process elements. This leads to a higher [Eu/Fe] abundance, compared to simulations with lower NSM probability. As the fraction of NSM systems is higher while the CCSN rate is constant, larger amounts of europium are produced, while the surrounding medium evolves regularly. This also leads to a higher abundance of europium at lower [Fe/H]. These effects shift the [Eu/Fe] curve to higher values for the same [Fe/H].

All these results are consistent with the earlier conclusions by Argast et al. (2004), stating that it is extremely difficult to reproduce the observed [Eu/Fe] ratios at metallicities [Fe/H]< -2.5 by NSM alone. A potential solution would be that the preceding supernovae which produced the two neutron stars of the merging system mix their ejecta with more extended amounts of the ISM. We utilized the results following a Sedov-Taylor blast wave of 10^{51}erg, which pollutes of the order $5 \cdot 10^4 M_\odot$ of ISM until the shock is stopped. van de Voort et al. (2015) assumed (in their standard case) the mixing with more than $10^6 M_\odot$ of ISM (Shen et al. 2015 utilized $2 \cdot 10^5 M_\odot$ in a similar approach). This produces an environment with a substantially lower [Fe/H] into which the NSM ejecta enter. Thus, it is not surprising that in such a case the Eu enrichment by NSM is setting in at lower metallicities. The higher resolution run shown in Fig. 4 of van de Voort et al. (2015) agrees with our results. Thus, the major question is whether such a very much enlarged mixing with the ISM by almost two orders of magnitude can be substantiated. We will discuss these aspect further in section 2.6

2.4.2 Probability of Jet-SNe

The contribution of Jet-SNe to the galactic Eu abundance differs from that of NSM. Since Jet-SNe explode directly from a massive star, they contribute

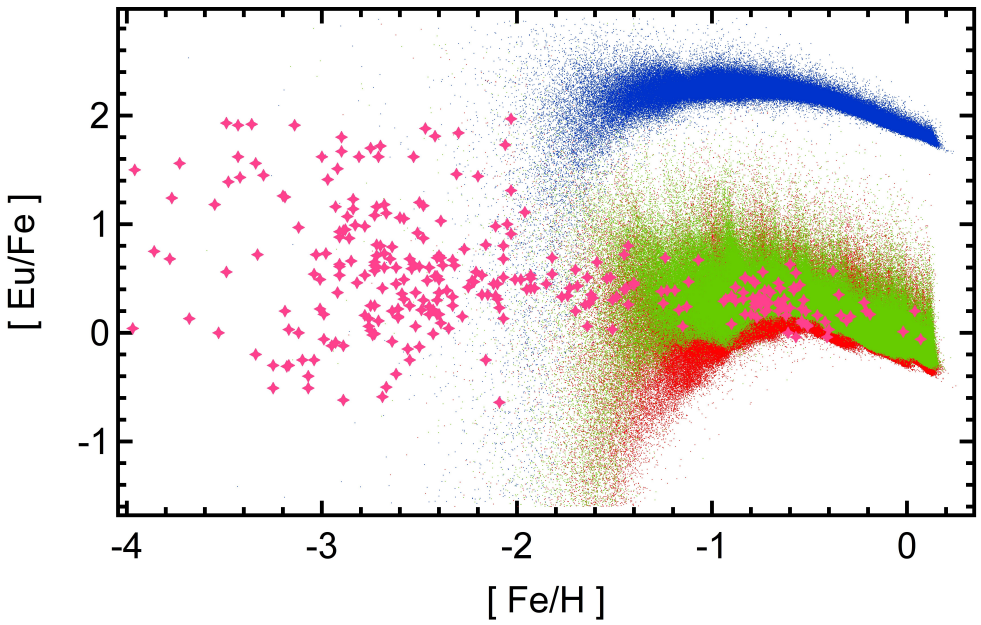

Fig. 2.1: Influence of coalescence time scale and NSM-probability on Eu-Abundances in GCE. Magenta stars represent observations. Red dots correspond to model star abundances as in Argast et al. (2004). The coalescence time scale of this event is 10^8 years and the probability P_{NSM} is set to $4{\cdot}10^{-4}$. Green dots illustrate the effect on the abundances if the coalescence time scale of NSM is shorter (around 10^6 years). Blue dots show the abundance change if the probability of HMS binaries to later merge in a NSM is increased to $4{\cdot}10^{-2}$ (cf. subsection 2.4.1).

much earlier to the chemical evolution than NSM. Since the interstellar matter is distributed more inhomogeneously than in later evolution stages of the galaxy, high [Eu/Fe] abundances are possible in individual stars. This leads to a large spread in the abundances towards lower metallicities. Considering Jet-SNe, the parameter with the highest impact on GCE for such rare events, similar to NSM events but ”earlier” in metallicity, is the probability of a massive star to actually become a Jet-SN. A lower probability leads to a smaller overall [Eu/Fe] abundance, while a higher probability leads to larger abundances. However, we also recognize a larger spread in abundances in models with lower probability. This comes from the fact that the high yield of the event only sets an upper limit on the abundances. The rarer an event is, the more and the longer stars remain unpolluted. This results in a larger spectrum of abundances in stars and therefore in a larger spread in [Eu/Fe] ratios. Note from Fig. 2.2 and Fig. 2.3 that Jet-SNe might explain the abundances at low metallicities better than NSM. Thus, while Jet-SNe alone could be an explanation for the lower metallicity observations, there is clear evidence of NSM events and therefore we have to examine the combination of both events. Whether the apparently to high concentration of model stars with low [Eu/Fe] values at metallicities $-3 <$[Fe/H]< 2 in comparison to observations is related to observational bias or whether we require another additional source will be discussed in the following sections.

2.4.3 Combination of sites

If both sites (Jet-SN and NSM) are considered to contribute to the galactic europium abundances, their contributions overlap. Therefore, parameters which lead to the observed [Eu/Fe] abundances, have to be searched for. As described in section 2.4.1, NSM contribute at a delayed stage to the GCE and in our simulations are unable to reproduce europium abundances at metallicities [Fe/H]< -2.5, Jet-SNe, however, contribute europium early, but only in those regions where they occured, and cause a larger spread in the

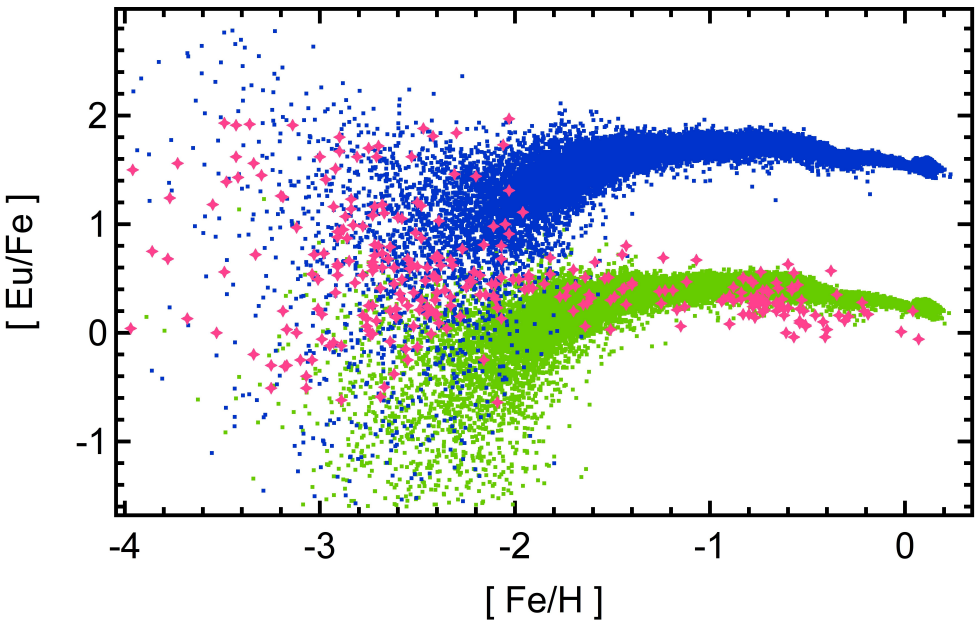

Fig. 2.2: Influence of increased Jet-SN probabilities on Eu-Abundances in GCE. Magenta stars represent observations. Green dots represent model star abundances based on Winteler et al. (2012), the Jet-SN probability has been chosen to follow the observations at [Fe/H]> -1.5. A good value seems to be 0.1% of HMS to end up in a Jet-SN. Note that this model fails to reproduce the observed abundances at lower metallicities. Blue dots illustrate the effect on the abundances if the Jet-SN probability is increased to 1%. This model better reproduces the observed abundances at lower metallicities, but clearly fails at higher ones.

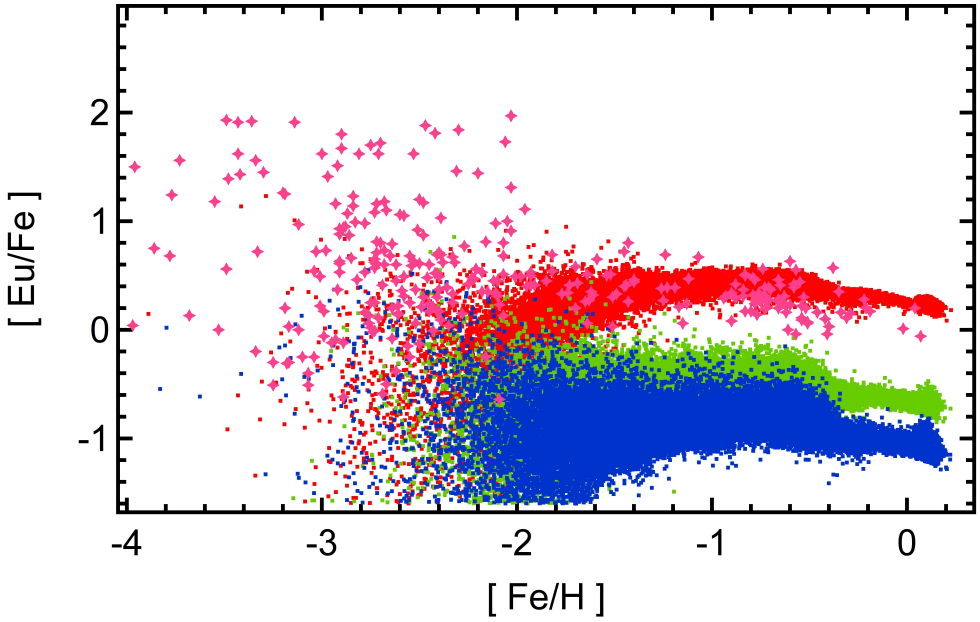

Fig. 2.3: Same as Figure 2.2, but with decreased probabilities. Red dots are the same as green dots in Fig. 2.2 with Jet-SN probability of 0.1%; Green and blue dots represent a Jet-SN probability of 10^{-4} and $2 \cdot 10^{-5}$, respectively. From the comparison of these models, we can see how decreased event probability shifts the abundance curve down. We also remark an increase of the spread in abundances when the probability is lowered. The rarer a high yield event is, the larger is the spread in abundances.

[Eu/Fe] values (cf. section 2.4.2). We have to test whether it is possible to use the same parameters as in sections 2.4.1 and 2.4.2, since the full combination of both events could lead to an overproduction of elements. We can use the earlier parameter explorations to tune the simulated abundance pattern in order to match the observations. In the following, we will discuss two possible cases:

1. $P_{NSM} = 3.4 \cdot 10^{-4}$, $P_{Jet-SN} = 0.3\%$, $t_{coal} = 1$My (hereafter model Jet+NSM:A). The results for the model Jet+NSM:A in comparison with observations are shown in Figure 2.4. This model provide a reasonable explanation of the observations at lower and higher metallicities, but there is an overproduction of europium between $-2 <$ [Fe/H] < -1. We conclude that larger coalescence time scales and larger probabilities are necessary regarding NSM, and lower probability of Jet-SNe is necessary to flatten and lower the modelled abundance curve.

2. $P_{NSM} = 3.8 \cdot 10^{-4}$, $P_{Jet-SN} = 0.1\%$, $t_{coal} = 10$My (Model Jet+NSM:B). The results for the model Jet+NSM:B in comparison with observations are shown in Figure 2.5. This model explains the main features of the abundance curve quite well: The spread at low metallicities, the first confinement of the spread at [Fe/H]≈ -2, the plateau between [Fe/H]≈ -2 and [Fe/H]≈ -0.6, and the second confinement of the spread at [Fe/H]≈ -0.2. However, there still seem to be difficulties at [Fe/H]≈ -2: the scatter in abundances towards low [Fe/H] ratios seems to be a bit too broad. This spread might be slightly reduced by additional mixing terms (e.g., spiral arms mixing) or an additional source providing ratios of [Eu/Fe]$= -1$, which we did not consider in this work.

Considering Fig. 2.4 and Fig. 2.5: While the results from both models Jet+NSM:A and Jet+NSM:B can reproduce the observed spread of [Eu/Fe] in the early galaxy, model Jet+NSB:B seems to better fit the overall [Eu/Fe]

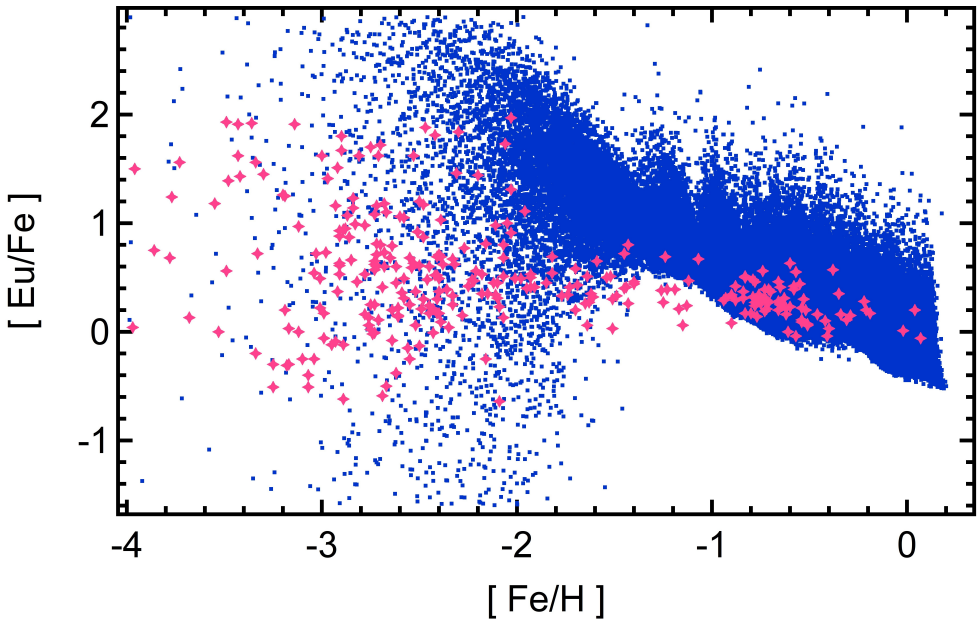

Fig. 2.4: Evolution of Eu-abundances in GCE including both Jet-SNe and NSM as r-process sites. Magenta stars represent observations, whereas blue dots represent model stars. Model (Jet+NSM:A) parameters are $P_{NSM} = 3.4 \cdot 10^{-4}$, $P_{Jet-SN} = 0.3\%$, $t_{coal} = 1$My.

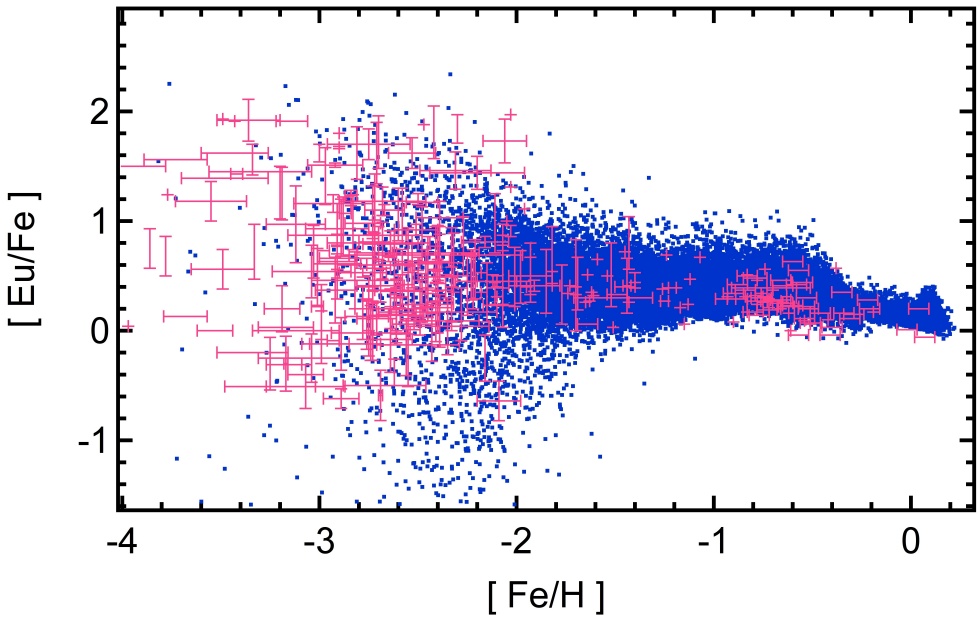

Fig. 2.5: Same as Figure 2.4, but with a different parameter set (ModelJet+NSM:B). Magenta stars represent observations (with observational errors; however, magenta stars at low metallicities which carry only horizontal errors represent upper limits). Blue dots represent model stars with $P_{NSM} = 3.8 \cdot 10^{-4}$, $P_{Jet-SN} = 0.1\%$, $t_{coal} = 10$My.

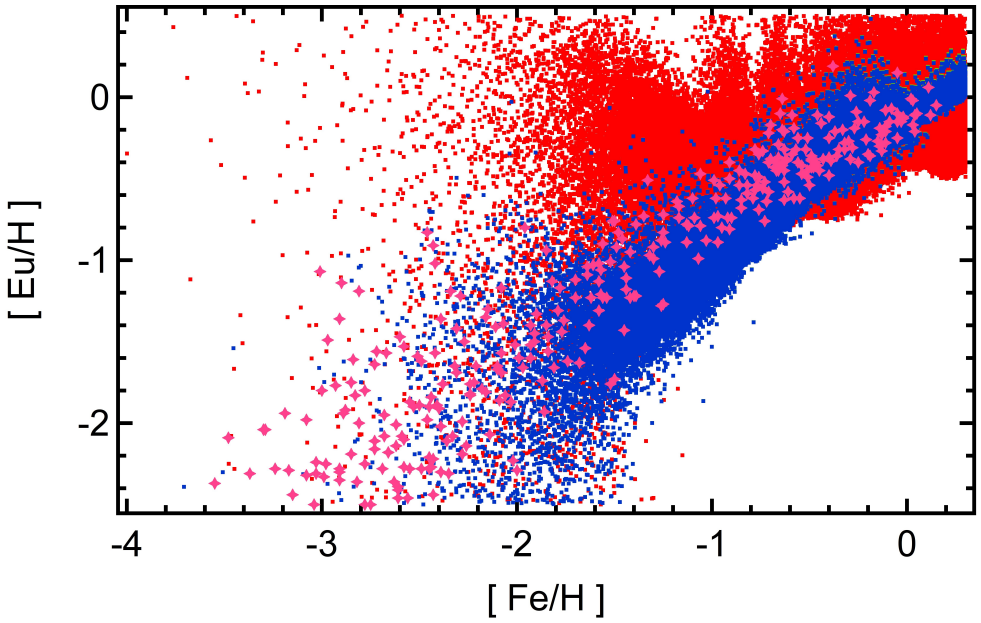

Fig. 2.6: Enrichment history for models Jet+NSM:A and Jet+NSM:B (cf. Figure 2.4 and 2.5 for evolution plots). Magenta stars represent observations, whereas blue dots represent model stars as per Figure 2.5 (Model Jet+NSM:B). Red dots representing the enrichment history of the simulation as per Figure 2.4 (Model Jet+NSM:A) do not suit the observational data.

vs. [Fe/H] distribution. On the other hand, the evolution of the [Eu/Fe] ratio at low metallicity depends on the r-process production and on the Fe production in CCSNe (see Section 2.5 and discussion), In Fig. 2.6, we compare the results for the *enrichment history* of europium in the galaxy according to Jet+NSM:A and Jet+NSM:B models with observations. While the [Eu/H] vs. [Fe/H] ratios predicted by model Jet+NSM:B are in agreement with the observations, model Jet+NSM:A seems to be ruled out.

2.5 The importance of inhomogeneities

2.5.1 Inhomogeneities in GCE

From observations of [Eu/Fe] in the early galaxy, one of the main features is a spread in the abundance ratios. Our model is able to reproduce these spreads, mainly because of the inhomogeneous pollution of matter. In Fig. 2.7, we try to illustrate the effect of applying such an inhomogeneous model. For this purpose, we perform a cut through the xy-plane of the simulation volume for specific time steps. These time steps are marked in the top panel of Fig. 2.7, in order to provide the reader with a quick glance of the extent of the inhomogeneous element distribution at the correspondent metallicities. For each marker, we provide the complete density field at this specific time step in the middle and lower panels (cf. figure caption for details). We show the extent of inhomogeneities in the middle left panel, for the first marker in the upper panel of the Figure. At this time step, we can see - by counting the ”bubble”-style patterns - that at least three supernovae must have taken place before the snapshot. Since such events give rise to nucleosynthesis, the abundances of metals in such a supernova remnant bubble are higher than outside such a remnant. A star being born *inside* such a remnant will inherit more metals than a star born *outside*. Therefore, in the early stages of galactic evolution the stellar abundances are strongly affected by the location *where* a star is born. Considering much later stages of the evolution, (e.g., the lower right panel of Fig. 2.7, corresponding to the fourth marker of the upper panel) the supernova remnants have a large overlap. Numerous supernova explosions, have contributed lots of nucleosynthesis all over the galaxy. This leads to an averaged distribution of abundances, including different events and an integral over the initial mass function of stars. Therefore, it resembles a ”mixed” phase of galactic evolution, where the elements have been homogenised over the whole volume. At this stage of the evolution, it seems not to be so relevant *where* a star was born. As

a consequence, there are smaller differences in the abundance of metals in stars. Therefore, a *confinement* in the spread of abundances of chemical elements at later stages of the chemical evolution is obtained. Becoming more and more homogeneous, the [Eu/Fe] value converges to a value that can be obtained by integrating the event yields over the whole IMF.

2.5.2 Instantaneous Mixing Approximation

A number of recent chemical evolution studies revoked the "instantaneous mixing approximation" (I.M.A., e.g., Chiappini et al. 2001, Recchi et al. 2001, Spitoni et al. 2009). The I.M.A. simplifies a chemical evolution model in terms of mass movement. In detail, all event outputs are expected to mix with the surrounding ISM instantaneously. Such approaches always result in an average value of element ratios for each [Fe/H]. Therefore, the I.M.A. scheme all stars at a given time inherit the same abundance patterns of elements and it is impossible to reproduce a scatter in the galactic abundances, which seems to be a crucial ingredient at low metallicities. Indeed, instead of a spread of distributions only one value is obtained for each metallicity. We calculate the best fit model (Jet+NSM:B, cf. Fig. 2.5) with I.M.A. The result can be found in Fig. 2.8. The I.M.A. approach may be used to study the chemical evolution trends with a lower computational effort, but Figure 2.7 shows that the reproduction of spreads in abundance ratios due to local inhomogeneities requires to use more complex codes as e.g., the ICE code adopted for this work. While inhomogeneus GCE codes can explain the spread in r-process elements, there is the question whether they might predict a far too large spread for other elements (e.g., α elements) at low metallicities (with present stellar yields from artificially induced CCSN explosion models). Such effects can also be seen in Fig. 1 in van de Voort et al. (2015) for [Mg/Fe], spreading by more than 1 dex, while observations seem to show a smaller spread up to 0.5 dex. This can be related to the amount of supernova ejecta being mixed with the ISM (see discussion above and in

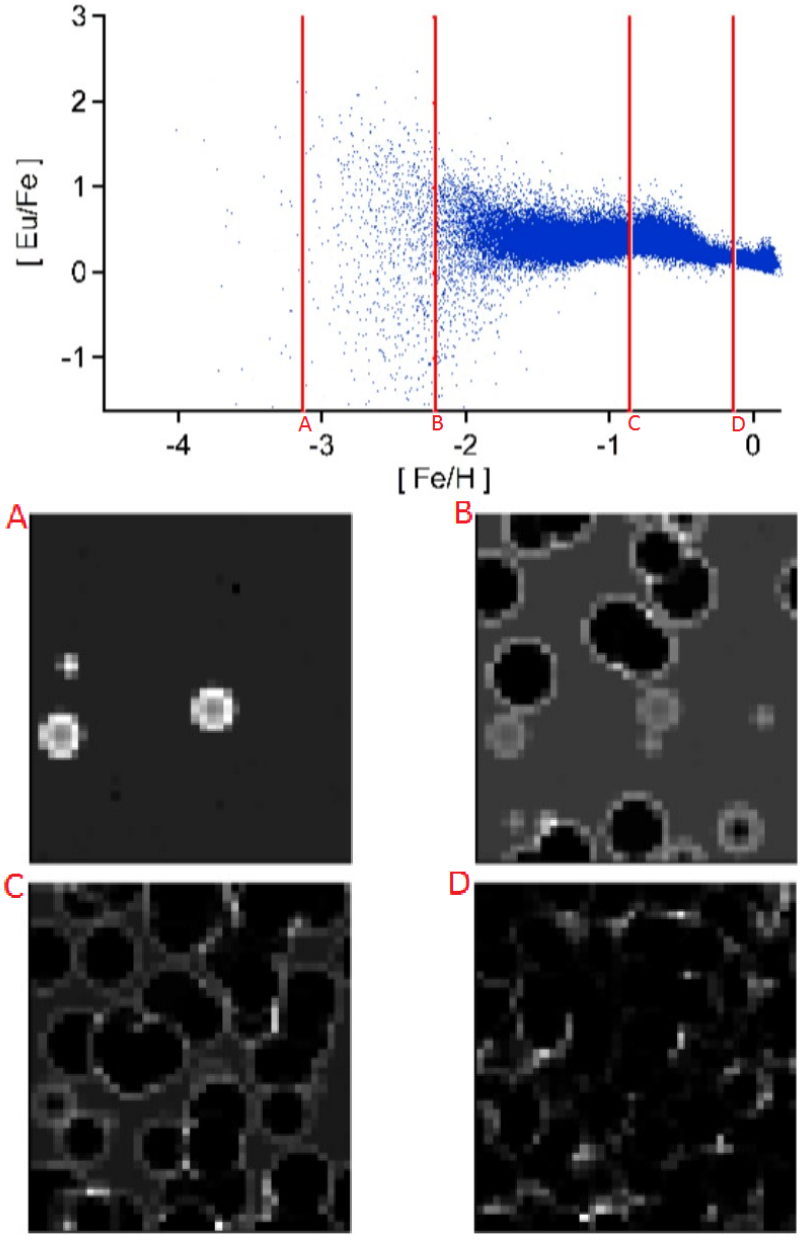

Fig. 2.7: The top panel shows the same GCE-model as in Fig. 2.5 (Model Jet+NSM:B), but without observations; The red markers refer to the position where a density determination cut through the the xy-plane of the simulation volume is performed. The middle and lower two panels show the density distribution through these planes. The middle left panel corresponds to the very left marker (”A”) position’s density profile (approximately 180 million years (My) have passed in the simulation), the middle right panel to the second marker ”B” ($\approx$ 290 My), the lower left panel to the third marker ”C” ($\approx$ 2 Gy) and the lower right panel to the very right marker ”D” ($\approx$ 12 Gy).

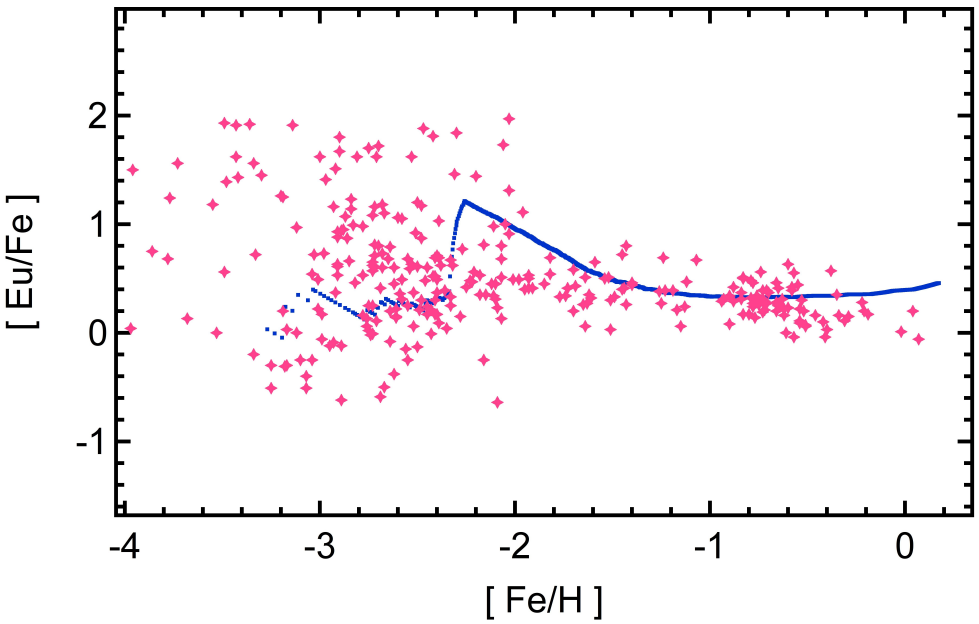

Fig. 2.8: Same GCE-model as in Fig. 2.5 (Model Jet+NSM:B); however I.M.A. is applied instead of inhomogeneous evolution. One is able to observe a trend in the abundance evolution, however the scatter in the abundance pattern is not present anymore (cf. Section 2.5 for further discussion). The kink at about [Fe/H]$= -2.5$ is related to the delayed time when NSMs set in and contribute to Eu as well. This Figure can also be compared to Fig. 2 in Matteucci et al. (2014) which shows the contribution of NSMs alone for various merger delay times and Eu production yields and Fig. 5 in Vangioni et al. (2015) [mergers alone being indicated by black lines]. Thus, also in this approach it is evident that the explanation of [Eu/Fe] at low(est) metallicities by NSM alone is not possible.

section 2.6: a more extended mixing reduces this spread), but it can also be related to the supernova nucleosynthesis yields which were never tested before in such inhomogeneous GCE studies. From general considerations of chemical evolution studies, it is found that there are large uncertainties for GCE studies, particularly the influence of stellar yields (e.g., Romano et al. (2010)). In Fig. 2.9, we show the results of model Jet+NSM:B, using the CCSN yields from from Nomoto et al. (1997) and Nomoto et al. (2006), which confirms a large spread in [O/Fe], similar to van de Voort et al. (2015) for [Mg/Fe]. However, present supernova yields are the result of artificially induced explosions with constant explosion energies of the order of 10^{51} erg. If we consider that explosion energies might increase with the compactness of the stellar core (i.e., progenitor mass, e.g., Perego et al. 2015), the heavier α-elements and Fe might be enhanced as a function of progenitor mass. On the other hand O, Ne, and Mg yields are dominated by hydrostatic burning and also increase with progenitor mass (e.g., Thielemann et al. 1996). This could permit to obtain more constant α/Fe ratios over a wide mass range, although the total amount of ejecta differs (increases) as a function of progenitor mass. This scenario does not take into account all the complexity and the multi-dimensional nature of the CCSN event (e.g., Hix et al. 2014, and references therein) that should be considered, but it may be interesting to test its impact in our GCE simulations. In Figs. 2.9 and 2.10, we show the results for tests where we:

1. replace the Nomoto et al. (1997) iron yields by *ad-hoc* yields, fitting, however, the observed SN1987A iron production;

2. keep the same CCSN rate as in the previous models;

3. adopt the parameters to study the r-process nucleosynthesis of Model Jet+NSM:B, obtaining the same [Eu/H] ratio.

This leads, based on the adopted CCSN yields, to a possibility to minimize the spread in α-elements at low metallicities, while keeping the spread in the

r-process element evolution. Therefore, the spread of [O/Fe] obtained from GCE simulations for the early galaxy is strongly affected by the uncertainties in the stellar yields, and it is difficult to disentangle them from more intrinsic GCE uncertainties. This means that at this stage it is not obvious whether an overestimation of the observed [O/Fe] spread is a problem of the ICE code, the observations could rather provide a constraint on stellar yields. In particular, the use of realistic, self-consistent, explosion energies, might reduce the spread at low metallicities to a large extent. Another fundamental point is related to the discussion in Section 2.4 concerning [Eu/Fe]. At this stage, we consider [Eu/H] as more constraining to study the r-process nucleosynthesis compared to [Eu/Fe], since Fe yields from CCSNe are affected by large uncertainties. Therefore, the model Jet+NSM:B is recommended compared to Jet+NSM:A (see also Fig. 2.6).

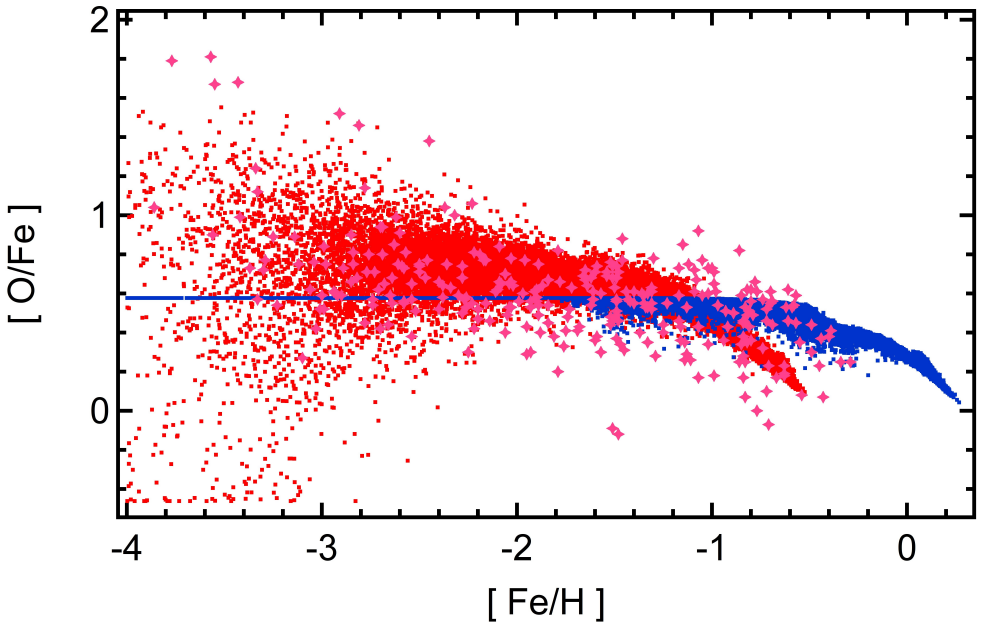

Fig. 2.9: Same GCE-model as in Fig. 2.5 (Model Jet+NSM:B); Red dots show the abundance evolution of Oxygen when Nomoto et al. (1997) yields are employed, while blue dots represent a far narrower spread at low metallicities if *ad hoc* yields are applied (which still would need to be optimized to obtain a better agreement with the metallicity evolution between $-1 < [\mathrm{Fe/H}] < 0$). Note that the downturn at high metallicities is shifted to higher [Fe/H] values. This is probably due to an overestimate of the total IMF-integrated Fe-production, which should be improved with realistic self-consistent explosion models and their iron yields. While the delay time scale for SNIa is unchanged, earlier CCSN produce more iron, thus dispersing the whole abundance curve. Here we only want to show how changes to possibly more realistic, progenitor-mass dependent, explosion energies can improve the [α/Fe] spread, while the [r/Fe] spread is conserved. (Cf. Section 2.5 for further discussion.)

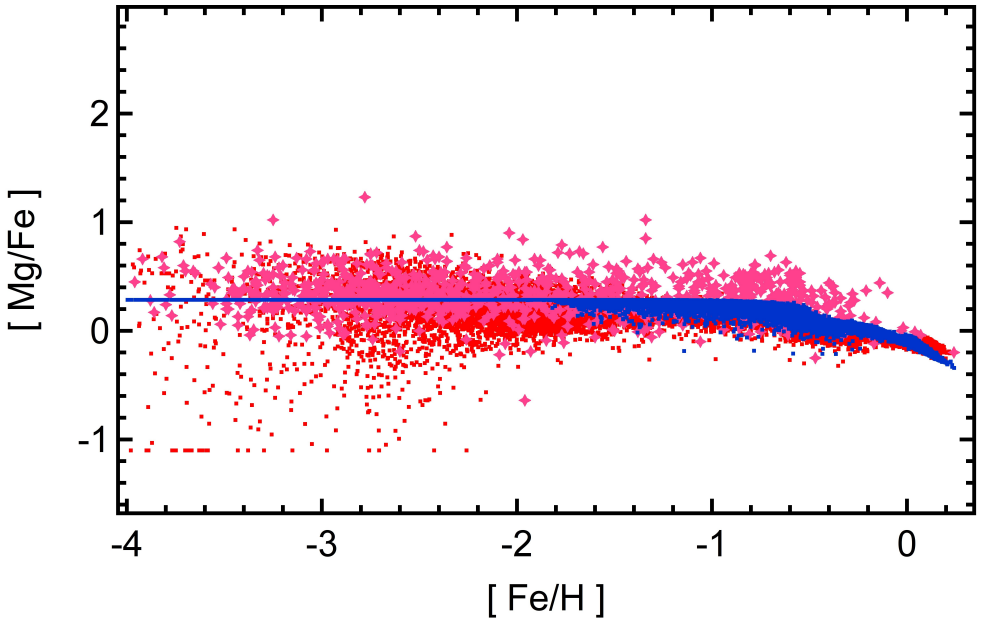

Fig. 2.10: Same consideration as in Fig. 2.9, however with magnesium instead of oxygen. GCE-model as in Fig. 2.5 (Model Jet+NSM:B); Red dots show the abundance evolution of magnesium when Thielemann et al. (1996) / Nomoto et al. (1997) yields are employed, while blue dots represent a far narrower spread at low metallicities if *ad hoc* yields are applied. Cf. Section 2.5 for further discussion.)

2.6 Conclusion and discussion

The main goal of this paper was to reproduce the solar europium abundance as well as the evolution of [Eu/Fe] vs. [Fe/H] throughout the evolution of the galaxy. For this reason we have studied the influence of two main r-process sites (NSM and Jet-SNe) on the GCE. Our simulations were based on the inhomogeneous chemical evolution (ICE) model of Argast et al. (2004), with updated nucleosynthesis input for the two sites considered, their respective occurrence frequencies / time delays, and a model resolution of $(50pc)^3$. The main conclusions are that:

1. The production of heavy r-process matter in NSM is evident since many years (see Freiburghaus et al. 1999 and many later investigations up to Korobkin et al. 2012, Rosswog 2013, Bauswein et al. 2013, Rosswog et al. 2014, Just et al. 2014, Wanajo et al. 2014, Eichler et

al. 2015, Mendoza et al. 2015). Our implementation of NSM in the inhomogeneous chemical evolution model "ICE" can explain the bulk of Eu (r-process) contributions in the galaxy for [Fe/H]> -2.5, but have problems to explain the amount and the spread of [Eu/Fe] at lower metallicities. This is in agreement with the initial findings of Argast et al. (2004). Recent SPH-based studies by van de Voort et al. (2015) make use of a mixing of the ejecta with $3 \cdot 10^6 M_\odot$, a further study by Shen et al. (2015) utilizes a mixing with $2 \cdot 10^5 M_\odot$ up to $8 \cdot 10^5 M_\odot$. The mixing volume we utilize, based on the Sedov-Taylor blast wave approach, would be related to a subgrid-resolution in these studies, but this treatment is essential for the outcome. Mixing initially with a larger amount of matter causes smaller [Fe/H] ratios into which the r-process material is injected. We have tested such differences in mixing volumes/masses also within our ICE approach. Fig. 2.11 shows the results we obtain when changing from the Sedov-Taylor blast wave approach to a mixing mass of $2 \cdot 10^5 M_\odot$ (like in Shen et al. 2015), and we can see that we essentially reproduce their results. On the other hand, a higher resolution test in section 3.1 of van de Voort et al. (2015) is essentially in agreement with our results presented above. Thus, these differences are not based on the differences in sophistication of the multi-D hydrodynamics approach, permitting to model energy feedback from supernovae, outflows and infall, they can rather be linked directly to the mixing volumes of supernova ejecta. This requires further studies in order to understand whether there exist physical processes (on the timescale of the delay between the supernova explosions and the merger event) which permit a mixing beyond the Sedov-Taylor blast wave approach.

2. The production of heavy r-process elements in a rare species of CCSNe with fast rotation rates and high magnetic fields, causing (fast) jet ejection of neutron-rich matter along the poles has first been postulated by Cameron (2001). This was followed up in rotationally symmetric 2D

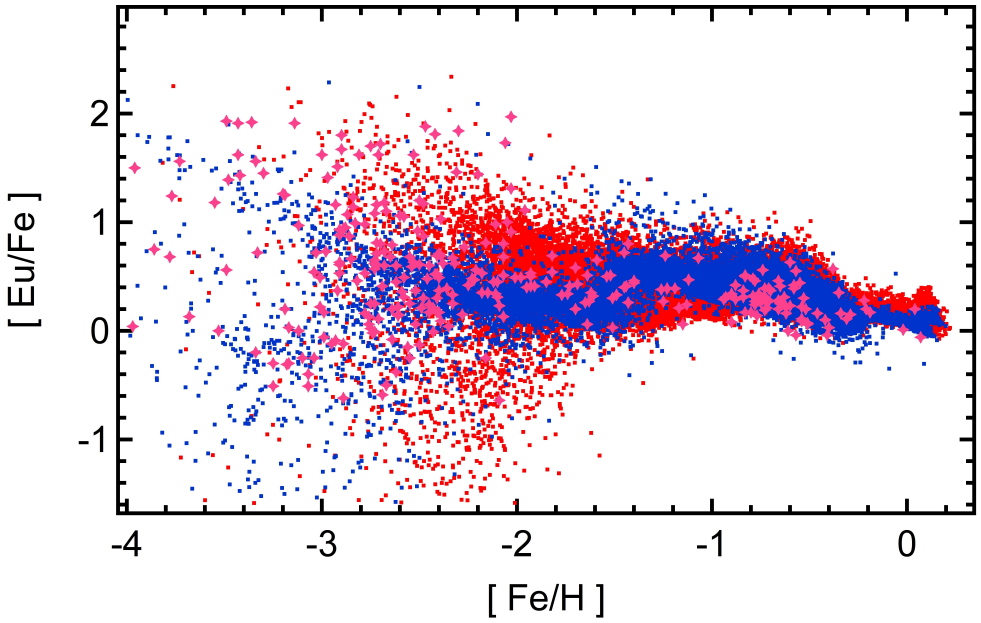

Fig. 2.11: Effect of slightly increased sweep-up mass on GCE. Magenta stars represent observations. Red dots show model stars as per our reference model JET+NSM:B. Blue dots represent a model where every CCSN pollutes $2 \cdot 10^5 M_\odot$ of ISM. The dominant effect of this increased sweep up mass is to decrease the scatter of abundances and to shift the abundance curve towards lower metallicities.)

calculations Fujimoto et al. (2006), Fujimoto et al. (2008) and the first 3D calculations by Winteler et al. (2012). These calculations still depend on unknown rotation velocities, and magnetic field configurations before collapse, however, they agree with the observations of magnetars and neutron stars with magnetic fields of the order 10^{15}Gauss which make up about 1% of all observed neutron stars. Further 3D calculations by Mösta et al. (2014) and recent 2D calculations by Nishimura et al. (2015), might indicate that not all events leading to such highly magnetized neutron stars are able to eject the heaviest r-process elements in solar proportions. Thus, probably less than 1% of all CCSNe end as Jet-SNe with a full r-process. When introducing Jet-SNe with ejecta as predicted by Winteler et al. (2012), they can fill in the missing Eu at lower metallicities and reproduce the spread in [Eu/Fe], in agreement with the recent findings of Cescutti & Chiappini (2014). We find that a fraction of 0.1% of all CCSNe which end up in this explosion channel

provides the best fit. This would mean that not all but only a fraction of magnetar events which produce the highest magnetic field neutron stars are able to eject a main r-process composition of the heaviest elements, as discussed above. Our conclusion is that both sites acting in combination provide the best scenario for understanding [Eu/Fe] observations throughout galactic history, with typical probabilities for NSM formations and (merging) delay times as well as probabilities for Jet-SNe. As a side effect we realized that present supernova nucleosynthesis yield predictions, based on induced explosions with a single explosion energy throughout the whole mass range of progenitor stars, bear a number of uncertainties. While apparently too large scatters of alpha/Fe ratios can be obtained in inhomogeneous chemical evolution models, when utilizing existing nucleosynthesis predictions from artificial explosions with energies of 1 Bethe, this might not be due to the chemical evolution model. Such deficiencies can be cured by assuming larger mixing masses with the ISM for supernovae explosions (van de Voort et al. 2015, Shen et al. 2015), or the introduction of an artificial floor of abundances based on IMF-Integrated yields of CCSNe for metallicities at [Fe/H]$= -4$, but it could in fact just be due the non-existence of self-consistent CCSN explosion models. We have shown that an explosion energy dependence on the compactness of the Fe-core, related to the main sequence mass, could solve this problem as well by modifying the nucleosynthesis results. Therefore, self-consistent core collapse calculations with explosion energies varying with progenitor mass and possibly other properties like rotation are highly needed. Although we have obtained a good accordance with the observed Eu abundances, the true origin of r-process elements might still require additional insights. The present investigation may be used to put constraints on the yields, as well as essential properties and occurrence frequencies of sites. There exist a number of open questions

not addressed in the present paper, related (a/b) to production sites and (c) to the true chemical evolution of the galaxy.

a) As discussed in detail in section 2.3.2, we did not include ”regular” CCSNe from massive stars as contributors to the main or strong r-process, producing the heaviest elements in the Universe. However, as already mentioned in section 2.3.2, there exists the chance for a weak r-process, producing even Eu in a Honda-style pattern in such events. This could provide the correct lower bound of [Eu/Fe] in Fig. 2.5 and would be consistent with the recent findings of Tsujimoto & Shigeyama (2014).

b) We did not include the effect of NS-BH mergers in the present paper. They would result in similar ejecta as NS-NS mergers per event (Korobkin et al. 2012), but their occurrance frequencies bear high uncertainties (Postnov & Yungelson 2014). Mennekens & Vanbeveren (2014) provide a detailed account of their possible contribution and also discuss their contribution to global r-process nucleosynthesis. One major difference with respect to our treatment of NSM in chemical evolution relates to the fact, that (if the black hole formation is not causing a hypernova event but rather occurring without nucleosynthesis ejecta) only one CCSN is polluting the ISM with Fe before the merger event, in comparison to two CCSNe. This would lead to a smaller [Fe/H] ratio in the ISM which experiences the r-process injection, and just to an ”earlier” appearance of high [Eu/Fe] ratios in galactic evolution. If we assume that BH formations are as frequent as supernova explosions, an upper limit of the effect would be that all NS-NS mergers are replaced by BH-NS mergers, moving the [Eu/Fe] features to lower metallicties by a factor of 2. However, the lower main sequence mass limit for BH formation is probably of the order $20 M_{\odot}$, and only a small fraction of core collapses end in black holes. Therefore, we do not

expect that the inclusion of NS-BH mergers shifts the entries by more than 0.15 in Fig. 2.1. This by itself would not be a solution in terms of making only compact (i.e. NS-NS and NS-BH) mergers responsible for the r-process at very low metallicities.

c) There have been suggestions that the Milky Way in its present form resulted from merging subsystems with a different distribution of masses. Such "dwarf galaxies" will experience different star formation rates. It is known that different star formation rates can shift the relation [X/Fe] as a function of [Fe/H]. If the merging of such subsystems will be completed at the time when type Ia supernovae start to be important, the relation [X/Fe]=f([Fe/H]) will be uniform at and beyond [Fe/H]> -1, but it can be blurred for low metallicities between the different systems, possibly leading also to a spread of the onset of high [Eu/Fe] ratios at low metallicities (Ishimaru, Wanajo & Prantzos 2015). The result depends on the treatment of outflows, should in principle be tested in inhomogeneous models, and also already be present in the simulations of van de Voort et al. (2015) and Shen et al. (2015). But it surely requires further investigations to test fully the impact of NSM on the r-process production in the early galaxy.

Future studies will probably require a distribution of delay times for NSM events, a test of the possible contributions by BH-NS mergers, a better understanding of yields, and improvements in understanding mixing processes after supernovae explosions and during galactic evolution. Testing the full set of element abundances from SNe Ia and CCSNe as well as the two sources discussed above, in combination with extended observational data, will provide further clues to understanding the evolution of galaxies.

3

Inhomogeneous chemical evolution of r-process elements in the Draco dwarf galaxy

3.1 Abstract

We examine the enrichment path of r-process elements in the Draco dwarf galaxy. This path has some unique features: An enrichment floor up to a certain metallicity, followed by an enrichment ”jump” providing a rapid increase while marginally increasing metallicity, which is then followed by a staircase-like enrichment pattern until the star formation comes to an end. We use our inhomogeneous chemical evolution model ”ICE”, to determine the possible site(s) contributing to the r-process enrichment: neutron star mergers (NSMs) and (the sub-class of) ”magnetorotationally driven supernovae” (MHD-SNe). In the neutron star merger case, we also estimate the effect of lowered star formation efficiencies on the r-process enrichment curve. Our main conclusions are

1. neutron star mergers have difficulties to explain the observed enrichment path for r-process elements when considered as exclusive r-process site, even when considering lowered star formation efficiencies.

2. MHD-SNe might explain the observed r-process element enrichment path when considered as exclusive r-process site.

3. A combined environment with both (long coalesence) NSMs and MHD-SNe explains the observed r-process enrichment path best.

3.2 Introduction

The origin of the heavie(st) elements beyond iron (Fe) is still under discussion. The rapid neutron capture process (r-process) is responsible for probably half the amount of these elements. Numerous astrophysical sites as origin of r-process elements have been discussed, e.g., processes in core collapse supernovae (CCSNe), and neutron star mergers (NSMs). Galactic chemical evolution (GCE) is a powerful tool which is able to help to constrain the astrophysical site(s) of the r-process. However, several GCE publications claim difficulties for scenarios where NSM act as exclusive r-process sites (e.g., Argast et al. 2004; Matteucci et al. 2014; Cescutti et al. 2015; Wehmeyer et al. 2015). The main argument is that the NSM elemental contribution is a delayed process after the occurrence of two independent CCSNe which produce two neutron stars, and that during the coalescence time scale of those two neutron stars, the interstellar medium's (ISM) metallicity already gets increased by surrounding SNe. Some studies claim that an additional site (e.g., high or low mass CCSNe, cf. Argast et al. 2004, and Matteucci et al. 2014 which is based on the two-infall model of Chiappini et al. 1997, 2001; or a sub-class of supernovae, cf. Cescutti et al. 2015; Wehmeyer et al. 2015), acting already at low metallicities, is necessary to explain the low metallicity and largely scattered abundances of r-process elements. Other works claim that the solution of this NSM problem is a scenario where independent smaller galactic systems (each with different mass and star formation efficiency) evolve individually and then later merge to form the Galactic halo (e.g., Ishimaru, Wanajo & Prantzos 2015). The choice of the combination of star formation efficiency and mass leads to an earlier or later (at lower or higher metallicities) onset of r-process enrichment, whereas the individual enrichment history path of the respective (sub-)system proceeds in a parallel manner. The main argument is that the observed Galactic elemental abundances can then be explained by the overlap of these parallel enrichment paths (cf. Ishimaru, Wanajo & Prantzos 2015). This procedure was then

further developed in 3D with full hydro and dark matter treatment (cf. Hirai et al. 2015), successfully reproducing both the early (low metallicity) onset and the correct scatter in the Galactic halo's r-process elemental abundances. However, this procedure only explains the abundances of the already *merged* systems whereas the individual *in-situ* enrichment paths have not yet been fully tested to reproduce actually *existing* and observed dwarf galaxy systems. (Low metallicity) r-process elemental abundance measurements of dwarf galaxy systems slowly become available (e.g., Jablonka et al. 2015; Simon et al. 2015; Tsujimoto et al. 2015; Ji et al. 2016). Despite that, only Tsujimoto & Nishimura (2015) investigated the *in-situ* enrichment path of a dwarf galaxies using a chemical evolution model. However, they used only a homogeneous, instantaneously mixing chemical evolution model, which is per se unable to explain the scatter seen in elemental abundance observations. Based on their considerations, we use our inhomogeneous chemical evolution model "ICE" (Wehmeyer et al. 2015) which relaxes the instantaneous mixing approximation to calculate the *in-situ* enrichment path of dwarf galaxies, and compare its predictions to the observations of the Draco dwarf galaxy.

3.3 The model

For the purpose of this work, the GCE modelling code ”ICE” (cf. Wehmeyer et al. 2015) is slightly modified to account for the specific properties of dwarf galaxies. In principle, we follow the modelling arguments of Tsujimoto & Nishimura (2015), who established a model which successfully reproduced the r-process element enrichment pattern of three dwarf galaxies: Draco, Sculptor and Carina. In contrast to the assumptions made in Wehmeyer et al. (2015), we use a steep IMF (with an integrated slope of -1.6) and a modified star formation history to account for the different star formation rate in Draco as described in Dolphin (2002). For the r-process elemental production sites, we consider magnetorotationally driven supernovae (MHD-SNe, e.g., Winteler et al. 2012; Nishimura et al. 2015) with an occurence rate of 0.005 or 0.007, and a neutron star merger occurrence rate of $4 * 10^{-4}$, both with respect to the ”standard” CCSN rate.

3.4 Observations

Observations of the europium enrichment abundances in dwarf galaxies are recently becoming available. We consider the Draco dwarf galaxy for out study. Observations are from Shetrone, Côté, Stetson (2001); Fulbright, Rich & Castro (2008); Cohen & Huang (2009); Tsujimoto & Nishimura (2015). The raw data compilation for this study were kindly provided by Takuji Tsujimoto & Nobuya Nishimura. For an overview of the observations see figure 3.1.

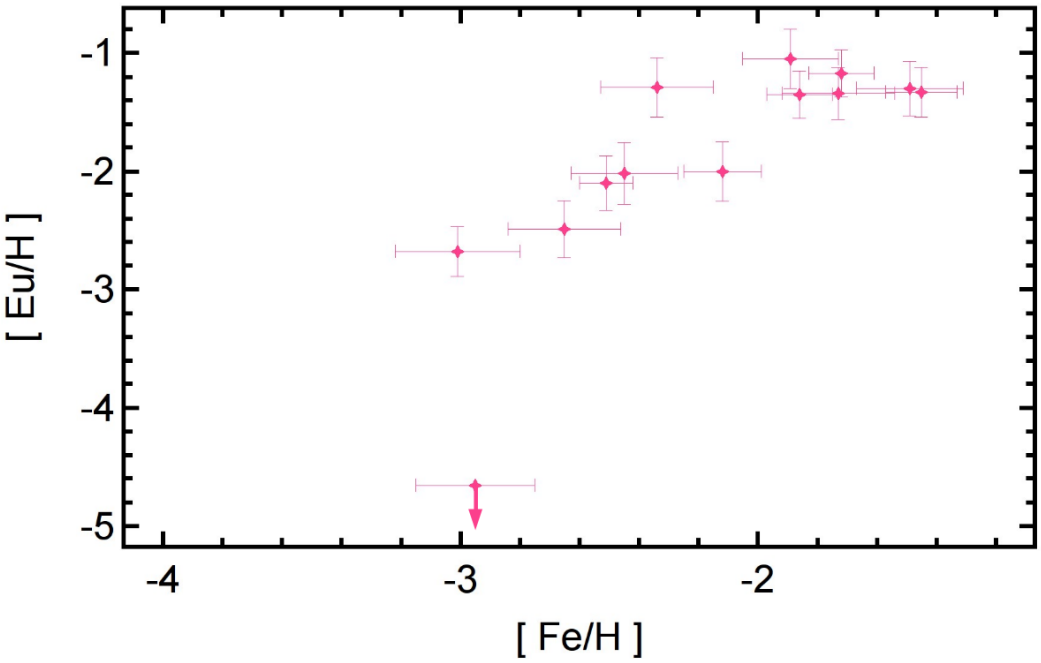

Fig. 3.1: Observed Eu abundances of the Draco dwarf galaxy. Except for the upper limit data point at [Eu/H]< 4.6, [Fe/H]≈ -2.95, a gradual increase is visible. Tsujimoto & Nishimura (2015) explain this difference with an initial "jump" in abundances together with a later "staircase-like" increase. Observations are from Shetrone, Côté, Stetson (2001); Fulbright, Rich & Castro (2008); Cohen & Huang (2009); Tsujimoto & Nishimura (2015), and compiled by Takuji Tsujimoto & Nobuya Nishimura.

3.5 Results

3.5.1 NSM as exclusive r-process site

When considering NSM as exclusive r-process site, the coalescence time scale is of major importance. For the purpose of this work, we consider a rather "standard" case, with a coalescence time scale of 10^8 years, as well as a case with very short (but probably unrealistically low) coalescence time scale of the order of 10^6 years. We also follow the considerations made by Ishimaru, Wanajo & Prantzos (2015), namely that a reduced star formation efficiency (SFE) leads to an earlier (lower metallicity) contribution to the r-process element enrichment by delayed processes such as neutron star mergers. A simple explanation for this effect is that less stars form during the fixed coalescence time scale of the neutron star mergers and thus less other stars are able to eject metals to the interstellar medium and increase the medium's metallicity while the two neutron stars sit idle and wait for their merger event at which they eject r-process matter.

Long coalescence time scales

Considering the r-process element enrichment path for long coalescence time scales (of the order of 10^8 years) for neutron star mergers as exclusive r-process site, our simulations show that the enrichment is in any case delayed (at too high metallicities) compared to the observations. With a standard star formation efficiency of 10^6, only slight enrichment takes place in the relevant metallicity range ($-5 \lessapprox$[Fe/H]$\lessapprox -1$). The bulk of r-process element enrichment takes place at higher metllicities. This can (partially) be cured applying the considerations of Ishimaru, Wanajo & Prantzos (2015), arguing that in lower mass systems, the enrichment pattern can be shifted towards lower metallicities by lowering the star formation efficiency. Our model with

reduced star formation efficiency (10^5) confirms this trend. In the relevant metallicity range, an enrichment "jump" occurs at [Fe/H]≈ -1.8, enriching the interstellar medium to abundances of [Eu/H]≈ -2. An illustration of the enrichment behaviour can be found in the left panel of fig. 3.2. This can be explained in the following way. When the star formation efficiency is lowered, less stars are born, evolve and explode in a CCSN during the coalescence time compared to the models with increased star formation efficiency. Since less stars produce less CCSNe, they also eject less metals to the insterstellar medium; Thus the medium's metallicity stays lower at the time of the first NSM. So, the first NSM is able to eject r-process elements at lower metallicities than in the higher star formation efficiency models. When applying the instantaneous mixing approximation, this shifting effect is lowered. This is because *any* ejecta from *anywhere* in the simulation volume contribute to the local metallicity. Since the delay effect as imposed by the coalescence time is a very *localized* effect, it is lowered when removing the importance of local effects (i.e., applying instantaneous mixing). *NB. When applying instantaneous mixing, the shifting towards lower metallicities is so strong that even the standard star formation efficiency model case will shift its enrichment jump into the relevant metallicity range.* An illustration of the enrichment behaviour when applying instantanous mixing can be found in the right panel of fig. 3.2. Although the model with lowered star formation efficiency has its enrichment jump occuring at far lower metallicity than higher star formation efficiency models, the enrichment path still proceeds at too high metallicities compared to the actual observations. As a result, it is very difficult to explain the observations when considering neutron star mergers with long coalescence time scale as exclusive r-process sites.

Low coalescence time scales

When considering NSMs as exclusive r-process site while applying a (probably unrealistically) low coalescence time scale of the order of 10^6 years, we can

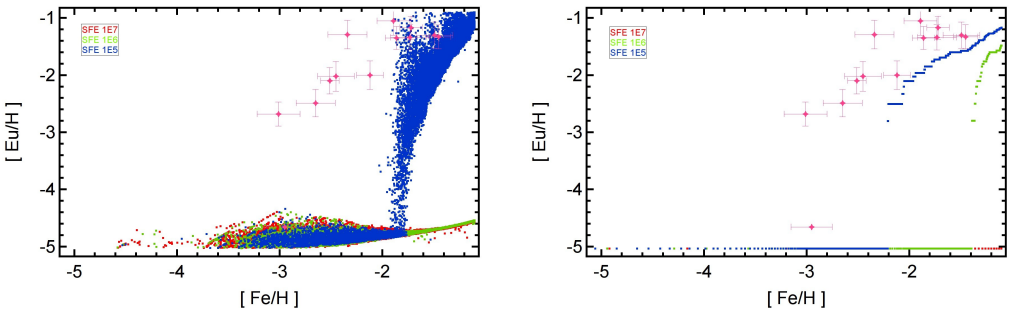

Fig. 3.2: Left panel: Effect of altered star formation efficiency on r-process enrichment when neutron star mergers act as exclusive r-process site and coalescence times are fixed to 10^8 years. Pink stars represent observations. Red dots represent model stars with a SFE of 10^7, green dots represent model stars with a SFE of 10^6, and blue dots represent model stars with a SFE of 10^5. Right panel: Same as left panel, but with applied instantaneous mixing approximation.

observe a different behaviour in the r-process enrichment. When such low coalescence time scales are applied, all models with star formation efficiency in the range $10^5 <$ SFE $< 10^7$ show a significant contribution to the r-process enrichment in the relevant metallicity range ([Fe/H]$\lessapprox -1$). In the following, the effect of the different star formation efficiencies on the r-process element enrichment are discussed. First, the behaviour in the inhomogeneous case is discussed (i.e., the instantaneous mixing approximation is not applied).

- When applying a high star formation efficiency 10^7, a bulk of unenriched stars ([Eu/H]≈ -5) forms in the metallicity range $-3.6 \lessapprox$[Fe/H]$\lessapprox -1.6$. At [Fe/H]≈ -1.6, a jump in the r-process abundance occurs, which enriches stars up to an enrichment level of [Eu/H]≈ -1, with an abundance spectrum of the order of ≈ 2 dex. This spectrum, however, decreases and the abundance curve converges to a value of the order of [Eu/H]≈ -1.9. An illustration of the enrichment behaviour can be found in the left panel of fig. 3.3.

- When applying a standard star formation efficiency 10^6, a bulk of unenriched stars ([Eu/H]≈ -5) forms in the metallicity range $-3.4 \lessapprox$[Fe/H]$\lessapprox -1.8$. At [Fe/H]≈ -1.8, a jump in the r-process abundance occurs,

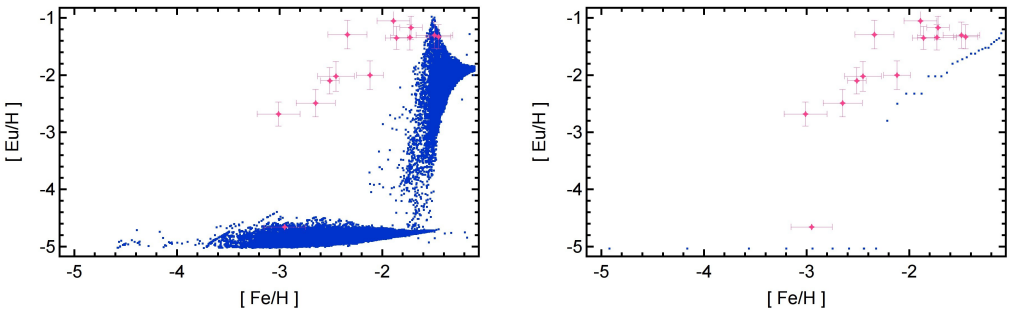

Fig. 3.3: Left panel: Effect of increased star formation efficiency on r-process enrichment when neutron star mergers act as exclusive r-process site and coalescence times are fixed to 10^6 years. Pink stars represent observations. Blue dots represent model stars with a SFE of 10^7. Right panel: Same as left panel, but with applied instantaneous mixing approximation.

which enriches stars up to an enrichment level of [Eu/H]≈ -1. However, the enrichment continuously increases after the jump towards higher metallicities. An illustration of the enrichment behaviour can be found in the left panel of fig. 3.4.

- When applying a lowered star formation efficiency 10^5, the bulk of unenriched stars ([Eu/H]≈ -5) forms in a decreased metallicity range $-3.4 \lessapprox$[Fe/H]$\lessapprox -2.6$. At [Fe/H]≈ -2.6, a (compared to the higher SFE models) moderate (of the order of 2 dex) jump in the r-process abundance occurs. However, the enrichment behaviour is much smoother compared to the higher SFE cases, and this trend continues also towards higher metallicities. An illustration of the enrichment behaviour can be found in the left panel of fig. 3.5.

A comparison of the effects of varied star formation efficiency while keeping the coalescence time scale constant can be found in the left panel of figure 3.6.

These effects might be explained in the following way.

- *Occurrence and shape of the jump in enrichment.* At high star formation efficiencies, the enrichment jump occurs at higher metallicities. At lower star formation efficiencies, the enrichment jump occurs at lower metallicities. During the coalescence time, the star formation efficiency

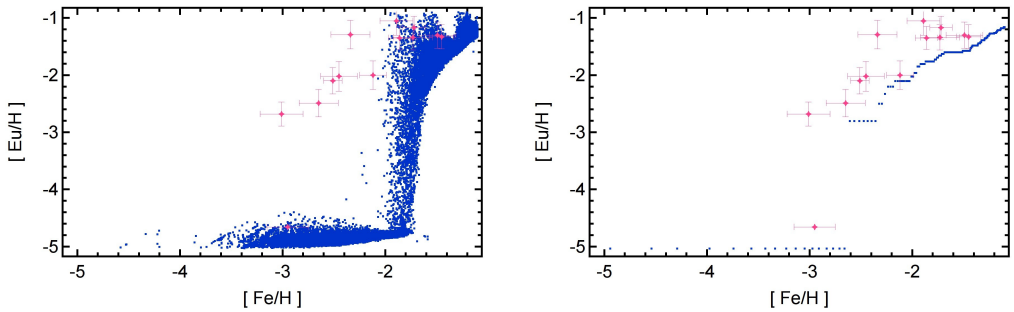

Fig. 3.4: Left panel: Effect of standard star formation efficiency on r-process enrichment when neutron star mergers act as exclusive r-process site and coalescence times are fixed to 10^6 years. Pink stars represent observations. Blue dots represent model stars with a SFE of 10^6. Right panel: Same as left panel, but with applied instantaneous mixing approximation.

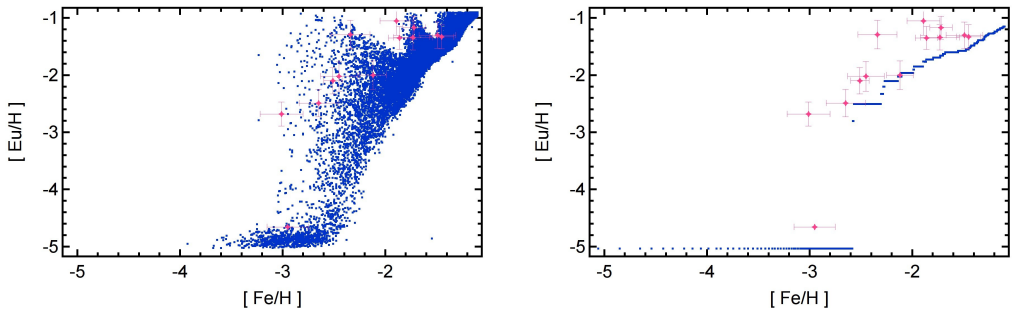

Fig. 3.5: Left panel: Effect of lowered star formation efficiency on r-process enrichment when neutron star mergers act as exclusive r-process site and coalescence times are fixed to 10^6 years. Pink stars represent observations. Blue dots represent model stars with a SFE of 10^5. Right panel: Same as left panel, but with applied instantaneous mixing approximation.

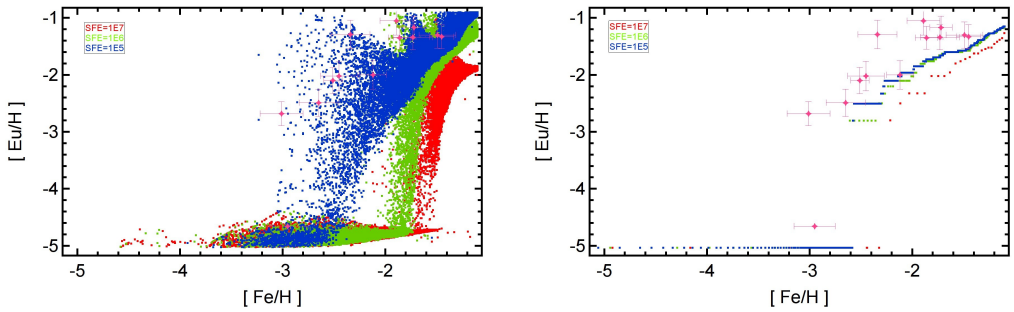

Fig. 3.6: Left panel: Effect of altered star formation efficiency on r-process enrichment when neutron star mergers act as exclusive r-process site and coalescence times are fixed to 10^6 years. Pink stars represent observations. Red dots represent model stars with a SFE of 10^7, green dots represent model stars with a SFE of 10^6, and blue dots represent model stars with a SFE of 10^5. Right panel: Same as left panel, but with applied instantaneous mixing approximation.

has a large impact on how many other stars are born and die in the immediate neighbourhood of the two neutron stars. These surrounding stars eject metals via CCSNe and thus increase the ISM's metallicity. This explains why the actual enrichment jump occurs in an environment with a higher metallicity when the star formation efficiency is increased, since in this case more stars could form in the coalescence time of the two neutron stars. If the star formation efficiency is lowered, less stars produce less CCSNe during the coalescence time scale, and thus less metals are ejected into the interstellar medium, hence the medium's metallicity is lower when the actual NSM event occurs.

- *Behaviour after occurrence of the enrichment jump.* The faster convergence after the initial enrichment jump when applying higher star formation efficiencies can be explained by the *log*-scale of the metallicity. For all models, a similar number of CCSNe in order to move around the enriched gas throughout the simulation cell is necessary. However, the first enrichment jump occurs at different metallicities. In the case with lowered SFE, the jump occurs very early, so the metallicity difference provided by those CCSNe which move the enriched gas around and thus equilibrate the enrichment is much larger than in the case with higher SFE. While the *number* of CCSNe and also the *amount* of metals which these CCSNe emit is approximately similar, the effect of the increase of the metallicity is much larger at lower metallicities because of the *log*-scale of the metallicity.

When applying the instantaneous mixing approximation, the effect is not so significant any more.

- The bulk of unenriched stars ([Eu/H]≈ -5) is not visible any more.

- The enrichment jump occurs at similar metallicities. (at least for standard and lowered SFE).

- The increase in enrichment after the jump is much more similar under varied SFE.

For an illustration of the enrichment behaviour with applied instantaneous mixing approximation can be found in the right panels of figs. 3.3, 3.4, and 3.5; A comparison between these cases can be found in the right panel of figure 3.6. These effects might be explained in the following way.

- *Bulk formation.* The disappearance of the bulk of unenriched stars before the enrichment jump when applying the IMA is probably an optical illusion. Since all stars will immediately inherit the ejecta of any nucleosynthesis event, they will be pushed at the exact same spot on the enrichment diagram as any other star in the simulation volume. Although it seems as if the bulk has disappeared, it just consists of many overlying stars.

- *Reduction of the shift of the enrichment jump and behaviour after the jump.* This is explained with the fact that all of the effects while not applying IMA show a very *localized* behaviour of the enrichment. When IMA is applied, metal-ejecting CCSNe situated *anywhere* in the simulation volume contribute to the overall metal enrichment throughout the whole simulation volume, thus smear out the effects of faster or slower local r-process enrichment. Only in the case with increased SFE, the significantly enhanced star formation (in comparison to the coalescence time scale) and thus the significantly higher amount of metals ejected per coalescence time shows the effect of shifting the enrichment towards higher metallicities.

Although the model with lowered star formation efficiency has some outliers which match the observations (of the enriched stars) at lowest metallicities ([Fe/H]$\lessapprox -2.5$), the bulk of model stars behaves completely different, and the bulk enrichment path proceeds at too high metallicities. This is even worse for the models with moderate or increased star formation efficiency, which

do not even have outlier model stars at the spot of the actual observed low metallicity (r-process enriched) stars. As a result, it is difficult to explain the observations when considering neutron star mergers as exclusive r-process sites.

Comparing coalescence time scales

This sub-section considers the effect of altered coalescence time scale on the enrichment of r-process elements. Since for long coalescence time scales (10^8 years), only the case with lowered star formation efficiency (10^5) shows an enrichment jump in the relevant metallicity range, we only compare the cases with the lowered SFEs. While the enrichment jump occurs at much lower metallicities ([Fe/H]≈ -2.6) in the lowered coalescence time scale model, the enrichment jump occurs at much higher metallicities ([Fe/H]≈ -1.8) in the increased coalescence time scale model. The bulk of unenriched stars ([Eu/H]≈ -5) in the lower SFE model extends over a smaller metallicity range of $-3.4 \lessapprox$[Fe/H]$\lessapprox -2.6$ than the metallicity range $-3.4 \lessapprox$[Fe/H]$\lessapprox -1.8$ in the model with increased coalescence time scale. After the convergence of the first enrichment jump(s) of the respective model, their abundance curve converges against each other. An illustration of the different enrichment behaviour under varied coalescence time scale can be found in fig. 3.7. This behaviour can be explained in the following way.

- *Enrichment jump and bulk formation.* In the low coalescence time model, significantly less time passes before the first r-process event compared to the longer coalescence time model. This leads to less star formation and thus less CCSNe occuring before the first r-process event in the low coalescence time scale model. The decreased occurrence of CCSNe leads to less metals ejected before the first r-process event, hence the metallicity is lower at the time of the event. In the increased coalescence time model, the time until the first r-process event is longer,

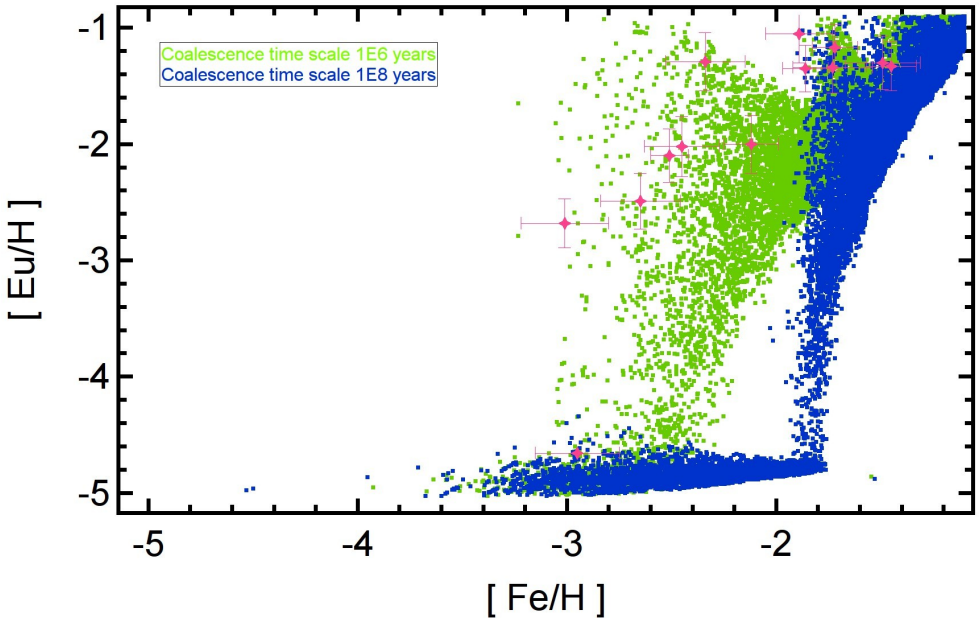

Fig. 3.7: Effect of different coalescence time scales on r-process enrichment when neutron star mergers act as exclusive r-process site. Pink stars represent observations. Green dots represent model stars with a when neutron stars mergers have a fixed coalescence time scale of the order of 10^6 years, blue dots represent model stars with a when neutron stars mergers have a fixed coalescence time scale of the order of 10^8.

hence more stars had time to be born, evolve and undergo a CCSN, enriching the ISM with metals and thus increasing its metallicity. The bulk sets in at similar metallicities, but the enrichment jump occurs at much higher metallicities for the increase coalescence time scale case. This explains the much larger bulk in this case.

- *Asymptotic behaviour after the enrichment jump.* In principle the behaviour is of both models is similar: After a first enrichment jump, the spectrum of the enrichment decreases, then the enrichment increases gradually. This behaviour follows the same pattern, but with much narrower spread in metallicity for the longer coalescence time scale model. This can be explained by the *log*-scale of the metallicity. At higher metallicities, the differences in the *amount* of metals is much narrower in the [Fe/H] space. In fact, the longer coalescence time model approximately mimics the behaviour of the enrichment curve of the lower

coalescence time scale model, only shifted towards higher metallicities: For instance, while the the respective jumps occur at [Fe/H]≈ -2.6 and ≈ -1.8, the metallicity difference at [Eu/H]≈ -1 is only Δ [Fe/H]≈ 0.1 at metallicities that high ([Fe/H]≈ -1.2). Although the difference in the *amount* of metals is still roughly conserved, the *log*-scale decreases the shifting effect of lowered and increased coalescence time scale at higher metallicities.

The conclusions of this comparison of the effect of altered coalescence time scales are congruent with those of the previous paragraphs (since the same models were used): NSMs have difficulties to explain the observed abundances when considered as exclusive r-process production site.

3.5.2 MHD-SNe as exclusive r-process site

When considering MHD-SNe as exclusive r-process site, we follow the assumptions made in Tsujimoto & Nishimura (2015). When applying an instantaneous mixing approximation, we can basically confirm the conclusions drawn in Tsujimoto & Nishimura (2015). The europium floor stays at [Eu/H]$= -5$ for metallicities lower than [Fe/H]$\lessapprox -3.2$. At this metallicity, the first r-process event pushes the Eu abundance in the region of [Eu/H]≈ -3. From here on, one can observe a "ladder-like" increase in the Eu abundance, with the steps correlated to the occurrence of r-process events. See fig. 3.8 for an illustration of this model.

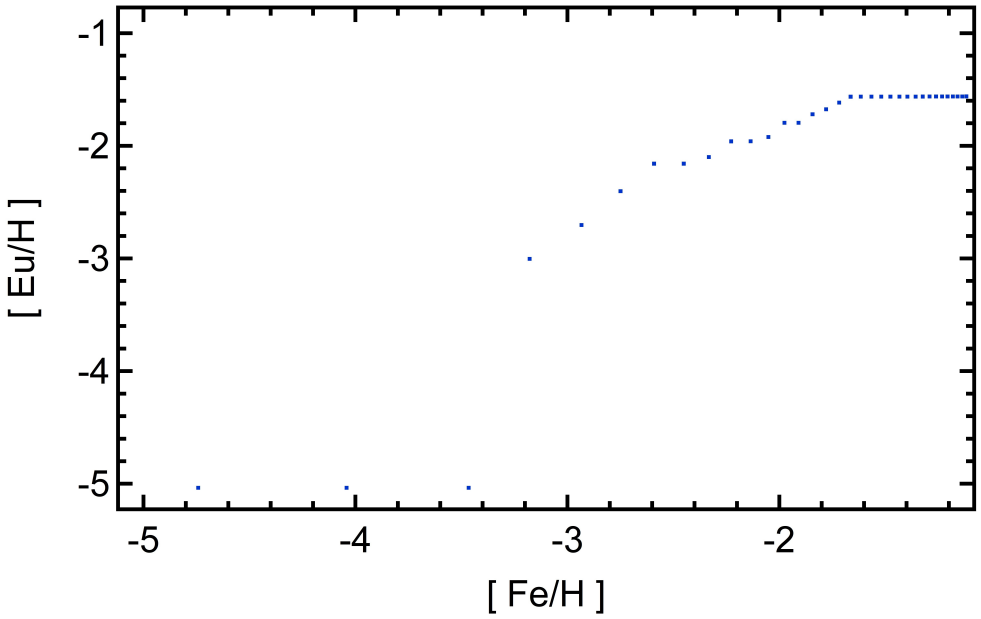

Fig. 3.8: Predicted evolution of Eu enrichment in the Draco dwarf galaxy. Pink stars represent observations. Blue dots represent model stars with a MHD-SN probability of 0.005)

When relaxing the instantaneous mixing approximation (IMA), the results are slightly different, but are still in general agreement with the calculations of Tsujimoto & Nishimura (2015). In contrast to the case where the IMA is applied, we cannot observe a constant europium floor until the first jump is increasing the abundance promptly. Here, we rather observe a quick increase in metallicity with not many stars in the region [Fe/H]< 3.5. This quick increase in metallicity leads to a bulk of stars at $-3.4 \lessapprox$[Fe/H]$\lessapprox -2.5$ / [Eu/H]≈ -5 waiting for the first r-process production event. The first r-process event then enriches its neighbourhood stars highly in Eu, which leads to a high r-process elemental abundance in these stars. However, the low rate of this event leads to an r-process enrichment only regionally, and is thus affecting only few stars; The bulk of unenriched stars stays at low [Eu/H]. As continuously additional ”standard” supernovae occur, the locally highly enriched gas gets moved throughout the simulation volume and diluted (mixed with unenriched gas). The bulk of stars is then only affected by a diluted enriched gas and thus these stars become enriched only slowly and

not as promptly as in the IMA case. Hence, this ”dilution” effect also explains why our model predicts quite a large spectrum in the enrichment abundances. At metallicities higher than [Fe/H] $\gtrapprox -2.5$, also the last of the low enrichment bulk stars have experienced an r-process element enrichment and so, also the lower end of the enrichment spectrum moves towards higher r-process element enrichment (towards higher values of [Eu/H]). See figure 3.9 for the simulated abundance evolution curve. We conclude that MHD-SNe acting as exclusive r-process site might explain the observed abundances in the Draco dwarf galaxy.

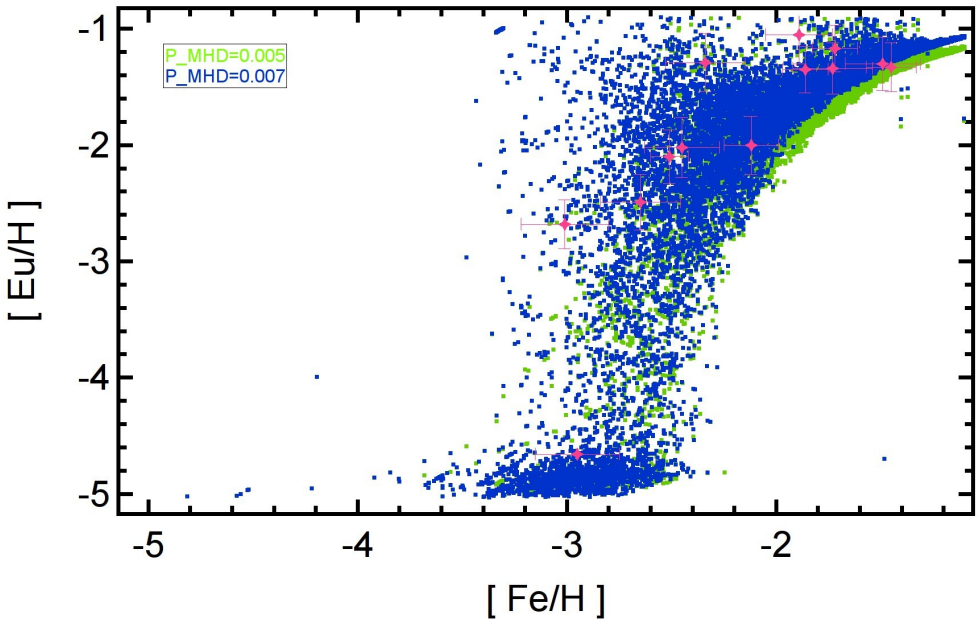

Fig. 3.9: Predicted evolution of Eu abundances when considering MHD-SNe as exclusive r-process site. Pink stars represent observations. Blue dots represent model stars with a MHD-SN probability of 0.007; Green dots represent model stars with a MHD-SN probability of 0.005.

3.5.3 Combination of sites

In the previous pragraphs, we came to the conclusions that MHD-SNe might explain the r-process elemental abundances in the Draco dwarf galaxy, whereas NSMs have difficulties to do so when considered as exclusive r-process production site. In this section, we test whether a combined model

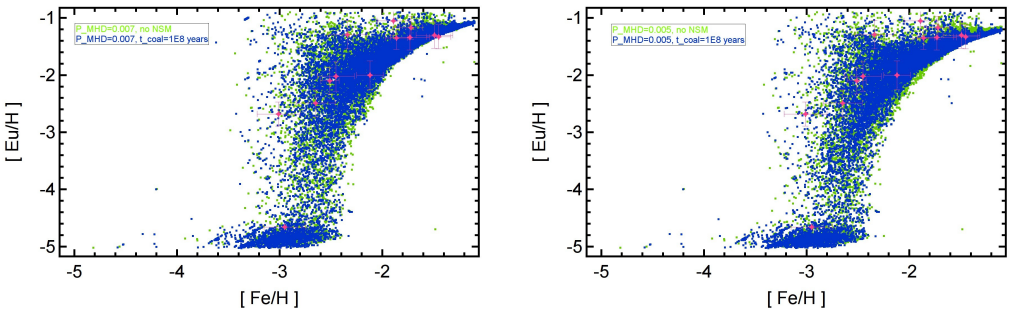

Fig. 3.10: Comparison of considering MHD-SNe as exclusive r-process site (model stars: green dots) vs. a combined model with both MHD-SNe and NSM (with long coalesence time of the order of 10^8 years) as r-process sites (model stars: blue dots). Pink stars represent observations. Left panel: MHD-SN probability of 0.007; Right panel: MHD-SN probability of 0.005.

with both MHD-SNe and NSMs acting as r-process production sites might still explain the observations. Firstly, we discuss the case with long coalescence time scales for neutron star mergers. We have already seen in section 3.5.1, that if we consider long coalescence time scales for NSMs, the enrichment effect in the relevant metallicity range is marginal. Therefore, when adding the contribution of NSM with long coalescence time scales to the enrichment provided by MHD-SNe, the effect is also marginal. A comparison of the additional enrichment in r-process elements of long coalescence NSMs to an environment with MHD-SNe already acting as r-process site with high ($P_{MHD} = 0.007$) and low ($P_{MHD} = 0.005$) MHD-SN probability can be found in figure 3.10. Instead, when considering the effect of adding NSMs with (probably unrealistically) low coalescence time scales (of the order of10^6 years) as additional site to MHD-SNe, the situation is different. We have already seen in section 3.5.1, that NSMs with short coalescence time scales might significantly contribute to the r-process elemental enrichment. Now, when adding NSMs with a short coalescence time scale to an environment where MHD-SNe already act as r-process site, the enrichment in r-process elements is enhanced (see figure 3.11): While at lower metallicities ([Fe/H]$\lessapprox 1.6$), we observe that the r-process element enrichment curve is shifted towards lower metallicities by Δ[Fe/H]≈ 0.1 (the effect is stronger when we assume the reduced MHD-SN probability of $P_{MHD} = 0.005$), the effect at higher metallicities

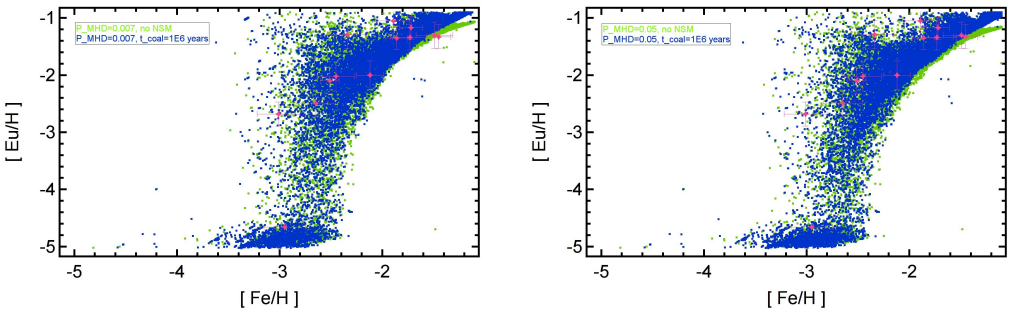

Fig. 3.11: Comparison of considering MHD-SNe as exclusive r-process site (model stars: green dots) vs. a combined model with both MHD-SNe and NSM (with short coalesence time of the order of 10^6 years) as r-process sites (model stars: blue dots). Pink stars represent observations. Left panel: MHD-SN probability of 0.007; Right panel: MHD-SN probability of 0.005.

([Fe/H]$\gtrapprox 1.6$) is different. At this stage, NSMs start to contribute strongly to the overall r-process enrichment and thus shift the r-process element enrichment curve towards higher enrichment (higher [Eu/H]). The effect is stronger in the case when contributing to the reduced MHD-SN probability ($P_{MHD} = 0.005$) case, since with assumed constant NSM contribution in both models, the *fraction* of r-process element contribution by NSMs is larger when considering less contribution by MHD-SNe. Hence, the difference in r-process enrichment when comparing MHD-SNe as exclusive r-process site vs. a combined environment with both NSM and MHD-SNe as r-process sites is larger when considering a lower rate of MHD-SNe. We note, however, that the model employing a combined environment of NSMs (of long coalescence time scales) and MHD-SNe as r-process sites, the observations at higher metallicities ([Fe/H]$\lessapprox 1.6$) are slightly off the predicted abundance curve. This fact (together with the assumption that NSMs with a coalescence time scale of the order of 10^6 years are in either case probably an unrealistic assumption) leads to the conclusion that only a model with a combined environment with both MHD-SNe and NSMs (with *long* coalescence time scale of the order of 10^8 years) should be considered as a realistic scenario for the r-process enrichment in the Draco dwarf galaxy. An illustration of a comparison of the effects of considering either a low or high probability of MHD-SNe acting as r-process site together with NSMs with long coalescence

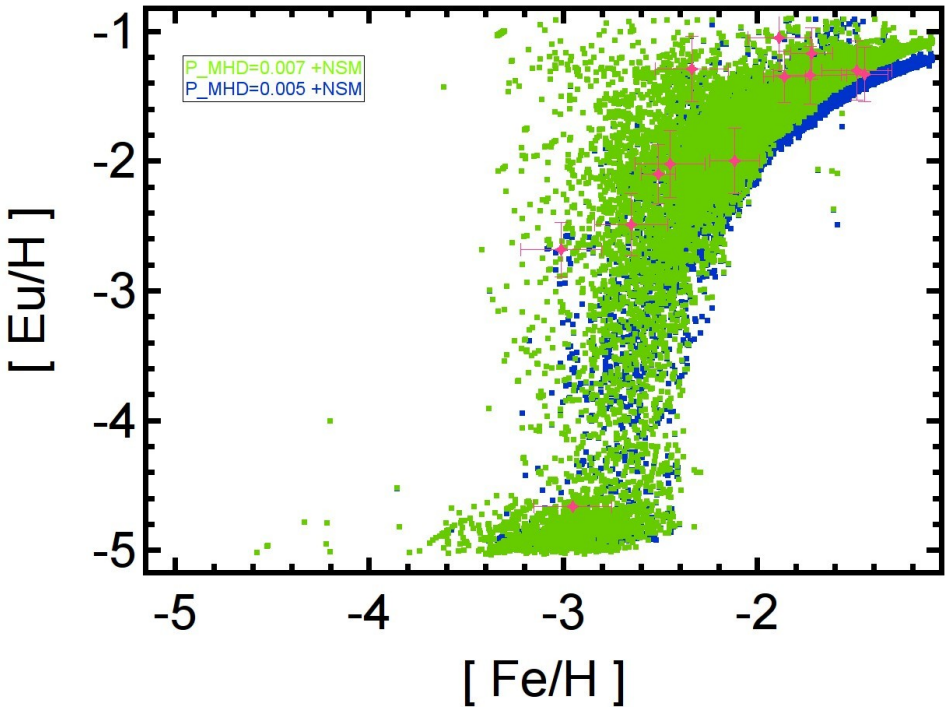

Fig. 3.12: Comaprison between high (0.007; model stars: green dots) and low (0.005; model stars: blue dots) probability of MHD-SNe when considering both MHD-SNe and NSMs (with long coalescence time scale of 10^8 years) as r-process production sites. While both models might explain the observations (pink stars) the lower MHD-SNe probability model (blue dots) explains observations better when assuming maximum observational errors, especially at higher metallicities.

time scale can be found in figure 3.12. We note that both of these scenarios might well explain the observations of r-process element enrichment in the Draco dwarf galaxy, with the low MHD-SNe probability case being slightly better at higher metallicities.

3.6 Conclusions and discussion

We have considered the r-process element enrichment in the Draco dwarf galaxy via the europium enrichment. We follow the argumentations of Tsujimoto & Nishimura (2015), who consider a constant r-process floor ([Eu/H]≈ -5) up to a metallicity of [Fe/H]≈ -2.9. Then, an "enrichment jump" occurs (up to an enrichment of [Eu/H]≈ -2.6), followed by a gradual increase in r-process enrichment up to a "ceiling" which is reached at Fe/H]≈ -2, with an enrichment of the order of $-1.6 \lessapprox$[Eu/H]$\lessapprox -1$. We have examined different scenarios on how to reproduce the shape of this enrichment:

1. NSM as exclusive r-process production site, with varied star formation efficiencies, as suggested by Ishimaru, Wanajo & Prantzos (2015).

    - *NSMs with long coalescence time scales:* This r-process production site (with coalescence time scales of the order of 10^8 years) contributes their r-process production at too high metallicities beyond the relevant metallicity range. Only if significantly lowered star formation efficiency is assumed, the enrichment contribution of this nucleosynthesis site is within the relevant metallicity range, however, the contribution still sets in at too high metallicities.

    - *NSMs with short coalescence time scales:* When considering NSMs with (probably unrealistically) short coalescence time scales of the order of 10^6 years, their contribution to the r-process element enrichment lies in the relevant metallicity range. A scenario with significantly lowered star formation efficiency (10^5) might explain the observations of the r-process enrichment in the Draco dwarf galaxy, however, some of the observations are only explained by extreme outliers of the calculated enrichment curve provided by

this scenario, while the bulk of model stars proceeds at higher metallicities.

2. *MHD-SNe as exclusive r-process production site, with varied star occurrence rate, as suggested by Tsujimoto & Nishimura (2015):* An environment with MHD-SNe as exclusive r-process site might well explain all the features of the observed enrichment in the Draco dwarf galaxy. While the predicted enrichment curve in the scenario with high occurrence of MHD-SNe proceeds at lower metallicity due to the higher amount of r-process elements ejected per time step, the scenario with the lowered occurrence rate of MHD-SNe better fits the observed enrichment features.

3. *Combined environment with both MHD-SNe and NSMs as r-process sites:*

   - When considering both MHD-SNe and NSMs with low coalescence time scale as r-process site, the predicted enrichment curve proceeds too high compared to observations.

   - When considering both MHD-SNe and NSMs with high coalescence time scale as r-process sites, the predicted enrichment curve well explains the features of the observed enrichment path.

As an additional conclusion, it is remarkable that, when applying an instantaneous mixing approximation, the abundance predictions are shifted significantly towards lower metallicities (for appropriate star formation efficiencies). This approximation might probably be considered as an upper limit for the effects of strong mixing in a simulated volume. It is though remarkable that, even with IMA applied, NSMs still have difficulties to explain the observed r-process enrichment at low metallicities.

Discussion. Considering neutron star mergers, the low coalescence time scale case (10^6 years) is probably not a valid channel of this nucleosynthesis site and consequently should be considered only as an illustration of the upper

limit of the effects of lowered coalescence time scales. In general, probably delay time distribution functions accounting for the different channels of this nucleosynthesis site should be employed instead of using a single, fixed time scale for all NSMs.

Considering the various mixing effects of dwarf galaxy systems (including the gas shifting by supernova explosions), these are difficult to mimic in our simulation environment. Modified (and probably for the simulation of dwarf galaxy systems more accurate) mixing might shift the predicted abundance curves to higher or lower metallicities. However, the instantaneous mixing models provided in this work can possibly be seen as an upper limit of this effect, since all matter is assumed to mix with the whole volume instantaneously, which is certainly an upper limit of all possible mixing effects.

Bibliography

Arnett, D., ”Supernovae and Nucleosynthesis”, 1996, Princeton University Press, ISBN: 0-691-01147-8

Argast, D., Samland, M., Thielemann, F.-K. and Qian, Y.-Z., 2004 A&A 416, 997–1011

Arcones, A., Thielemann, F.-K., 2013 JPhG 40 013201 DOI: 10.1088/0954-3899/40/1/013201

Arlandini, C., Käppeler, F., Wisshak, K., Gallino, R., Lugaro, M., Busso, Ma., Straniero, O., 1999 ApJ 525 886-900, DOI:10.1086/307938

Audouze, J., Tinsley, B.M., 1976 AR A&A 14 43-79 DOI:10.1146/annurev.aa.14.090176.000355

Barklem, P. S, et al. 2005, A&A, 439, 129

Bauswein, A., Goriely, S., Janka, H.-T., 2013 ApJ 773 :78

Bauswein, A., Pulpillo, R. A., Janka, H. T., Goriely, S., 2014 ApJL 795 (1) L9 DOI:10.1088/2041-8205/795/1/L9

Bensby, T., Feltzing, S., Oey, M. S., 2014 A&A 562, id. A71

Berghöfer & Breitschwerdt, 2002 A&A 390, 299

Bisterzo, S., Travaglio, C., Gallino, R., Wiescher, M., Käppeler, F., 2014 ApJ 787: 10,14, DOI:10.1088/0004-637X/787/1/10

Bravo, E., Domínguez, I., Badenes, C., Piersanti, L., Straniero, O., 2010 ApJL 711, L66-L70, DOI:10.1088/2041-8205/711/2/L66

Burrows, A., Hayes, J., Fryxell, B. A., 1995 ApJ 450, 830

Cameron, A.G.W., 2001 ApJ 562 456-469 DOI: 10.1086/323869

Cescutti, G., Chiappini, C., Hirschi, R., Meynet, G., Frischknecht, U., 2013 A&A 553: UNSP A51, DOI: 10.1051/0004-6361/201220809

Cescutti, G., Romano, D., Matteucci, F., Chiappini, C., Hirschi, R. 2015 A&A 577, 139

Cescutti, G., Chiappini, C., 2014 A& A 565 DOI: 10.1051/0004-6361/201423432

Chiappini, C., Matteucci, F., Gratton, R. 1997, ApJ 477, 765

Chiappini, C., Matteucci, F., Romano, D., 2001 ApJ 554 1044-1058

Cohen, J. G., Huang, W. 2009 ApJ, 701, 1053

Cowan, Thielemann & Truran, "The Nuclear Evolution of the Universe", in preparation

De Donder, E., Vanbeveren, D., 2003 New Astronomy 8 415-425

Dolphin, A. E., 2002 MNRAS 332, 91

Eichler, M., Arcones, A., Kelic, A., Korobkin, O., Langanke, K., Martinez-Pinedo, G., Panov, I. Rauscher, T., Rosswog, S., Winteler, C., Zinner, N.T., Thielemann, F.-K. 2015 ApJ 808 id.30

François, P. et al. 2007 A&A, 476, 935

Freiburghaus, C., Rosswog, S., Thielemann, F.-K., 1999 ApJ 525 L121

Fujimoto, S., Hashimoto, M., Kotake, K., Yamada, S., 2006 Origin of Matter and Evolution of Galaxies 847, 386-388

Fujimoto, S., Nishimura, N., Hashimoto, M., 2008 ApJ 680 1350-1358 DOI:10.1086/529416

Fulbright, J. P., Rich, R. M., & Castro, S. 2004 ApJ 612, 447

Fischer, T., Whitehouse, S. C., Mezzacappa, A., Thielemann, F.-K., Liebendörfer, M., 2010 A&A 517 A80, DOI:10.1051/0004-6361/200913106

Fröhlich, C., Martinez-Pinedo, G., Liebendörfer, M., Thielemann, F.-K., Bravo, E., Hix, W., Langanke, K., Zinner, N., 2006 PRL 96 14 142502, DOI: 10.1103/PhysRevLett.96.142502

Fröhlich, C., Hauser, P., Liebendörfer, M., Martínez-Pinedo, G., Thielemann, F.-K., Bravo, E., Zinner, N. T., Hix, W. R., Langanke, K., Mezzacappa, A., Nomoto, K. 2006 ApJ 637 415-426, DOI:10.1086/498224

García Pérez, A. E., Allende Prieto, C., Holtzman, J. A., Shetrone, M., Mészáros, Sz., Bizyaev, D., Carrera, R., Cunha, K., García-Hernández, D. A., Johnson, J. A., Majewski, S. R., Nidever, D. L., Schiavon, R. P., Shane, N., Smith, V. V., Sobeck, J., Troup, N., Zamora, O., Weinberg, D. H., Bovy, J., Eisenstein, D. J., Feuillet, D., Frinchaboy, P. M., Hayden, M. R., Hearty, F. R., Nguyen, D. C., O'Connell, R. W., Pinsonneault, M. H., Wilson, J. C., Zasowski, G., 2016 ApJ 151, id. 144

Geisler, D., Smith, V. V., Wallerstein, G., Gonzalez, G., Charbonnel, C., 2005 AJ, 129,1428

Gibson, B. K., Fenner, Y., Renda, A., Kawata, D., Lee, H., 2003 Publications of the Astronomical Society of Australia, 20 4 401-415, DOI: 10.1071/AS03052

Greggio, L., A&A 441, 1055-1078 DOI: 10.1051/0004-6361:20052926

Goriely, S., Bauswein, A., Janka, H.T., 2012 Nuclear Physsics in Astrophysics V 337 012039 DOI: 10.1088/1742-6596/337/1/012039

Goriely, S., Sida, J.-L., Lemaître, J.-F., Panebianco, S., Dubray, N., Hilaire, S., Bauswein, A., Janka, H.-T., (2013) PRL 111, 24, DOI:10.1103/PhysRevLett.111.242502

Goswami, A., Prantzos, N., 2000 A&A, 359, 191-212

Henbest, N. & Couper, H., The Guide to the Galaxy (1996), ISBN 3-7643-2535-3

Hester, J. J. 2008 AR A&A 46 127–155 DOI:10.1146/annurev.astro.45.051806.110608

Hüdepohl, L., Müller, B., Janka, H.T., Marek, A., Raffelt, G..G, 2010 PRL 104 251101 DOI:10.1103/PhysRevLett.104.251101

Hirai, Y., Ishimaru, Y., Saitoh, T. R., Fujii, M. S., Hidaka, J., Kajino, T., 2015 ApJ 814, 41

Hix, W., Lentz, E., Endeve, E., Baird, M., Chertkow, M., Harris, J.„ Messer, O. E., Mezzacappa, A., Bruenn, S., Blondin, J., 2014 AIP Advances 4 041013, DOI:10.1063/1.4870009

Honda, S., Aoki, W., Ishimaru, Y., Wanajo, S., Ryan, S. G., 2006 ApJ 643 1180

Ishimaru, Y. & Wanajo, S., 1999 ApJ 511 L33-L36 DOI: 10.1086/311829

Ishimaru, Y., Wanajo, S., Prantzos, N., (2015) ApJL 804L 35I, DOI: 10.1088/2041-8205/804/2/L35

Iwamoto, K., Brachwitz, F., Nomoto, K., et al. 1999, ApJS 125 439-462, DOI:10.1086/313278

Jablonka, P., North, P., Mashonkina, L., Hill, V., Revaz, Y., Shetrone, M., Starkenburg, E., Irwin, M., Tolstoy, E., Battaglia, G., Venn, K., Helmi, A., Primas, F., François, P., 2015 A&A 583, A67

Janka, H.-T. and Müller, E., 1996 A&A 306, 167

Ji, A. P., Frebel, A., Chiti, A., Simon, J. D. , 2016 Nature 531, 610

Jones, S., Hirschi, R., Nomoto, K., Fischer, T., Timmes, F. X., Herwig, F., Paxton, B., Toki, H., Suzuki, T., Martínez-Pinedo, G., Lam, Y. H., Bertolli, M. G., 2013 ApJ 772 2 150

Just, O. et al. 2014, arXiv1406.2687

Käppeler, F., Gallino, R., Bisterzo, S., Aoki, W., 2011 RvMP, 83 157-194, DOI:10.1103/RevModPhys.83.157

Kalogera, V., Kim, C., Lorimer, D.R., Burgay, M., D'Amico, N., Possenti, A., Manchester, R.N., Lyne, A.G., Joshi, B.C., McLaughlin, M.A., Kramer, M., Sarkissian, J.M., Camilo, F., 2004 ApJ 601 L179-L182

Kennicutt, R. C. Jr., 1998 ApJ 498:541, DOI:10.1086/305588

Kobayashi, C., Umeda, H., Nomoto, K., Tominaga, N., Ohkubo, T., 2006 ApJ 653 1145-1171

Kobayashi, C., 2012 AIPC 1484 90-98, DOI: 10.1063/1.4763379

Korobkin, O., Rosswog, S., Arcones, A., Winteler, C., MNRAS 2012 426 1940-1949. DOI: 10.1111/j.1365-2966.2012.21859.x

Kouveliotou, C., Dieters, S., Strohmayer, T., et al. 1998, Nature, 393, 235

Kramer, M. 2009, in IAU Symp. 259, Cosmic Magnetic Fields: From Planets, to Stars and Galaxies, ed. K. G. Strassmeier, A. G. Kosovichev, & J. E. Beckman (Cambridge: Cambridge Univ. Press), 485

Kratz, K.-L., Farouqi, K., Mashonkina, L. I., Pfeiffer, B., 2008 New Astronomy Reviews 52 390-395, DOI:10.1016/j.newar.2008.06.015

Kuroda, T., Kotake, K., Takiwaki, T., 2012 ApJ 755, 21

Larson, R., 1991 ASPC 20 571L

Letarte, B., Hill, V., Tolstoy, E., Jablonka, P., Shetrone, M., et al., 2010 A&A 523 A17

Liebendörfer, M., Mezzacappa, A., Messer, O. E. B., Martinez-Pinedo, G., Hix, W. R., Thielemann, F.-K., 2003 Nuc Phys A 719 C144-C152

Liebendörfer, M., Messer, O.E.B., Mezzacappa, A., Bruenn, S.W., Cardall, C.Y., Thielemann, F.-K., 2004 ApJ Suppl. Series 150 263-316 DOI: 10.1086/380191

Maíz-Apellániz, J., 2001 ApJL 560, L83

Martinez-Pinedo, G., Fischer, T., Lohs, A., Huther, L., 2012nuco.confE..54M

Matteucci, F., "The chemical evolution of the Galaxy", Astrophysics and space science library, Volume 253, Dordrecht: Kluwer Academic Publishers, ISBN 0-7923-6552-6

Matteucci, F., 2012 Chemical Evolution of Galaxies, Astronomy and Astrophysics Library. ISBN 978-3-642-22490-4. Springer-Verlag Berlin Heidelberg, 2012 DOI: 10.1007/978-3-642-22491-1

Matteucci, F., Romano, D., Arcones, A., Korobkin, O., Rosswog, S., (2014) MNRAS 438 p.2177-2185, DOI:10.1093/mnras/stt2350

McWilliam, A., Wallerstein, G., Mottini, M. 2013 ApJ 778,149

Mendoza-Temis, J., Martinez-Pinedo, G., Langanke, K., Bausweis, A., & Janka, H.-T., (2014) ArXiv

Mennekens, N., Vanbeveren, D., (2014) A&A 564, A134, DOI:10.1051/0004-6361/201322198

Minchev, I., Chiappini, C., Martig, M., 2014 A&A 572 A92-A92

Mösta, P., Richers, S., Ott, C.D., Haas, R., Piro, A.L., Boydstun, K., Abdikamalov, E., Reisswig, C., Schnetter, E., 2014 ApJL 785 L29 DOI: 10.1088/2041-8205/785/2/L29

Nishimura, N., Takiwaki, T., Thielemann, F.-K., arXiv:1501.06567

Nomoto, K., Hashimoto, M., Tsujimoto, T., et al. 1997 Nucl. Phys.A 616 79c13

Nomoto, K., Tominaga, N., Umeda, H., Kobayashi, C., Maeda, K., 2006 Nuc. Phys. A, 777 424-458 DOI: 10.1016/j.nuclphysa.2006.05.008

Nomoto, K., Kobayashi, C., Tominaga, N., 2013 AR A&A 51 457-509, DOI:10.1146/annurev-astro-082812-140956

Padmanabhan, T., "Theoretical Astrophysics, Volume I: Astrophysical Processes", 2000, Cambridge University Press, ISBN: 0-521-56240-6

Padmanabhan, T., ”Theoretical Astrophysics, Volume II: Stars and Stellar Systems”, 2001, Cambridge University Press, ISBN: 0-521-56241-4

Pagel, B., 2009 Nucleosynthesis and Chemical Evolution of Galaxies, Cambridge University Press, ISBN:9780521840309 DOI: 10.1017/CBO9780511812170

Panov, I. V.; Korneev, I. Yu.; Thielemann, F.-K., 2008 AL 34 189-197

Perego, A., Hempel, M., Fröhlich, C., Ebinger, K., Eichler, M., Casanova, J., Liebendörfer, M., Thielemann, F.-K., 2015 arXiv:1501.02845

Postnov, K. A. & Yungelson, L. R. 2014, Living Rev. Rel., 17, 3

Pruet, J., Woosley, S. E., Buras, R., Janka, H.-T., Hoffman, R. D. 2005 ApJ 623 325-336 DOI: 10.1086/428281

Pruet, J., Hoffman, R. D., Woosley, S. E., Janka, H.-T., Buras, R., 2006 ApJ 644 1028-1039. DOI:10.1086/503891

Qian Y.-Z., 2000 ApJL 534 L67

Rauscher, T., Heger, A., Hoffman, R. D., Woosley, S. E., (2002) ApJ 576 (1) 323 DOI:10.1086/341728

Recchi, S., Matteucci, F., D’Ercole, A., 2001 MNRAS 322 800-820, DOI: 10.1046/j.1365-8711.2001.04189.x

Reed, D. S., Balick, B., Hajian, A. R., Klayton, T. L., Giovanardi, S., Casertano, S., Panagia, N., Terzian, Y., 1999 ApJ 118 2430–2441, arXiv:astro-ph/9907313, doi:10.1086/301091

Ren, M. et al., 2012 ApJ 755 89

Roberts, L.F., Kasen, D., Lee, W.H., Ramirez-Ruiz, E., 2011 ApJ 736 L21

Roederer, I.U. et al., 2010 ApJ 724 975

Roederer, I.U. et al., 2014 ApJ 784 158

Roederer, I.U. et al., 2014 AJ, 147 136

Roederer, I.U. et al., 2014 MNRAS 445 2970

Romano, D., Karakas, A. I., Tosi, M., Matteucci, F., 2010 A&A 522 A32, 27, DOI:10.1051/0004-6361/201014483

Stephan Rosswog, 2013 Phil. Trans. R. Soc. A:20120272, DOI: 10.1098/rsta.2012.0272

Rosswog, S., Korobkin, O., Arcones, A., Thielemann, F.-K., Piran, T., 2014 MNRAS 439 744-756 DOI: 10.1093/mnras/stt2502

Ryan, S. G., Norris, J. E., and Beers, T. C., 1996 ApJ, 471 254

Schmidt, M.: 1959 ApJ, 121: 161

Seitenzahl, I. R., Ciaraldi-Schoolmann, F., Röpke, F. K., Fink, M., Hillebrandt, W., Kromer, M., Pakmor, R., Ruiter, A. J., Sim, S. A., Taubenberger, S., 2013 MNRAS 429 1156-1172, DOI:10.1093/mnras/sts402

Shen, S., Cooke, R., Ramirez-Ruiz, E., Madau, P., Mayer, L., Guedes, J., Accepted for ApJ 2015 arXiv:1407.3796

Shetrone, M., Côté, P., Stetson, P. B., 2001 PASP 113 1122

Shetrone, M., Venn, K. A., Tolstoy, E., Primas, F., Hill, V., Kaufer, A., 2003 AJ125 684

Shigeyama, T. and Tsujimoto, T., 1998 ApJ 507 L135

Simmerer, J., et al., 2004 ApJ 617 1091

Simon, J. D., Jacobson, H. R., Frebel, A., Thompson, I. B., Adams, J. J., Shectman, S. A., 2015 ApJ 802, 93

Sneden, C., Cowan, J.J., Gallino, R., 2008 AR A&A 46 241

Spitoni, E., Matteucci, F., Recchi, S., Cescutti, G., Pipino, A., 2009 A&A 504 87-96, DOI: 10.1051/0004-6361/200911768

Starkenburg, E., Hill, V., Tolstoy, E., Franois, P., Irwin, M. J., Boschman, L., Venn, K. A., de Boer, T. J. L., Lemasle, B., Jablonka, P., Battaglia, G., Groot, P., Kaper, L., 2013 A&A 549 88

Suda, T., Katsuta, Y., Yamada, S., Suwa, T., Ishizuka, C., Komiya, Y., Sorai, K., Aikawa, M., Fujimoto, M.Y., 2008 PASJ 60 1159-1171

Suda, T., Yamada, S., Katsuta, Y., Komiya, Y., Ishizuka, C., Aoki, W., Fujimoto, M.Y., 2011 MNRAS 412 843-874

Takahashi, K., Witti, J., Janka, H.T., 1994 A&A 286 857-869

Thielemann, F.-K., Nomoto, K., Hashimoto, M., 1996 ApJ 460 408-436

Thielemann, F.-K., Brachwitz, F., Höflich, P., Martinez-Pinedo, G., Nomoto, K., 2004 New Astronomy Reviews 48 605-610 DOI:10.1016/j.newar.2003.12.038

Thielemann, F.-K., Arcones, A., Käppeli, R., Liebendörfer, M., Rauscher, T., Winteler, C., Fröhlich, C., Dillmann, I., Fischer, T., Martinez-Pinedo, G., Langanke, K., Farouqi, K., Kratz, K.-L., Panov, I., Korneev, I. K., Progress in Particle and Nuclear Physics 66 346-353, DOI: 10.1016/j.ppnp.2011.01.032

Thielemann, F.-K., Eichler, M., Panov, I., Pignatari, M., Wehmeyer, B., "Making the Heaviest Elements also in a Rare Class of Supernovae?", in: Handbook of Supernovae, submitted (2016)

Timmes, F.X., Woosley, S.E., Weaver, T.A., 1995 ApJ Suppl. Series 98 617-658 DOI: 10.1086/192172

Timmes, F. X., Brown, E. F., Truran, J. W., 2003 ApJ 590 L83-L86 DOI:10.1086/376721

Travaglio, C., Galli, D., Gallino, R., Busso, M., Ferrini, F., Staniero, O., 1999 ApJ 521 691-702 DOI: 10.1086/307571

Travaglio, C., Hillebrandt, W., Reinecke, M., Thielemann, F.-K., 2004 A&A 425.1029T

Travaglio, C., Hillebrandt, W., Reinecke, M., 2005 A&A, 443 1007-1011 DOI: 10.1051/0004-6361:20052883

Tsujimoto, T., Shigeyama, T., (2014) A& A 565 id.L5, 4 pp., DOI: 10.1051/0004-6361/201423751

Tsujimoto, T., Ishigaki, M. N., Shigeyama, T., Aoki, W., 2015 PASJ 67, L3

Tsujimoto, T. and Nishimura, N., 2015 ApJL 811, L10

van den Heuvel, E. P. J., Lorimer, D. R., 1996 MNRAS 283 (2) L37-L40

van de Voort, F., Quataert, E., Hopkins, P. F., Keres, D., Faucher-Giguère, C.-A., 2015 MNRAS 447 140-148, DOI:10.1093/mnras/stu2404

Vangioni, E., Goriely, S., Daigne, F., Francois, P., Belczynski, K., ArXiv:1501.01115

Wanajo, S., Sekiguchi, Y., Nishimura, N., Kiuchi, K., Kyutoku, K., Shibata, M., 2014 ApJL 789 L39 DOI: 10.1088/2041-8205/789/2/L39

Wanajo, S., 2006 ApJ 647 1323W, DOI:10.1086/505483

Wanajo, S., 2013 ApJL 770 L22 DOI: 10.1088/2041-8205/770/2/L22

Wehmeyer, B., Pignatari, M., and Thielemann, F.-K., 2015 MNRAS 452, 1970

A. Weigert, H. J. Wendker, L. Wisotzki, ”Astronomie und Astrophysik”, 2006, Wiley VCH, Weinheim, ISBN: 3-527-40358-2

von Weizsäcker, C. F., 1935 Zeitschrift f. Physik 96, 431-458

Woosley, S.E., Wilson, J.R., Mathews, G.J., Hoffman, R.D., Meyer, B.S., 1994 ApJ 433 229-246 DOI:10.1086/174638

Woosley, S. E., Heger, A., Weaver, T. A., 2002 Rev. Mod. Phys., 74 1015-1071 DOI: 10.1103/RevModPhys.74.1015

Winteler, C., Käppeli, R., Perego, A., Arcones, A., Vasset, N., Nishimura, N., Liebendörfer, M., Thielemann, F.-K., 2012 ApJ 750 L22

Wu, M.-R., Qian, Y.-Z., Martinez-Pinedo, G., Fischer, T., Huther, L., 2014 arXiv:1412.8587W

Yamada, S., Suda, T., Komiya, Y., Aoki, W., Fujimoto, M.Y., 2013 MNRAS 436 1362-1380